

University of St Andrews



Full metadata for this thesis is available in
St Andrews Research Repository
at:

<http://research-repository.st-andrews.ac.uk/>

This thesis is protected by original copyright

CERTIFICATE

I certify that James Macdonald Strachan Hutchison, B.Sc., has spent nine terms as a research student in the Physical Laboratory of the United College of the University of St. Andrews, that he has fulfilled the conditions of Ordinance No. 51 of the University Court of St. Andrews and that he is qualified to submit the accompanying Thesis in application for the Degree of Doctor of Philosophy.

Research Supervisor.

DECLARATION

I hereby declare that this Thesis has been composed by me, is a record of work carried out by me and has not previously been presented for a Higher Degree.

CAREER

I matriculated in the United College of St. Salvator and St. Leonard in the University of St. Andrews in October 1958 and followed a course leading to graduation in 1962 with the Degree of Bachelor of Science with First Class Honours in Natural Philosophy. I then spent one year with Marconi's Wireless Telegraph Company. In October 1963, I was admitted by the Senatus Academicus as a research student in the Department of Natural Philosophy of the same College and began the work which is the subject of this Thesis. This research was made possible by an award from the Science Research Council.

ACKNOWLEDGEMENTS

I would particularly like to thank Professor J. F. Allen for the use of facilities in the experimental laboratory, and Dr. D. Bijl for his helpful supervision throughout. I would also like to thank all the technical staff of the Physics Department for their excellent workmanship on the apparatus, the necessary supply of liquid helium and for photocopying facilities; the staff of the Computing Laboratory for the use of the IBM 1620 Computer and helpful advice on computing problems; the research students and members of staff of the Physics Department for interesting and informative discussions; and the Science Research Council for the award of a maintenance grant.

C O N T E N T S

CHAPTER 1 INTRODUCTION

1.1	Definition of Passage	1
1.2	Historical Note	1
1.3	Scope of Thesis	2

CHAPTER 2 GENERAL TREATMENT OF THE BLOCH EQUATIONS

2.1	Introduction	4
2.2	Equations of Motion of a Free Spin	4
2.3	Rotating Coordinate System	5
2.4	The Bloch Equations	6
2.5	The Bloch Equations applied to Fast Passage	8
2.6	Solution of the Bloch Equations	9
2.7	Correlation with Experiment	13

CHAPTER 3 INTERMEDIATE PASSAGE IN INHOMOGENEOUSLY BROADENED LINES

3.1	Introduction	16
3.2	Hole Burning	16
3.3	Intermediate Passage in the Derivative-recording Spectrometer	18
3.4	Behaviour of the Spin System under Field Modulation Alone	18
3.5	Combined Effect of Field Modulation and Field Sweep	21
3.6	Dependence of Signal on Power Level	26
3.7	Saturating Passage	28
3.8	Computer Solutions	30

CHAPTER 4 THE APPARATUS

4.1	Introduction	32
4.2	Microwave Circuitry	33
4.3	Cavity Design	34

4.4	Intermediate Frequency Amplifier	36
4.5	The Local Oscillator and Monitor Klystron A.F.C. Systems	37
4.6	Pulsed Klystron (X.13) A.F.C. System	39
4.7	Magnet and Field Sweep	41
4.8	Field Modulation	42
4.9	Pulse and Gate Circuits	43
4.10	The Apparatus as a Derivative-recording Spectrometer	45
4.11	Display and Recording	46
4.12	Setting-up Procedure	48
4.13	Optimisation	49
4.14	Operation	51
4.15	Limitations of the Apparatus	52
CHAPTER 5	EXPERIMENTS ON NEUTRON-IRRADIATED MAGNESIUM OXIDE	
5.1	Nature of Spectrum	55
5.2	Samples	55
5.3	Measurements of Spin-lattice Relaxation Time	57
5.4	Inversion Measurements - Extended Pulse Technique	60
5.5	Inversion Measurements - Results	62
5.6	Observation of Reverse Relaxation	64
5.7	Locus of the $Z_p = 0$ Contour	65
CHAPTER 6	EXPERIMENTS ON PHOSPHORUS-DOPED SILICON	
6.1	Introduction	66
6.2	Measurements of Spin-lattice Relaxation Time (T_S)	67
6.3	Inversion Measurements	70
6.4	Estimate of T_2	73
6.5	Locus of the $Z_p = 0$ Contour	74
6.6	Optical Stimulation	75
CHAPTER 7	EXPERIMENTS ON NEUTRON-IRRADIATED DIAMOND	
7.1	Introduction	76

7.2	Nature of Spectrum	76
7.3	Relaxation of Holes	77
7.4	Other Characteristics of Holes	79
7.5	Variation of Hole Depth with Sweep Rate and Power	79
7.6	Intermediate Passage Experiments	80
7.7	Even Harmonic type Signals	84
7.8	Measurement of the Overall Spin-lattice Relaxation Time, \bar{T}_1	86
7.9	Confirmation of the $S = 1$ Nature of the Spectrum	87

CHAPTER 8 POINTS ARISING FROM THE WORK AND CONCLUSIONS

8.1	Failure of the Bloch Equations at High Microwave Field	91
8.2	Anomalous Behaviour of the MgO Satellite Line	97
8.3	Locus of the $Z_f = 0$ Contour in MgO	97
8.4	Conclusions and Recommendations	98

APPENDICES

1.	Analytical Solution of the Bloch Equations in Certain Regions	A1
2.	Relation between H_1 and Power for an H_{012} Cavity	A3
3.	Best Fit Exponential for the Case of Non-uniform Time Interval Progression	A5
4.	Curve Fitting - Relaxation Rate against Temperature	A7
5.	Transition Probability in an $S = 1$ System	A8

REFERENCES

(i - iv)

I L L U S T R A T I O N S

Figure	Title	Following Page
2.1	Computer Solution of the Bloch Equations - Program	10
2.2	Typical Passage Signals - Computer Solution	10
2.3	Analogue Computer Circuit	11
2.4	Contour Map of Final Magnetisation, Z_f	11
2.5	The Four Regions of Figure 2.4	11
2.6	Contour Map of Final Magnetisation, Z_f	15
3.1	Hole Burning	17
3.2	Behaviour of a Spin Packet under Field Modulation	17
3.3	Four Examples of Even Harmonic Signals	21
3.4	Variation of T_I and I_1 with λ when $T_o \gg 1$	25
3.5	Variation of Signal Detection Efficiency (Saturating Passage)	29
3.6	Computer Program - Intermediate Passage	30
3.7	Contour Map of I_1 against λ and T_o	30
3.8	Contour Map of I_2 against λ and T_o	30
3.9	Contour Map of T_I against λ and T_o	30
3.10	λ (optimum) against T_o - graph	31
4.1	General View of the Apparatus	32
4.2	Block Diagram of the Spectrometer	32
4.3	The Apparatus as a Derivative-recording Spectrometer (Block Schematic)	32
4.4	The Apparatus as a Relaxation Spectrometer (Block Schematic)	32
4.5	Resonant Cavity Details (Photograph)	35
4.6	Cavity and Variable Coupler (Diagram)	35

Figure	Title	Following Page
4.7	Photograph of Cryostat Assembly between Magnet Poles, showing Field Modulation Coils	35
4.8	I. F. Amplifier	36
4.9	Monitor Klystron and Local Oscillator A.F.C. System	37
4.10	X.13 A.F.C. System	39
4.11	Integrating Amplifier	42
4.12	Slow Sweep Circuit	42
4.13	Field Sweep Amplifier	42
4.14	Pulse Circuits	44
4.15	Gate and Filter	44
4.16	Narrow Band Amplifier	45
4.17	Phase Sensitive Detector	45
4.18	Sampling Circuit	46
4.19	Mode Sweep Circuit	48
4.20	Typical Mode Display	48
4.21	Operating Regions	48
5.1	Temperature Dependence of T_1 in MgO	58
5.2	Diagram Illustrating Extended Pulse Technique	61
5.3	Inversion Map for MgO (2b) Main Line	63
5.4	Inversion Map for MgO (2b) Lowest Satellite	63
5.5	Inversion against Microwave Field	63
5.6	Recordings of Reverse Relaxation	64
6.1	Procedure for Measuring Long Relaxation Times	68
6.2	Typical Traces	68
6.3	Temperature Dependence of T_1 in P-doped Silicon	69

Figure	Title	Following Page
6.4	Inversion Map for P-doped Silicon	71
6.5	System for Recording Multiple Inversion	72
6.6	Typical Recording	72
6.7	Inversion in P-doped Silicon at 5000 gauss / second (actual and theory)	74
7.1	Diamond Spectra (Diagrammatic)	76
7.2	Variation of Hole Relaxation Rate with Position (D 24)	77
7.3	Variation of Hole Depth with Pulse Power	80
7.4	Signals Illustrating "Integration" Phenomenon	81
7.5	Distorted Integration (see text)	83
7.6	Experimental Even Harmonic Signals	84
7.7	Temperature Dependence of \bar{T}_1 in Diamond	86
7.8	Complementary "Hole" and "Hump" Effect	87
8.1	Two Spins in the Rotating Coordinate Frame	91
8.2	Reduction of β for a Gaussian Line Shape	96
A3.1	Computer Program for Appendix 3	A6
A4.1	Computer Program for Appendix 4	A7

T A B L E S

Table	Title	Page
1.	Analogue Computer Settings	11a
2.	Neutron-irradiated MgO Samples	56
3.	Properties of Neutron-irradiated Diamond Samples	78
4.	Experimental Data for the Recordings shown in Figure 7.4	82
5.	Experimental Conditions for the Recordings shown in Figure 7.6	85

CHAPTER 1

INTRODUCTION.

1.1 Definition of Passage.

In Electron Spin Resonance and Nuclear Magnetic Resonance, "Passage" is the name given to any process in which the magnetic field is swept through the resonance line while an R.F. field is being applied to the sample. If this is carried out slowly compared with the spin relaxation times, the system may be regarded as being in equilibrium at all times during passage. However, if such conditions do not hold, as is more generally the case, a dynamic problem results, and the behaviour of the spin system is more complex.

1.2 Historical Note.

Much of the initial work on the dynamic behaviour of spin systems was done using nuclear spins. Since these precess at a much lower rate than electron spins in a given magnetic field, the dynamic effects are more easily observed. The well known Bloch Equations (1946, Ref.1) were intended to be applied to nuclear spin systems. In the first developments in E.S.R. which took place around this time (Refs.2,3), passage effects were of little importance, since electron spin relaxation times are very much shorter in general than their nuclear counterparts, and the steady-state solutions of the Bloch Equations were sufficient. Only with the extension of work to liquid helium temperatures and the development of the two-level maser (Refs.4,5,6) around 1954 did passage effects become important. However, the two-level maser was soon superceded

by the more efficient three-level maser (Ref.7), leaving the understanding of passage effects far from complete. In recent years, the advent of the digital computer has made it possible to attack quantitatively some problems which hitherto had seemed insoluble, and has renewed the interest in the solution of the Bloch Equations. (For example, Ernst and Anderson, 1965, Ref.8)

1.3 Scope of Thesis.

The work contained in this thesis is directed at investigating some of the dynamic effects associated with E.S.R. spectroscopy, especially at low temperatures, where saturation, relaxation and passage effects are important. In the first part of the thesis, two particular aspects of this field are investigated theoretically.

1.) In Chapter 2, the process generally referred to as Adiabatic Fast Passage is investigated quantitatively. This is a standard technique for inverting spin populations, as in a two-level maser, for example, but the efficiency of inversion is never as high as might be hoped (i.e. 100%). The treatment is restricted to a single E.S.R. line, or a single spin packet within a line.

2.) In Chapter 3, the treatment is extended to a distribution of spin packets, known generally as an inhomogeneously broadened line. The theory is developed with particular reference to the operation of a normal derivative-recording type of spectrometer.

Chapter 4 deals with the design and construction of the apparatus for observing and measuring passage effects. It was initially designed as a pulsed relaxation spectrometer, but it was found advantageous to

instal facilities for using it as a derivative-recording spectrometer. Versatility rather than sensitivity was aimed at in the design.

From the selection available, the materials chosen for study were neutron-irradiated magnesium oxide, phosphorus-doped silicon and neutron-irradiated diamond. These were chosen not so much from the point of view of studying the materials themselves as for the variety of spin systems and spectra they provide. The magnesium oxide line is narrow with no observable inhomogeneous broadening; the diamond line is a prime example of an inhomogeneously broadened line; the silicon line has an extremely long spin-lattice relaxation time. The experiments on these materials are described in Chapters 5, 6 and 7.

Chapter 8 discusses some points arising from the preceding work and conclusions.

Experimentally, the work has been biased towards developing new techniques of investigating spin systems, rather than carrying out investigations using well established techniques.

CHAPTER 2

GENERAL TREATMENT OF THE BLOCH EQUATIONS.2.1 Introduction.

The purpose of this chapter is to attempt to derive a quantitative account of the behaviour of a spin system under the conditions of varying magnetic field encountered in the process known as Fast Passage. A special form of this process, known as Adiabatic Fast Passage has been used by many workers, both in E.S.R. and N.M.R. to invert the spin populations of ~~para~~^{para}magnetic substances, and the essentials of the process are adequately described in the literature (Refs. 8 to 13, for example). It need only be said at this stage that a high power microwave field is applied to the sample, while the magnetic field is swept through the resonance line fairly rapidly (as for example in Section 5.5). As is always the case in practice, the process is never 100% efficient, and the purpose of our investigation is to find out why this is so, and to try to derive a quantitative estimate of how efficient the process should be under a given set of conditions.

2.2 Equations of Motion of a Free Spin.

Both the Classical and Quantum Mechanical derivations of the equations of motion of a free spin in a magnetic field are adequately described in the literature (for example, Slichter, Ref. 13). In both cases they can be expressed by the vector equation

$$d\mu/dt = \mu \times \gamma \underline{H} \quad (2.1)$$

where $\underline{\mu}$ is the vector magnetic moment of the spin (the expectation value in the quantum case), γ the ~~gyromagnetic~~ ^{magnetogyric} ratio and \underline{H} the vector magnetic field. This equation can be extended to an aggregate of spins in a bulk sample, provided that the spins are independent and all have the same γ . Then the bulk magnetisation of the sample is

$$\underline{M} = \sum \underline{\mu}$$

and
$$d\underline{M}/dt = \underline{M} \times \gamma \underline{H} \quad (2.2)$$

2.3 Rotating Coordinate System.

In order to deal with a spin system under the influence of a magnetic microwave field, it is convenient to transform to a rectangular coordinate system which is rotating about the main magnetic field direction (usually taken as the Z-axis) at the microwave frequency ω , the sense of rotation being that in which the spins would normally precess. It is found that the motion of the spins is now represented by the same set of equations, 2.2, except that $H_z = H - \omega/\gamma$, where H is the main magnetic field. When tuned exactly to the resonance line, $\omega = \omega_0 = \gamma H_0$ and $H_z = 0$. The microwave field is usually taken as being in the X-direction, and for convenience is written

$$H_x = 2H_1 \cos \omega t \quad (2.3)$$

In the rotating coordinate system, this can be resolved into two components, one of magnitude H_1 in the X-direction, and the other of magnitude H_1 rotating about the Z-axis at a frequency 2ω . The latter component is generally insignificant, as it is too rapidly varying

to affect the spins, although if H_1 is large, it can introduce a shift in the resonance field of the order of $H_1 / 4H_0$, the so-called Bloch Shift (Refs. 14,15) as well as producing higher order resonances (Refs. 16,17). For the magnitudes of H_1 normally used, these effects may be neglected. The fields are therefore

$$\begin{aligned} H_x &= H_1 \\ H_y &= 0 \\ H_z &= H - H_0 \end{aligned} \quad (2.4)$$

where H_0 is the resonance field corresponding to the microwave frequency ω , i.e. $H_0 = \omega / \gamma$.

2.4 The Bloch Equations.

To take account of spin-spin and spin-lattice interaction, Bloch (Ref. 1) introduced two relaxation times T_1 and T_2 into his formulation. T_1 , the spin-lattice relaxation time is the time taken for the spin system to return to thermal equilibrium with the environment after the populations of the two levels have been altered from their equilibrium values, i.e. the time for M_z to return to equilibrium M_0 . T_2 , the spin-spin relaxation time, is the time taken for the transverse components of magnetisation in the rotating coordinate system, i.e. M_x and M_y to decay. Hence equations 2.2 become the familiar Bloch Equations

$$\begin{aligned} \frac{dM_x}{dt} &= \gamma H_z M_y - M_x / T_2 \\ \frac{dM_y}{dt} &= \gamma (H_x M_z - H_z M_x) - M_y / T_2 \end{aligned}$$

$$dM_z / dt = -\gamma H M_y - (M_z - M_0) / T_1 \quad (2.5)$$

Returning to the laboratory coordinate frame, M_x and M_y appear as R.F. magnetisations of amplitude M_x in phase with the microwave field, and of amplitude M_y lagging by 90 degrees respectively. They may be related to the apparent components of R.F. susceptibility of the sample

$$\chi' = M_x / 2H_1 \quad ; \quad \chi'' = M_y / 2H_1$$

The steady-state solution of the Bloch Equations (Refs. 14,18) is normally expressed in terms of these components of susceptibility

$$\chi' = \frac{1}{2} \chi_0 \omega_0 T_2 \frac{\Delta \omega T_2}{1 + (\Delta \omega T_2)^2 + \gamma^2 H_1^2 T_1 T_2}$$

$$\chi'' = \frac{1}{2} \chi_0 \omega_0 T_2 \frac{1}{1 + (\Delta \omega T_2)^2 + \gamma^2 H_1^2 T_1 T_2} \quad (2.6)$$

where $\Delta \omega = \omega - \omega_0$, the difference between the resonance frequency ω_0 and the microwave frequency ω

and $\chi_0 =$ the d.c. susceptibility, M_0 / H_0

χ'' gives rise to the absorption signal normally observed in an E.S.R. spectrometer. Plotted against ω , it has a Lorentzian shape of width $2/T_2$ at the half-signal points, provided $\gamma^2 H_1^2 T_1 T_2 \ll 1$ (i.e. non-saturating conditions). It is commoner, however, to observe the signal as a function of magnetic field at a constant frequency, and in this case the line width is $2 / \gamma T_2$.

This relation between line width and T_2 is only valid for a homogeneous line; that is, one in which γ is the same for every spin, and all spins "see" the same magnetic field. If the system is such that the spins exhibit a spread of resonant frequencies for a given external magnetic field, due to local fields within the sample, or a spread of γ , then the spectrum is known as "inhomogeneously broadened". If the above equations are to be at all valid in such a system, they may only be applied to such a fraction of the total spins as have the same resonant frequency in a given field. Such a fraction is known as a "spin packet" (Ref.19), and has a basic line width of $2/\gamma T_2$. The whole line, consisting of a number of such packets, has a line width of the order of $1/\gamma T_2^*$, where T_2^* is the characteristic de-phasing time of the spins as a whole, i.e. the decay time of the total transverse magnetisation. The exact relation between T_2^* and line width depends on the overall line shape.

The concept of a spin system composed of a number of non-interacting spin packets is very useful, and will be used throughout the following treatment, but it also has its limitations, which will be discussed further in Chapter 8. The distinction between spin-spin interaction and cross relaxation (Ref.20) becomes somewhat vague when applied to inhomogeneously broadened lines.

2.5 The Bloch Equations applied to Fast Passage.

Suppose that during fast passage the external field is varying at a uniform rate $R = dH/dt$. Referring to the rotating coordinate system,

$$H_z = Rt$$

if we time the sweep to pass through resonance at $t = 0$.

It is convenient to normalise a number of quantities in such a way that the microwave field is one unit, the thermal equilibrium value of the magnetisation is one unit, and the angular velocity of precession in unit field is unity. This can be done by taking a time scale

$$t' = \gamma H_1 t$$

and letting $X = M_x / M_0$ and so on.

Hence $H_z = rt'$ where $r = R / \gamma H_1^2$

The normalised relaxation rates are

$$\alpha = 1 / \gamma H_1 T_1 \quad \text{and} \quad \beta = 1 / \gamma H_1 T_2$$

and the normalised Bloch Equations

$$\begin{aligned} dX / dt' &= rt'Y - \beta X \\ dY / dt' &= -rt'X - \beta Y + Z \\ dZ / dt' &= -Y + \alpha(1 - Z) \end{aligned} \quad (2.7)$$

In most of the experimental cases under consideration, passage through the line takes place in a time very short compared with T_1 , so that $\alpha \ll 1$ and the term in α may be neglected, or that to a first approximation, the spin-lattice relaxation starts at $t' = 0$ and proceeds independently. This makes computation easier, and leads to a final stable value of Z at the end of passage, Z_f . Then, as far as future spin-lattice relaxation is concerned, this value Z_f can be assumed to occur at $t' = 0$, thereafter relaxing to $Z = 1$ with time constant T_1 , or α^{-1} in the normalised time scale.

2.6 Solution of the Bloch Equations.

Setting $\alpha = 0$, analytical solutions can be found for equations 2.7

for certain ranges of the parameters β and r . The boundary conditions imposed are that $Z = 1$, $X = 0$ and $Y = 0$ at $t' = -\infty$, corresponding to the thermal equilibrium state before passage.

(a) When $\beta \gg 1$,

$$Z_f = e^{-\pi/r}$$

(b) When $r \ll 1$,

$$Z_f = e^{-\pi r/\beta} \quad (2.8)$$

The derivation of these solutions is given in Appendix 1.

Several workers have obtained numerical solutions to the Bloch Equations under various conditions. Hyde (Refs. 21,22) has solved them with a view to the ultimate sensitivity of a spectrometer under saturating conditions. Firth (Ref. 11) investigated them from the standpoint of maser oscillation, which involves the reaction of the magnetisation on the cavity microwave field. However, a comprehensive set of solutions, with a bearing on the question of inversion efficiency, was not available at the time.

In view of the recent acquisition by St. Andrews University of an IBM 1620 digital computer, it was decided to construct a FORTRAN program to solve equations 2.7 for a range of values of β and r . A fourth order Runge-Kutta method was chosen (Ref. 23), the range of t' being limited to $-5 \leq t' \leq +5$ to save computer time. This limited range is a compromise between the ideal but impractical infinite range and one which is too short to give a realistic solution. The program is shown in Figure 2.1. In view of the necessarily reduced range of t' , the program was started with the magnetisation parallel to the instantaneous magnetic field in

SATURATION EFFECTS 6. J. HUTCHISON.

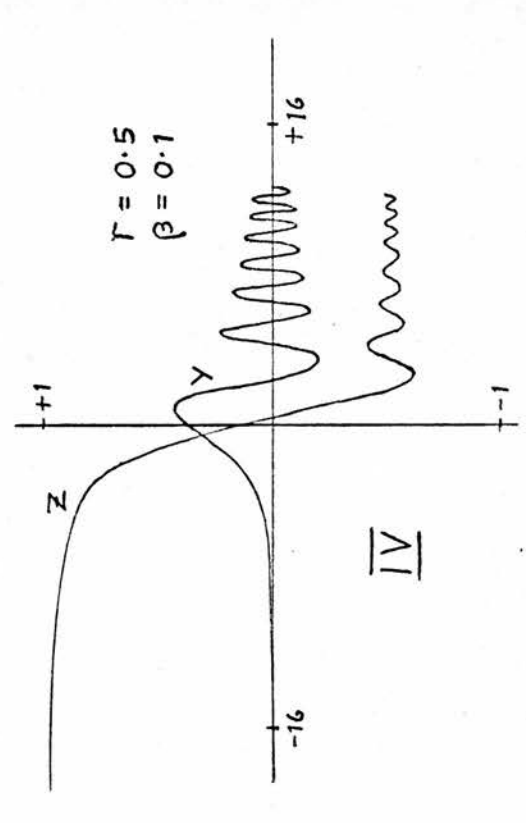
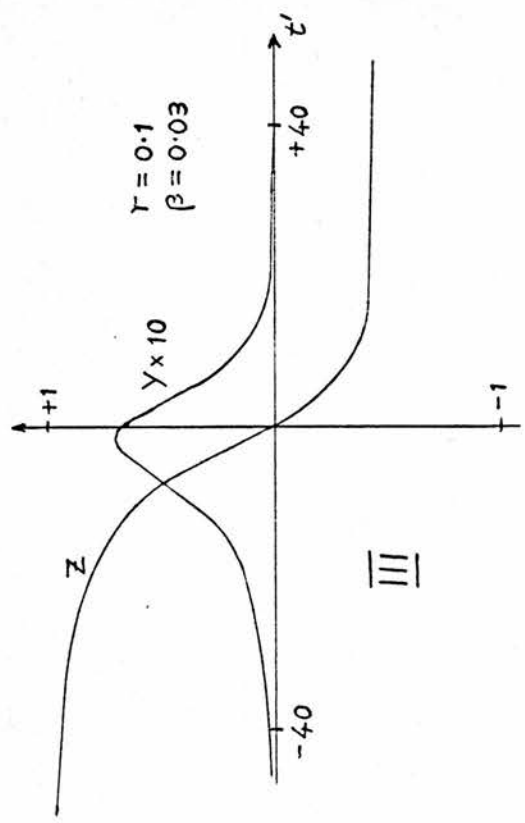
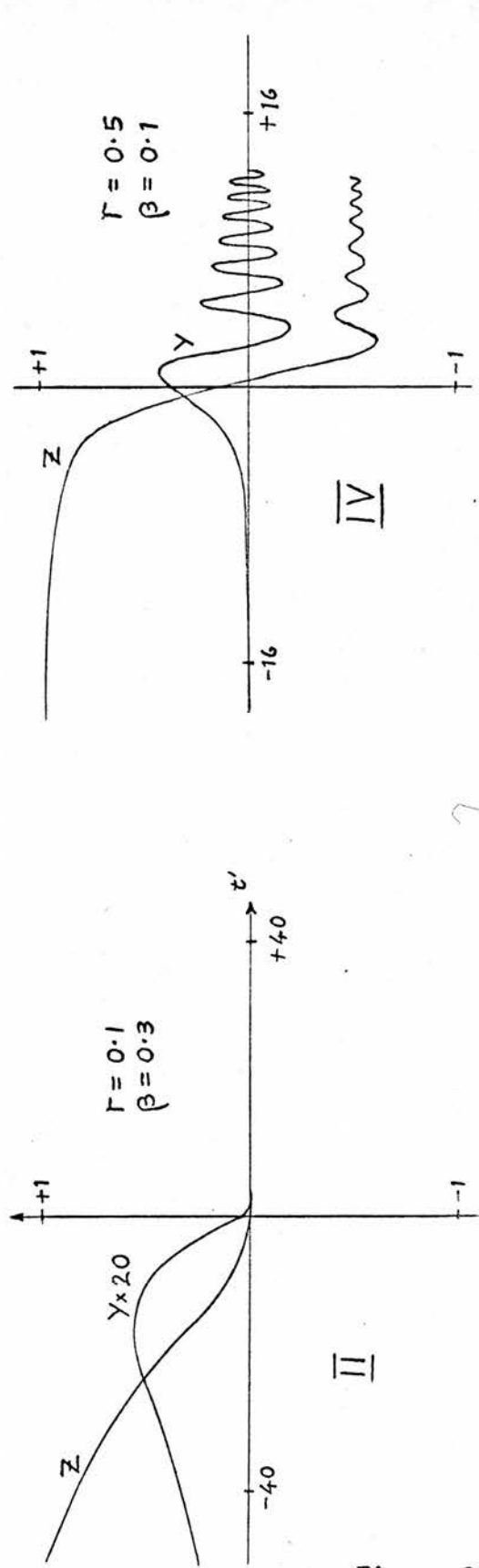
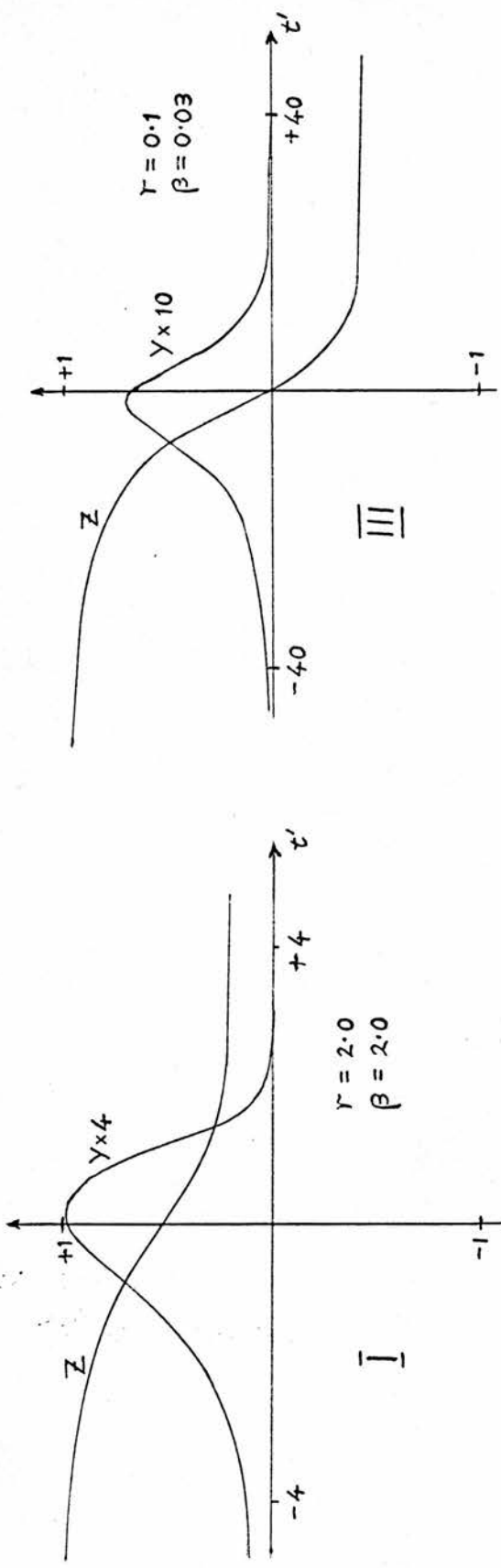
```

C   INTERMEDIATE PASSAGE
C   FOURTH ORDER RUNGE-KUTTA METHOD.
F1(T,X,Y,Z)=-B*X-R*T*Y
F2(T,X,Y,Z)=R*T*X-B*Y-Z
F3(T,X,Y,Z)=Y+A*(1.-Z)
DIMENSION UU(10),VV(10),WW(10),Q(12)
PRINT 20
8 READ 7,A,B,R,H,N
PRINT 21,A,B,R,H
S=N
S=S*H
T=-S
U=-1./(S*R)
V=0.
W=1.
HH=H*.5
9 DO 6 I=1,10
  Q(1)=HH*F1(T,U,V,W)
  Q(2)=HH*F2(T,U,V,W)
  Q(3)=HH*F3(T,U,V,W)
  Q(4)=HH*F1(T+HH,U+Q(1),V+Q(2),W+Q(3))
  Q(5)=HH*F2(T+HH,U+Q(1),V+Q(2),W+Q(3))
  Q(6)=HH*F3(T+HH,U+Q(1),V+Q(2),W+Q(3))
  Q(7)= H*F1(T+HH,U+Q(4),V+Q(5),W+Q(6))
  Q(8)= H*F2(T+HH,U+Q(4),V+Q(5),W+Q(6))
  Q(9)= H*F3(T+HH,U+Q(4),V+Q(5),W+Q(6))
  Q(10)=H*F1(T+H,U+Q(7),V+Q(8),W+Q(9))
  Q(11)=H*F2(T+H,U+Q(7),V+Q(8),W+Q(9))
  Q(12)=H*F3(T+H,U+Q(7),V+Q(8),W+Q(9))
  U=U+(2.*(Q(1)+Q(7))+4.*Q(4)+Q(10))/6.
  V=V+(2.*(Q(2)+Q(8))+4.*Q(5)+Q(11))/6.
  W=W+(2.*(Q(3)+Q(9))+4.*Q(6)+Q(12))/6.
  UU(I)=U
  VV(I)=V
  WW(I)=W
6 T=T+H
PRINT 22,UU,VV,WW
IF(T-S)9,8,8
7 FORMAT(3E10.3,F5.3,I5)
20 FORMAT(24H SATURATION EFFECTS 6. /
1 30H SOLUTION OF BLOCH EQUATIONS. )
21 FORMAT(8H ALPHA= E10.3,7H BETA= E10.3,4H R= E10.3,
1 40H PROGRESS OF X, Y, Z IN STEPS OF
2 F5.3//)
22 FORMAT(3(10F10.5//))
19 CALL EXIT
END

```

Computer Solution of the Bloch Equations.

Figure 2.1



TYPICAL PASSAGE SIGNALS (COMPUTER SOLUTIONS)

Figure 2.2

the rotating coordinate system, and not parallel to the Z-axis; this overcame some undesirable oscillations which occurred immediately after the start. The results are presented in terms of

the dispersion signal X

the absorption signal Y

the polarisation Z

Some examples of the variation of these quantities with time for different sets of parameters r and β are shown in Figure 2.2.

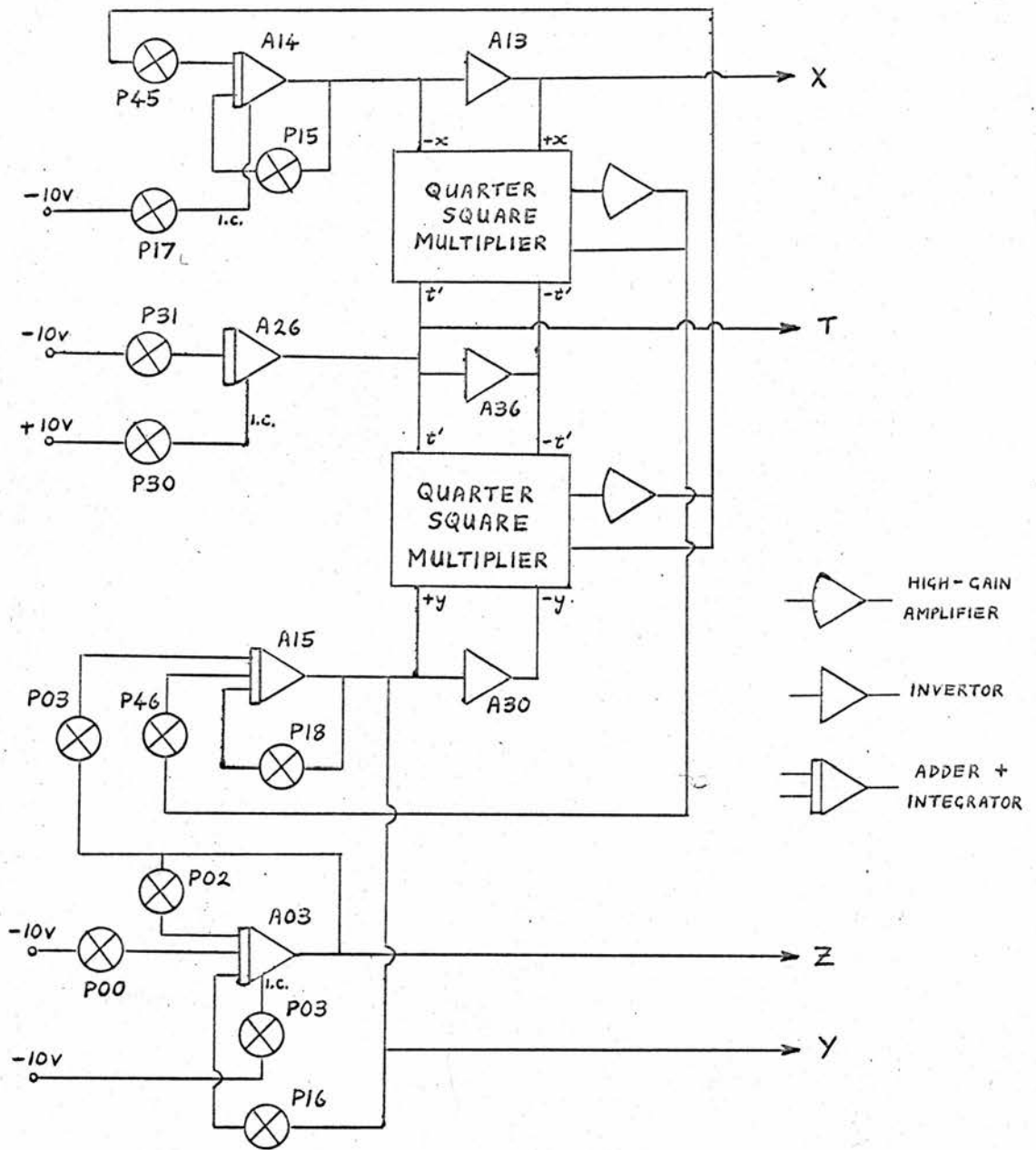
The problem was also set up on an analogue computer (a PACE TR48) for comparison with the digital solution. Its performance was found to be superior in those cases where oscillations ("wiggles") occur, since the variation of \mathbf{E}' is continuous. The circuit for this is shown in Figure 2.3 and the potentiometer settings in Table 1. Four different groups of settings were used to obtain efficient operation over a range of β and r . In groups 2 and 3 the equations were modified to

$$\begin{aligned} dX / dt'' &= -(\beta/r)X + (t''/r)Y \\ dY / dt'' &= -(\beta/r)Y + (1/r)Z - (t''/r)X \\ dZ / dt'' &= (\alpha/r)(1 - Z) - (1/r)Y \end{aligned} \quad (2.9)$$

where $t'' = rt'$.

In group 4, the constant k (see Table 1) was chosen to modify the range of t' . $k = 2$ was used for $r \geq 1$ and $k = 2/r$ for $r < 1$.

The combined results of these two programs, together with the analytical solutions (2.8), were used to construct the contour map shown in Figure 2.4. This is a map of Z_p plotted against r and β , with logarithmic axes. It can conveniently be divided into four regions, as illustrated in Figure 2.5.



ANALOGUE COMPUTER CIRCUIT

Figure 2.3

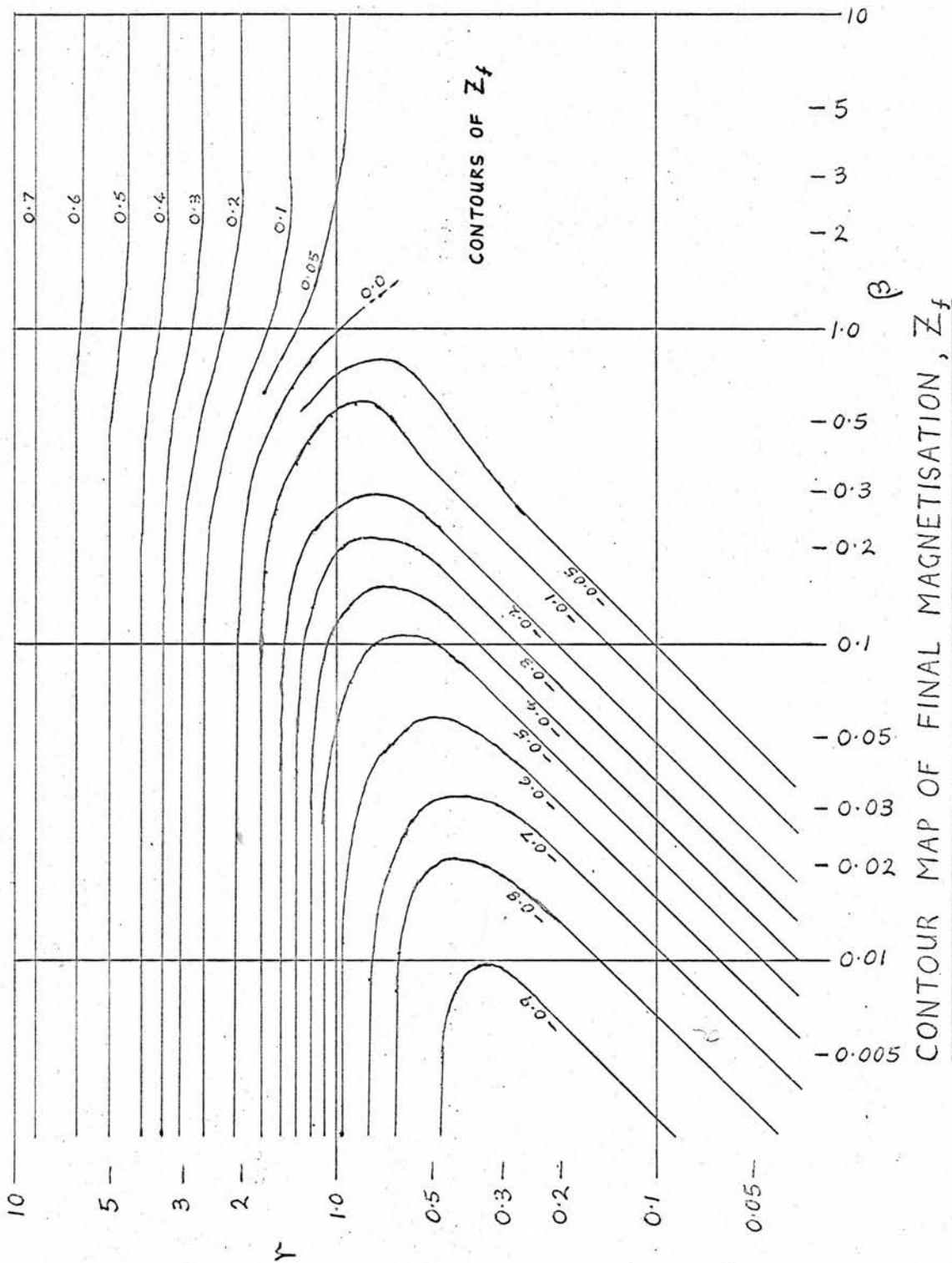
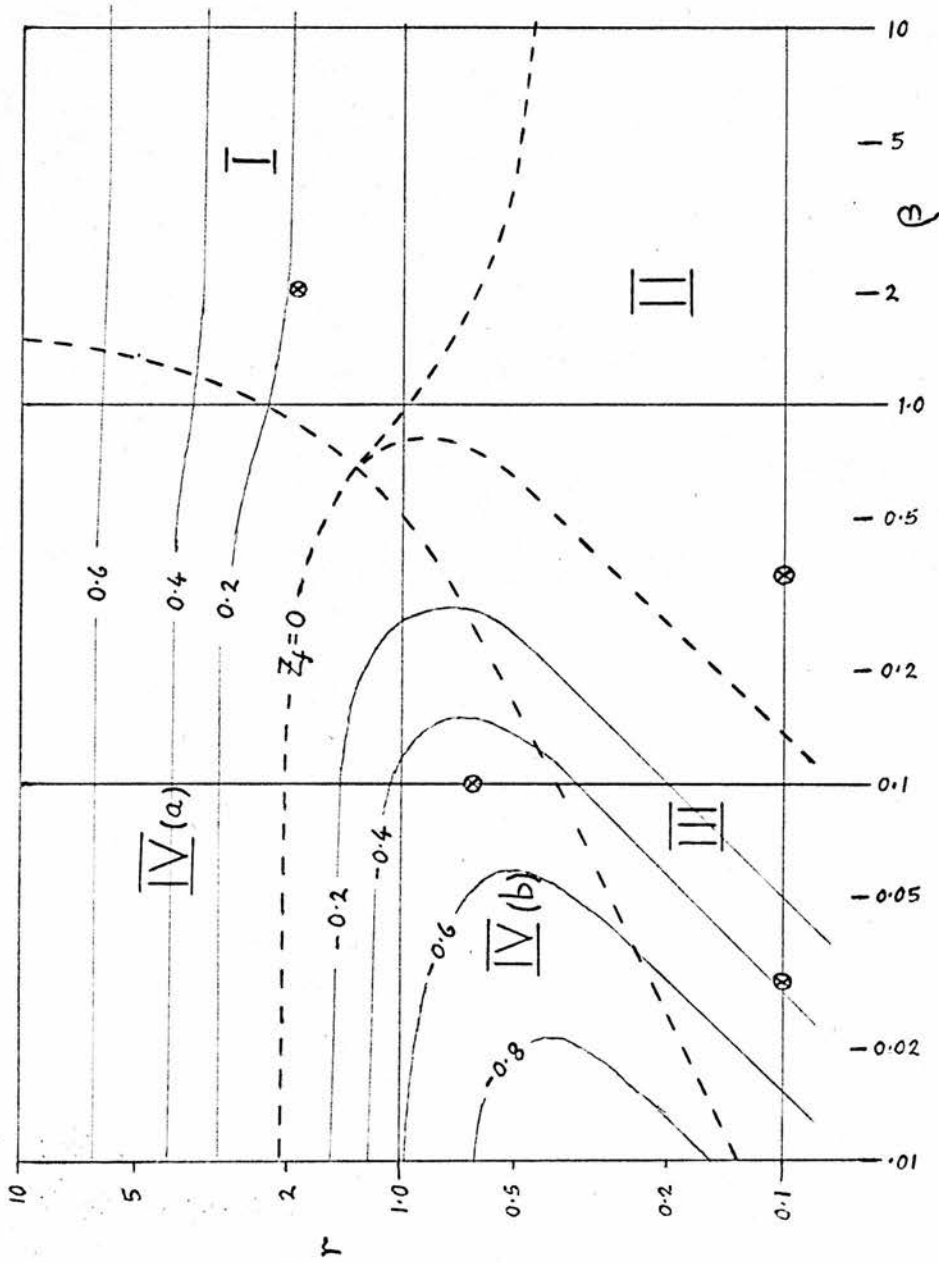


Figure 2.4



THE FOUR REGIONS OF FIGURE 2.4

- \otimes POINTS TAKEN FOR FIGURE 2.2
- - - - - APPROXIMATE REGION BOUNDARIES

Figure 2.5

TABLE 1.

Element of Computer	Setting			
	Group 1.	Group 2.	Group 3.	Group 4.
A 03 } A14 } A 15 }	1.0	1.0	0.1	0.1
{ P 00 P 02 }	∞	∞ / r	∞ / r	$\infty / 10$
P 03	1.0	1.0	1.0	1.0
P 15	β	β / r	β / r	$\beta / 10$
P 16	1.0	1 / r	1 / r	0.1
P 17	(0.1)*	*	*	*
P 18	β	β / r	β / r	$\beta / 10$
P 30	1.0	1.0	1.0	1.0
P 31	r / 10	1 / 10r	1 / r	1 / 10k
P 45	10	10	10	kr
P 46	10	10	10	kr
Range of t'	$\pm 10 / r$	± 10	± 10	$\pm 10k$

* P 17 is adjusted to minimise initial oscillations. It represents an initial value of X in the equations. The constant k merely alters the range of T'.

I. The Partial Saturation region. This is the region in which most conventional spectroscopy is done. No inversion of the magnetisation takes place, as this region corresponds to a relatively small microwave field (i.e. low power).

II. The Complete Saturation region. $Z_f \doteq 0$

III. The Adiabatic Inversion region, which represents the conditions normally used in Adiabatic Fast Passage (A.F.P.). Inversion proceeds smoothly in this region, although it is not the region of greatest inversion efficiency. Again, an analytical solution exists over most of this region.

IV. The "Wiggles" region. The variation of Z with t' over this region shows characteristic oscillations or "wiggles". These are not normally observed in E.S.R. as they are too fast, but are common in N.M.R., where T_2 can be quite large. In the sub-region (a), Z_f is positive while in (b) it is negative, but this is the only significant difference between the two sub-regions.

Typical signals (absorption) and variation of Z (polarisation) for these four regions are shown in Figure 2.2 (I,II,III and IV respectively).

The criteria normally assumed for A.F.P., i.e. that passage should be fast compared to the spin relaxation times, but sufficiently slow for the magnetisation to follow the magnetic field direction in the rotating coordinate frame (adiabaticity), can be expressed by the inequality

$$1 \gg r \gg \alpha, \beta$$

Some workers even consider that β is unimportant. Redfield's criteria (Ref. 24) can be expressed as

$$l \gg r \gg \alpha$$

and

$$l \gg \beta$$

His arguments that the Bloch Equations fail at high microwave fields ($\beta \ll 1$) are plausible to a certain extent, but they are erroneous in that he assumes that the T_2 decay is an iso-entropic process. This matter will be more fully discussed in Chapter 8.

2.7 Correlation with Experiment.

The quantities r , β and Z_p , although not directly observable with the apparatus, may be related to directly observable quantities such as field sweep rate, incident microwave power and absorption signal. The rotating component of microwave field in the cavity, H_1 , is related to the incident microwave power P by

$$P = \frac{H_1^2 V \omega}{4 \mu_0 Q_L} (L^2/B^2 + 1)$$

where

P = incident microwave power (watts)

H_1 = field component (weber metre⁻²)

ω = microwave angular frequency (sec.⁻¹)

μ_0 = permeability of free space ($4\pi \times 10^{-7}$ henry metre⁻¹)

Q_L = loaded cavity Q (near critical coupling is assumed)

V = cavity volume (metre³)

$2L$ = length of cavity (metre)

B = width of cavity (metre)

The derivation of this formula is given in Appendix 2, along with a numerical calculation for the cavity in question. For a given cavity, then,

$$P \propto H_1^2$$

Hence $r = (1/\gamma H_1^2)(dH/dt) \propto (dH/dt)/P$

and $\beta = 1/\gamma H_1 T_2 \propto P^{-1/2}$

In this way Z_f can now be plotted as a function of normalised incident power P' and normalised sweep rate S , such that

$$P' = \beta^{-2} \quad ; \quad S = r\beta^{-2}$$

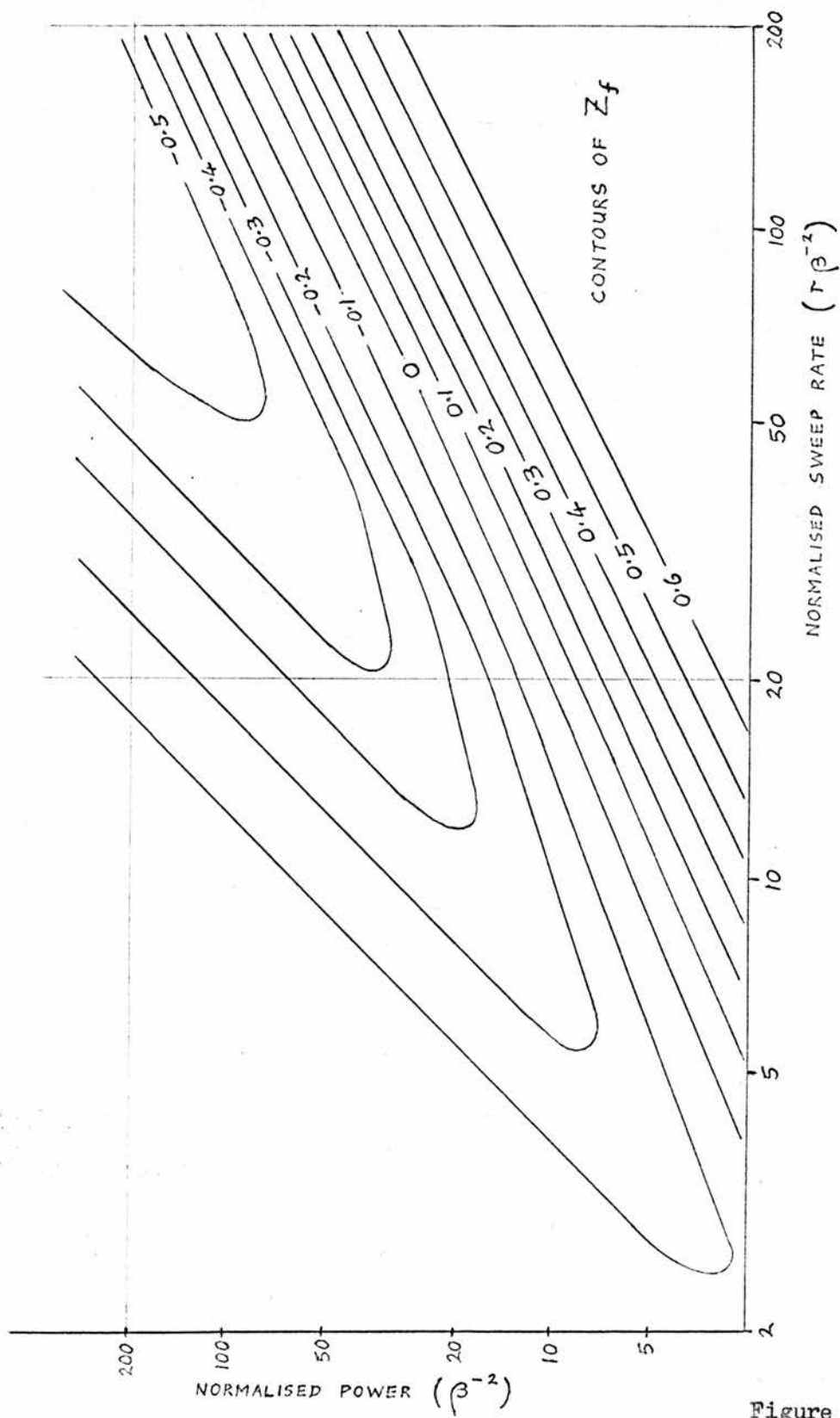
This has been done in Figure 2.6, again with logarithmic axes. When an experimental plot of Z_f against power and sweep rate is obtained, it can be matched to Figure 2.6, the relation between P and P' decided, and hence a value of T_2 obtained. Z_f is obtained by observing the absorption signal with a very low monitor microwave power. The techniques involved are discussed fully in Chapter 5.

The ability to calculate r before the experiment provides an absolute test of certain aspects of the Bloch Equations. For if it is known that either $\beta \ll 1$ or $\beta \gg 1$, then Z_f is a function of r alone and should be predictable. In particular, the case of $Z_f = 0$ is easily found experimentally, and for small β , corresponds to $r = 2.26$. This leads to a constant value for the ratio of sweep rate to incident power

$$R^* = (dH/dt)/P = 40 \text{ gauss per microwatt second}$$

for the cavity in question. It can also be shown that this condition ($\beta \ll 1$, $r = 2.26$) is exactly equivalent to a so-called "90-degree pulse". This is obtained by using a pulse half the length of the "180-degree pulse", a technique widely used in N.M.R. for inverting resonance lines.

During a "90 degree pulse", the initial Z- magnetisation is rotated so that it lies entirely in the X-Y plane.



CONTOUR MAP OF FINAL MAGNETISATION, Z_f

Figure 2.6

CHAPTER 3

INTERMEDIATE PASSAGE IN INHOMOGENEOUSLY BROADENED LINES.3.1 Introduction.

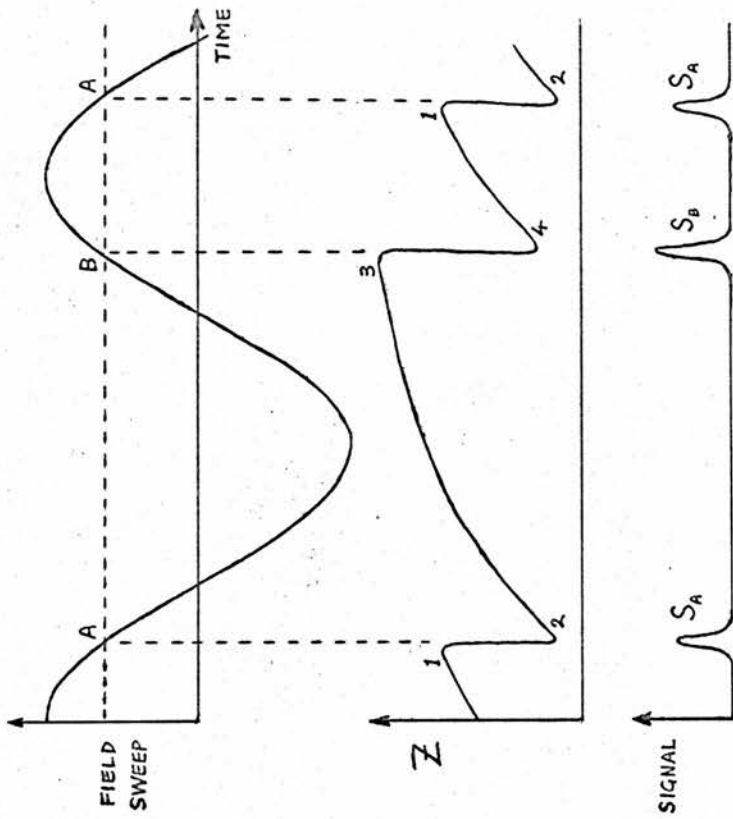
As mentioned in Chapter 2, an E.S.R. line may be composed of a large number of so-called "spin packets" each of fairly narrow line width, but spread over a relatively large range of field. This system is known as an inhomogeneously broadened line (see, for example, Refs. 19, 21, 22, 25, 26) and can be identified, at least at low temperatures, by the ability to have "holes" burnt in it by a microwave signal. Such a line is of particular interest at liquid helium temperatures, since it is only at such temperatures that it becomes readily distinguishable from a homogeneously broadened line. The purpose of this chapter is to investigate the behaviour of inhomogeneously broadened lines under various conditions encountered in the spectrometer.

Firstly, the behaviour of the spin system under field modulation alone will be considered; this is an equilibrium situation, where the pattern of behaviour is repeated every cycle of the modulation. Then, from section 3.5 onwards, the more general case including linear field sweep will be dealt with. The theory discussed in Chapter 2 will be used as a basis for the work in this chapter; in particular, the solutions for Regions I and II, corresponding to moderately low power levels, will be used.

3.2 Hole Burning.

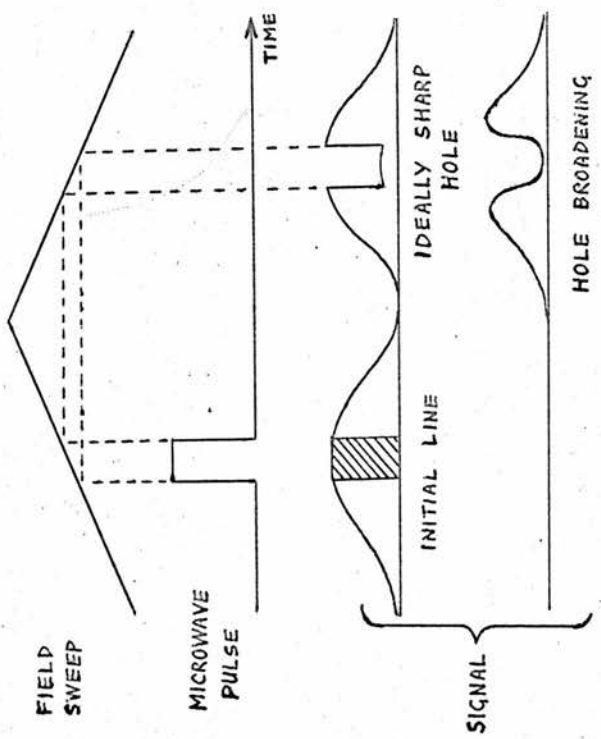
The phenomenon of hole-burning has been observed by a number of

workers (for example Refs. 20, 27, 28), and occurs when part of an inhomogeneously broadened line is selectively irradiated with microwave power. Generally the magnetic field is swept through the line, and a microwave pulse applied to the sample during the time in which the field is sweeping over that part of the line in which it is desired to burn a hole. Consequently, only those spin packets which fall within the desired range are affected, and can be treated individually as if passage had occurred, provided that the total sweep range is significantly wider than the spin packet. Near the ends of the sweep range, however, passage will be incomplete, resulting in less saturation of the spins in these regions. This gives rise to a "rounding off" of the edges of the hole, as illustrated in Figure 3.1. Part of this "rounding off" is fundamental, since the edges of a hole cannot be sharper than the spin packets constituting it, and part due to incomplete passage. When the microwave field component H_1 is large compared with the basic line width, the latter predominates, the range over which passage is incomplete being of the order of $\pm H_1$; this results in a "rounding off" of this order of magnitude. The extent to which the edges of the hole are rounded off can therefore indicate the order of magnitude of the basic line width of the spin packets, and hence of T_2 (as in section 6.5, for example). The only other method of finding T_2 is by the "spin echo" technique used in N.M.R. (Ref. 29). This technique is not very useful in E.S.R. since it involves the use of pulses which are an order of magnitude shorter than T_2 . Since T_2 is of the order of a microsecond or less, very short and powerful pulses are required. It is also required



BEHAVIOUR OF A SPIN PACKET
UNDER FIELD MODULATION

Figure 3.2



HOLE BURNING

Figure 3.1

that the I.F. amplifier have a very fast recovery time after the power pulse.

3.3 Intermediate Passage in the Derivative-recording Spectrometer.

Most derivative-recording spectrometers are required to work at a sufficiently low power level to avoid saturation of the E.S.R. spectrum, and at a sufficiently slow sweep rate to ensure that the system is effectively in equilibrium at all times. When the power level is not low enough to avoid saturation, and the sweep speed is too fast to allow an equilibrium to be reached, certain effects occur which will be referred to henceforth as "Intermediate Passage" effects. The most striking of these is that the signal is partially integrated; that is, in addition to the usual derivative line shape, a component of the original, undifferentiated line shape is present, the sign being determined by the direction of sweep.

3.4 Behaviour of the Spin System under Field Modulation alone.

Consider first the case of no field sweep, but merely field modulation, and assume that the basic line width is very much less than the modulation depth. One other assumption will be made, namely that the time taken for the field to pass through a spin packet (i.e. cover the basic line width) is very much less than T_1 . This is in complete contrast to the requirements of the steady-state solutions (2.6), i.e. T_1 much less than the time of passage, and means that the absorption signal obtained from a given spin packet depends only on the amount by which its polarisation (Z) is changed during passage, and not on the

actual polarisation, as in the steady-state case. This follows from the third of equations 2.7, for if it is assumed that α is small, the total signal from the spin packet is proportional to

$$\int Y \cdot dt = -\Delta Z (dt/dt')$$

Since dt/dt' depends only on H_1 , which is constant, the signal is proportional to ΔZ . Suppose the field modulation is

$$H = H_0 + A \cos \omega_m t$$

$$\text{then } r = (dH/dt)/\gamma H_1^2 = -r_0 \sin \omega_m t \quad \text{where } r_0 = \omega_m A / \gamma H_1^2$$

Any given spin packet will be passed through twice in each cycle at times t and $2\pi/\omega_m - t$. Each time the polarisation Z will be changed by an amount depending on 1.) the initial value Z_i and 2.) the sweep rate r . The ratio Z_f/Z_i is a function of r , treated in Chapter 2, and may be written $f(r)$. Between passages, the polarisation relaxes towards $Z = 1$ with characteristic time T_1 . The behaviour of Z is shown diagrammatically in Figure 3.2.

Four significant points on the curve of Z against t are labelled in Figure 3.2; at the points A and B passage occurs, and each time the polarisation is reduced by a factor $f(r)$. Hence

$$Z_2 / Z_1 = f(r_0 \sin \omega_m t)$$

$$Z_4 / Z_3 = f(r_0 \sin \omega_m t)$$

and the relaxation between passages,

$$(1 - Z_2)/(1 - Z_3) = \exp \left[(2\pi/\omega_m - 2t) / T_1 \right]$$

$$(1 - Z_4)/(1 - Z_1) = \exp [2t / T_1] \quad (3.1)$$

The solution of this set of equations yields

$$\text{Signal at A, } S_a = Z_1 - Z_2 = (1-f) [f + (1-f)E_1 - E] / (f^2 - E)$$

$$\text{Signal at B, } S_b = Z_3 - Z_4 = (1-f) [f + (1-f)E_2 - E] / (f^2 - E)$$

$$\text{where } E_1 = \exp [(2\pi/\omega_m - 2t)/T_1] \quad ; \quad E_2 = \exp [2t/T_1] \quad ;$$

$$E = \exp [2\pi/\omega_m T_1] \quad (3.2)$$

In the particular example shown in Figure 3.2, where $AB > BA$, this does in fact lead to $S_a < S_b$.

The relation between f and t may be known in certain cases. For instance, if $\beta \gg 1$, as will be the case in low power operation,

$$\begin{aligned} f(r) &= \exp(-\pi/r) \quad \text{from Appendix 1.} \\ &= \exp[-\pi/(r_0 |\sin \omega_m t|)] \end{aligned}$$

Thus, in principle, S_a can be expressed as a function of t (S_b is the same function of $2\pi/\omega_m - t$). There are a few limiting cases where a simple solution is obtained:

1) $\omega_m T_1 \ll 1$. The spin packet recovers fully after each passage.

$$\text{Therefore } S_a = 1 - f = 1 - \exp[-\pi/(r_0 |\sin \omega_m t|)]$$

2) $\omega_m T_1 \gg 1$. The exponential parts of the curve of Z against t can be taken as linear, giving

$$S_a = \left\{ 2t - 2 \exp[-\pi/(r_0 |\sin \omega_m t|)] (t + \pi) \right\} / \omega_m T_1$$

3

$\beta) r_0 \ll 1$. The spin packet is saturated ($Z \rightarrow 0$) at each passage,

i.e. $f = 0$

$$S_a = 1 - \exp \left[-(2\pi/\omega_m - 2t)/T_1 \right]$$

If it is now assumed that the density of spin packets over the width of the field modulation is uniform (a condition which, in the case of normal operation, would give no signal) the resulting signal at time t will be S_a times the rate at which the spin packets are being covered, i.e. $\rho A \omega_m |\sin \omega_m t|$ where ρ = density of spin packets.

Therefore
$$\text{Signal} = K S_a |\sin \omega_m t|$$

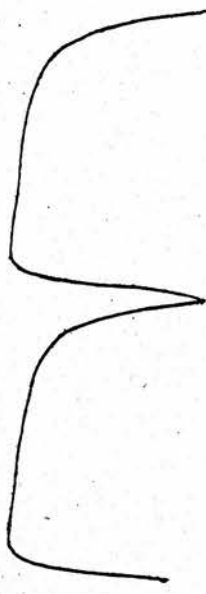
The point arising at this stage is that S_a only exists from $t = 0$ to $t = \pi/\omega_m$; beyond this point it becomes S_b from $t = \pi/\omega_m$ to $2\pi/\omega_m$. However, the shape of S_b in this range is exactly the same as S_a , so that S_a is in effect repeated twice every cycle. But $|\sin \omega_m t|$ also repeats twice every cycle, so that the resulting signal does also. In other words, the signal consists only of even harmonics of the modulating frequency. The calculated shape of the signal is shown for four cases in Figure 3.3 (c.f. the experimental signals from diamond, Figure 7.6). The existence of this even harmonic signal is useful experimentally, in that it can indicate the presence of a very wide inhomogeneously broadened line which might otherwise not appear in a derivative recording spectrometer.

3.5 Combined Effect of Field Modulation and Field Sweep.

This problem is most easily dealt with in the case where $\omega_m T_1 \gg 1$. Here the polarisation of any given spin packet does not alter much from



$$\omega_m T_1 = 1.0, \quad \gamma_0 = 0.5$$



$$\omega_m T_1 = 1.0, \quad \gamma_0 = 10.0$$



$$\omega_m T_1 = 1.0, \quad \gamma_0 = 2.0$$



$$\omega_m T_1 = 50, \quad \gamma_0 = 2.0$$

FOUR EXAMPLES OF EVEN - HARMONIC SIGNALS

Figure 3.3

one cycle to the next, but only gradually as the field modulation passes over it. Let the magnetic field be

$$H = H_0 + A (\cos \omega_m t + t/\tau) \quad (3.3)$$

and the spin packet under consideration be at H_0 . Over the period of one cycle at the approximate time t , the spin packet is subject to two passages and a certain amount of relaxation. Since the change in Z is small, it can be expressed as a first order difference

$$\Delta Z = 2Z [f(r) - 1] + 2\pi(1 - Z)/\omega_m T_1 \quad (3.4)$$

The value of r for the passage is found by setting $H = H_0$ in 3.3. This gives $t/\tau = -\cos \omega_m t$. Now

$$\begin{aligned} r &= r_0 \sin \omega_m t \\ &= r_0 \sqrt{(1 - [t/\tau]^2)} \end{aligned}$$

Since ΔZ is small, $f(r) = 1$, and hence $r \gg 1$, and to a first approximation

$$f(r) - 1 = -\pi/r$$

Thus 3.4 becomes

$$\Delta Z = -2\pi Z / (r_0 \sqrt{1 - (t/\tau)^2}) + 2\pi(1 - Z)/\omega_m T_1$$

The point on the cycle where passage occurs may be specified by an angle θ , where $\cos \theta = -t/\tau$. The fractional change of θ from one cycle to the next is therefore

$$\Delta \theta = \frac{\Delta \theta}{\Delta \cos \theta} \cdot \Delta \cos \theta = 2\pi/\omega_m \tau \sin \theta$$

Hence
$$\Delta Z/\Delta \theta = -Z \omega_m \tau / r_0 + \tau(1 - Z) \sin \theta / T_1 \quad (3.5)$$

It is to be noted that only the first term in the expression for ΔZ in equation 3.4 represents the signal, since the other term is due to relaxation. Furthermore, the process of phase-sensitive detection employed in the spectrometer only selects the fundamental frequency component of this signal, and only that component which is in phase with the modulation. This can be done mathematically by multiplying by $\cos \theta$, that is

$$\text{Signal } S = - 2\pi Z \cot \theta / r_0 \quad (3.6)$$

The apparently infinite value of the signal at $\theta = 0$ is due to the assumption of a spin packet having zero width. Its presence does not however invalidate the calculation.

Let the density of spin packets in the neighbourhood of H_0 be

$$\rho = \alpha + \beta(H - H_0)$$

Therefore, near $t = 0$, the field will be covering spin packets at a rate

$$\rho |dH/dt| = \rho A \omega_m |\sin \theta|$$

The signal due to all the spin packets is therefore

$$\begin{aligned} S &= \int_{-A}^{+A} 2\pi Z \rho A \omega_m \cos \theta dt / r_0 \\ &= \frac{2\pi A}{r_0} \left[\alpha \int_0^\pi Z \cos \theta d\theta + \beta A \int_0^\pi Z \cos^2 \theta d\theta \right] \end{aligned}$$

It can now be seen that the total signal consists of two components,

namely a term in α , representing the actual density of spin packets at $H = H_0$, and a term in β , representing the gradient of the density, that is, the derivative spectrum. In the absence of saturation (i.e. at very low power levels), Z is very nearly constant at 1, and the term in α vanishes, leaving only the derivative spectrum. The ratio of the coefficient of βA to the coefficient of α defines an "integration constant" (T_I) which can be calculated as a function of the two parameters

$$\lambda = \omega_m \tau / r_0$$

which may be called the "sweep parameter", and

$$T_0 = T_1 / \tau$$

the normalised relaxation time. The signal may be written

$$\begin{aligned} s &= \frac{2\pi A}{r_0} \left[\alpha I_1 + \beta A I_2 \right] \\ &= \frac{2\pi A}{r_0} I_1 \cdot \rho + \frac{2\pi A^2}{r_0} I_2 \cdot d\rho/dH \end{aligned} \quad (3.7)$$

where $I_2 / I_1 = T_I = T_I(\lambda, T_0)$

Written in terms of λ and T_0 , equation 3.5 becomes

$$dz / d\theta = -\lambda z + (1 - z) \sin \theta / T_0 \quad (3.8)$$

From the solution of this differential equation, the two integrals

$$I_1 = \int_0^\pi z \cos \theta \cdot d\theta$$

and $I_2 = \int_0^\pi z \cos^2 \theta \cdot d\theta \quad (3.9)$

may be calculated, and hence T_I . This is done numerically in section

3.8. Equation 3.8 can be solved analytically when T_0 is very large, i.e. when $T_I \rightarrow \infty$. It becomes

$$dz / d\theta = - \omega_m \tau z / r_0 \quad \text{whose solution is}$$

$$z = \exp \left[-\omega_m \tau \theta / r_0 \right] \quad \text{and leads to}$$

$$I_1 = \frac{\lambda}{(\lambda^2 + 1)} (1 + e^{-\lambda \pi})$$

$$I_2 = \frac{(\lambda^2 + 2)}{\lambda(\lambda^2 + 4)} (1 - e^{-\lambda \pi})$$

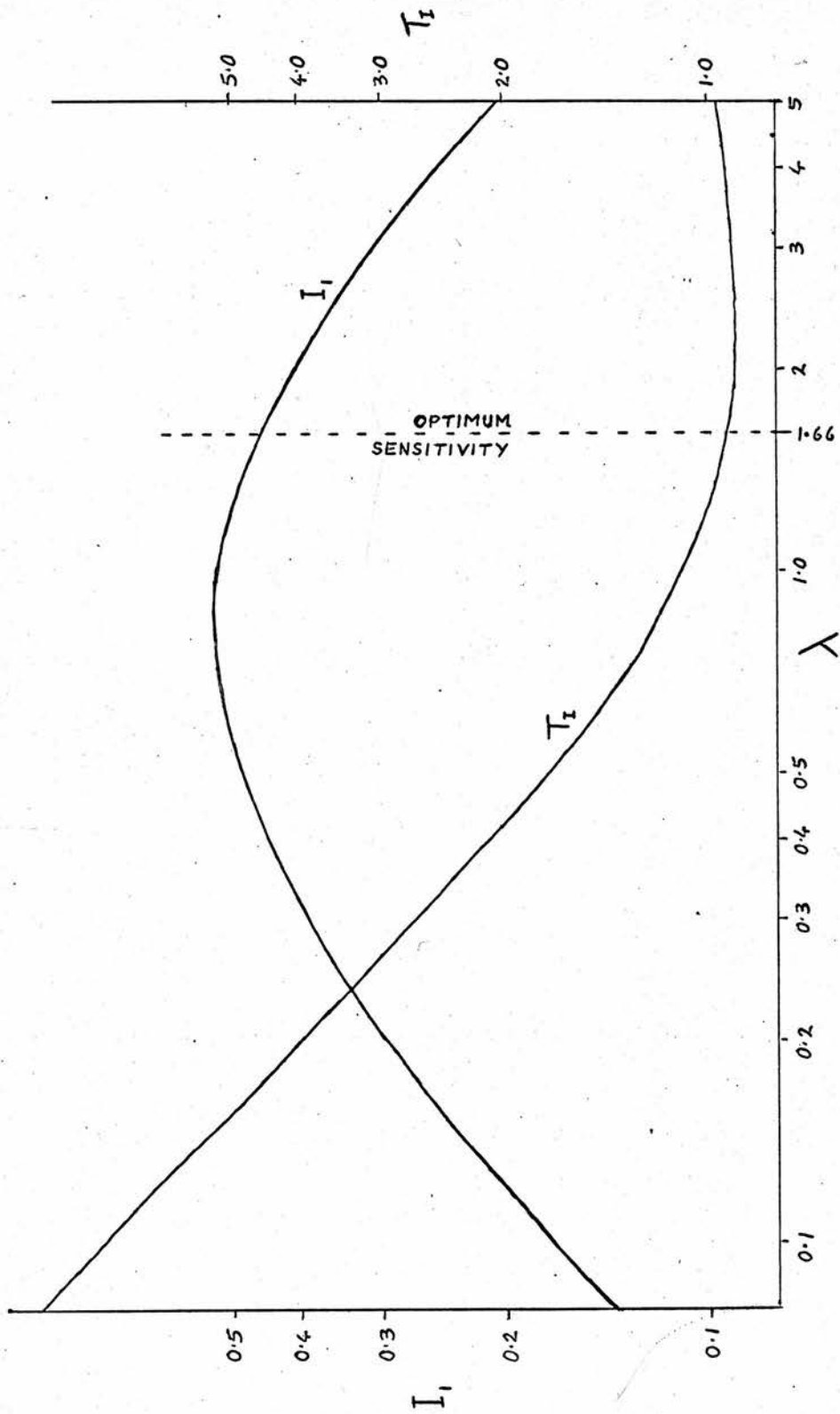
$$\text{and} \quad T_I = \frac{(\lambda^2 + 1)(\lambda^2 + 2)}{\lambda^2(\lambda^2 + 4)} \tanh(\pi\lambda/2) \quad (3.10)$$

$$\text{where} \quad \lambda = \omega_m \tau / r_0$$

The function $T_I(\lambda)$ as expressed in 3.10 is plotted in Figure 3.4 using logarithmic axes. For very small λ , $T_I \rightarrow \pi / 2\lambda$, and for large λ , $T_I \rightarrow 1$.

The significance of the partial integration of the signal can be seen on considering a very wide spectrum, where $d\rho/dH$ may be very small. It might be thought that by increasing A , the modulation depth, a greater signal could be obtained, but two factors in particular limit this possibility.

1) Although the term in $d\rho/dH$ in equation 3.7 contains A^2 , r_0 is also proportional to A , for a given power level, so that only a factor of A is gained.



VARIATION OF T_I & I_I WITH λ WHEN $T_o \gg 1$

Figure 3.4

2) The modulation depth, A , which can be conveniently used is generally restricted by experimental limitations such as vibrational pickup and available modulating power.

In the calculations so far, it has been assumed that the incident microwave power, and hence H_1 , is fixed. The effect of varying the power level will now be treated.

3.6 Dependence of Signal on Power Level.

The sensitivity of the spectrometer to a given spin transition depends on the microwave power level. The case when no passage effects occur (for example, at room temperature) has been extensively treated by Feher (Ref. 30). In the present work, however, passage effects do occur, and the fact that T_1 is very much longer than any passage times is very useful, since it implies that the energy absorbed from the microwave field by a spin packet can be equated to the energy change of the spin packet during passage.

Assuming a nearly critically coupled cavity, the signal to noise ratio (S_n) obtainable for a given R.F. susceptibility (χ'') is proportional to the square root of the incident power (P); that is, proportional to H_1 . Now $\chi'' = M_y / 2 H_1$, therefore

$$\begin{aligned} S_n &\propto H_1 |\chi''| \\ &= \frac{1}{2} |M_y| \\ &= \frac{1}{2 \gamma H_1} \left| \frac{dM_z}{dt} \right| \end{aligned}$$

from equations 2.5, if T_1 is much longer than the time of passage. But in the absence of spin-lattice relaxation, dM_z/dt is just the rate of induced spin transitions. Therefore, for a given rate of spin transitions,

$$S_n \propto H_1^{-1} \propto P^{-\frac{1}{2}}$$

However, a number of other factors change when the power level is changed. In particular, r_0 is inversely proportional to power level. Applied to equation 3.7, this would indicate that $S \propto P$ and hence that the overall signal to noise ratio, S_n , was proportional to $P^{\frac{1}{2}}$, but the integrals I_1 and I_2 are also dependent on r_0 . When considering ultimate sensitivity for a given spin system, it must be decided which type of signal is being observed. Since the discussion is centred on wide lines, it will be more useful to consider the "integrated" part of the signal; that is, the part

$$S_1 = 2\pi A \rho I_1 / r_0 = 2\pi \gamma H_1^2 I_1 \rho / \omega_m \propto P I_1 \rho / \omega_m$$

It can be assumed that A is constant for, as indicated earlier, A is merely limited by experimental conditions. Now

$$\lambda = \omega_m \tau / r_0 = \gamma H_1^2 \tau / A \propto P \tau$$

The signal to noise ratio $\propto S_1 P^{-\frac{1}{2}}$, but the bandwidth of the signal recorder need not be greater than $1 / 2\tau$, since the resolution of the signal is only of the order of τ . Since (in an ideal system at least) noise level is proportional to the square root of the bandwidth, this leads to a signal to noise ratio

$$S_n \propto S_1 P^{-\frac{1}{2}} \tau^{-\frac{1}{2}} \propto P^{\frac{1}{2}} \tau^{\frac{1}{2}} I_1 \rho / \omega_m \propto \lambda^{\frac{1}{2}} I_1 \rho / \omega_m$$

The factor $\lambda^{\frac{1}{2}} I_1$ has a maximum at $\lambda = 1.66$, as can be deduced from Figure 3.4, but it would appear at first sight that the $1/\omega_m$ term would lead to any desired sensitivity by making ω_m small enough. This, however, is due to the fact that the signal here is integrated over one cycle of the modulation, whose length is proportional to $1/\omega_m$. If the signal were integrated over real time, the $1/\omega_m$ term would disappear. However, there exists one approximation which could give rise to error when ω_m is reduced: that is the assumption

$$f(r) = 1 - \pi / r$$

In fact when r is not large, $f(r)$ is less than this value, indicating a decrease in sensitivity at small ω_m . The value $\lambda = 1.66$ is only an optimum when $r_0 \gg 1$. When this condition is not fulfilled, equation 3.5 cannot be derived from 3.4. The case when r is not large will be treated in the next section.

3.7 Saturating Passage.

In this case the exact value of $\omega_m \tau$ is significant, for it determines what the value of r is likely to be on the first passage through the spin packet. If dH/dt is zero, that is, the spin packet lies at a turning value of the field, passage conditions no longer exist, but if H_1 is sufficiently large, complete saturation will occur ($\Delta Z = -1$). If also $T_1 \gg \tau$, the spin packet will not give rise to any further signal. Each successive cycle will saturate the spins within a range of field $2\pi A / \omega_m \tau$, giving rise to a signal $2\pi A \rho / \omega_m \tau$, which is the

same as that obtained by making λ large, whence $I_1 \rightarrow \lambda^{-1}$, showing that the approximation is not serious.

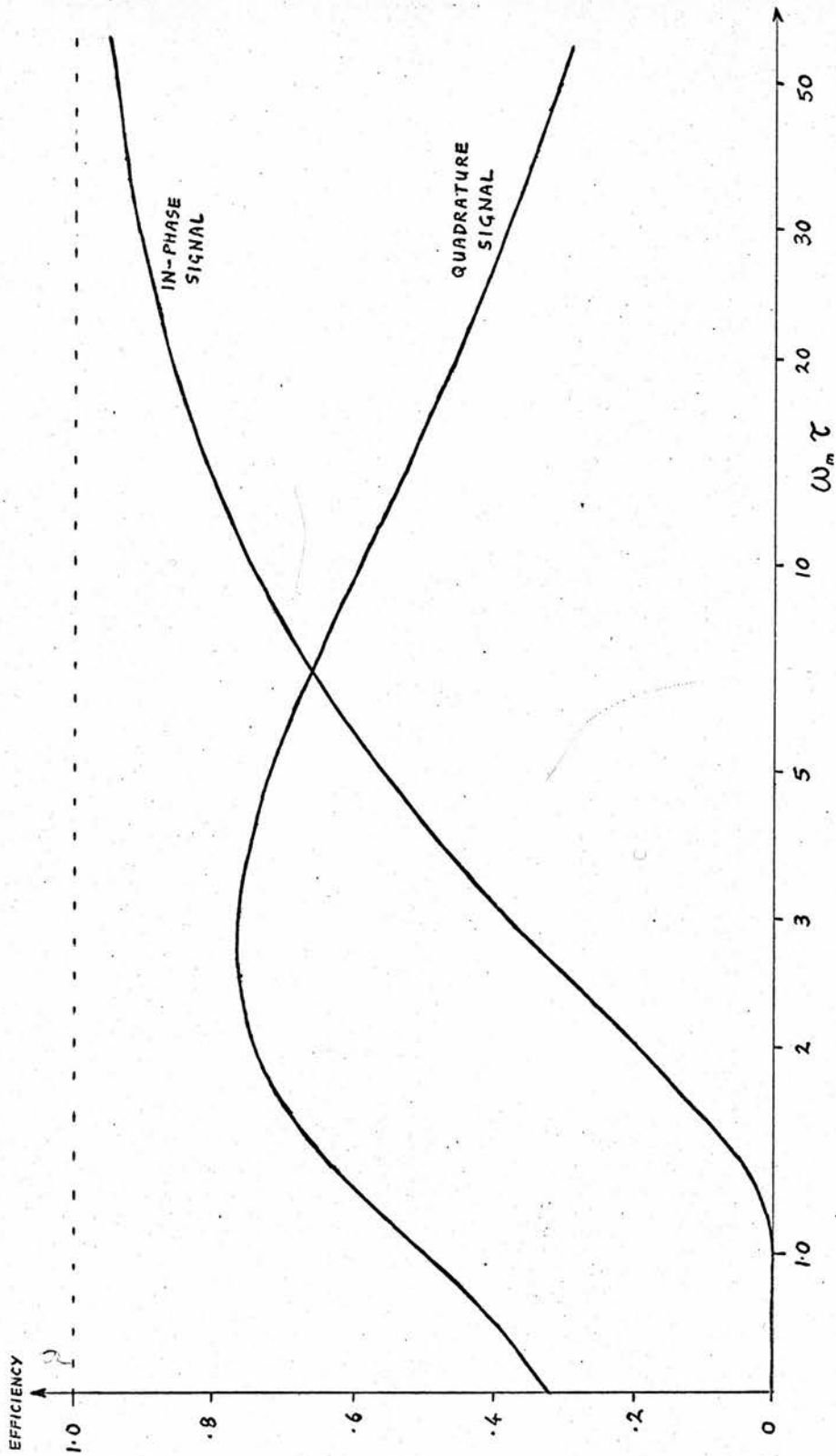
However, it has been assumed that all spin packets are saturated at or near $\theta = 0$, but this is only true when $\omega_m \tau$ is large. As $\omega_m \tau$ decreases, so the angle over which unsaturated spins are encountered increases until at a critical value $\omega_m \tau = 1$, spins are encountered at all angles, since the field variation becomes unidirectional. The extent to which a spin packet contributes to the final signal is proportional to $\cos \theta$, by virtue of the phase sensitive detection process. Spins undergoing passage at $\theta \neq 0$ will not contribute efficiently to the final signal. The relation between overall efficiency and $\omega_m \tau$ is shown in Figure 3.5 and it is seen that it falls off sharply as $\omega_m \tau$ approaches unity. By shifting the phase of the reference signal in the phase sensitive detection process by 90 degrees, the system can be made to give the "quadrature" signal, that is, where the contribution to the final signal is proportional to $\sin \theta$, and this component is also shown in Figure 3.5. It exceeds the "in-phase" signal when $\omega_m \tau < 1$. The phase angle of the signal varies considerably with $\omega_m \tau$, being 90 degrees leading at $\omega_m \tau = 1$, and decreasing as $\omega_m \tau$ increases.

When $\omega_m \tau \leq 1$, it is no longer necessary to specify $f(r) = 0$, since

$$r = r_0 (\sin \omega_m t + \omega_m \tau)$$

is always positive, so that the signal integral is

$$\int_0^{2\pi} \rho \cos \theta \cdot f(\sin \theta + \omega_m \tau) d\theta = 0$$



VARIATION OF SIGNAL DETECTION EFFICIENCY
(SATURATING PASSAGE)

Figure 3.5

for any function f , indicating that the signal is entirely in quadrature. Neither is the restriction $T_1 \gg \tau$ necessary, as no spin packet undergoes passage more than once. The region is, however, quite unsuitable experimentally, because it represents much too fast a sweep rate.

The overall picture, then, is that $\omega_m \tau$ should be fairly large, say greater than 10 for maximum sensitivity in the case of saturating passage. However, saturating passage does not give the best sensitivity, since the power level required is too high, and the sensitivity factor $\lambda^{\frac{1}{2}} I_1$ is lower than its maximum. The condition $\lambda = 1.66$ is only optimum when $T_0 \rightarrow \infty$.

3.8 Computer Solutions.

In order to obtain a comprehensive set of solutions to equations 3.8 and 3.9, the IBM 1620 computer was again employed. The program constructed is shown in Figure 3.6 and the solutions displayed as contour maps of I_1 , I_2 and T_I against λ and T_0 in Figures 3.7, 3.8, and 3.9 respectively. The axes are logarithmic. Within the program, ALPHA represents the normalised relaxation rate (T_0^{-1}) and BETA represents λ . Four quantities are read in:

T1I = lowest value of T_0

NT = number of points in the T_0 direction

BETA = lowest value of λ

NB = number of points in the λ direction

The points are spaced logarithmically at intervals of $\sqrt[5]{10}$ for

```
C INTERMEDIATE PASSAGE. MODULATION+LINEAR SWEEP.
C WM*T1 LARGE.
DIMENSION CN(100),SN(100)
T=.005
DO1 I=1,100
CN(I)=COSF(3.14159*T)
SN(I)=SINF(3.14159*T)
1 T=T+.01
READ 4, T1I,NT,BETA,NB
4 FORMAT(2(E10.3,I2))
R=10.0**0.2
DO 5 J=1,NB
E=0.031416*BETA
T1=T1I
DO 6 K=1,NT
ALPHA=0.031416/T1
Z=1.0
S1=0.
S2=0.
DO 2 I=1,100
99 Z=Z+(1.0-Z)*ALPHA*SN(I)-E*Z
Q=Z*CN(I)
S1=S1+Q
2 S2=S2+Q*CN(I)
TI =S2/S1
S1=S1*.031416
S2=S2*.031416
PRINT 3,T1,BETA,S1,S2,TI,Z
3 FORMAT(9H FOR T1=E10.3,8H @ BETA=E10.3,4H I1=F8.5,
1 4H I2=F8.5,4H TI=E10.3,4H ZF=F6.4)
6 T1=T1*R
PRINT 7
7 FORMAT(/)
5 BETA=BETA*R
CALL EXIT
END
```

CONTOUR MAP OF I_1 AGAINST λ & T_0

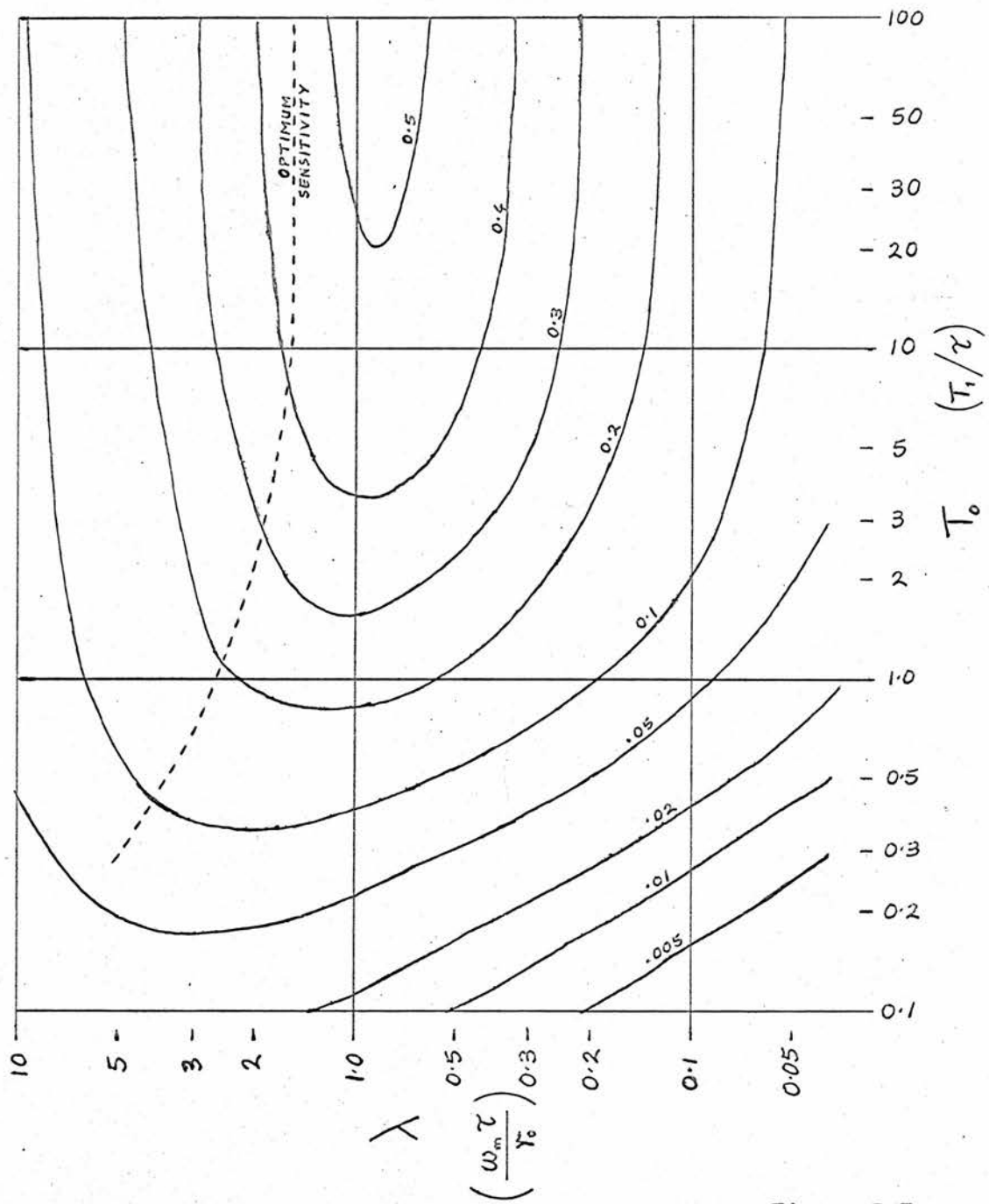


Figure 3.7

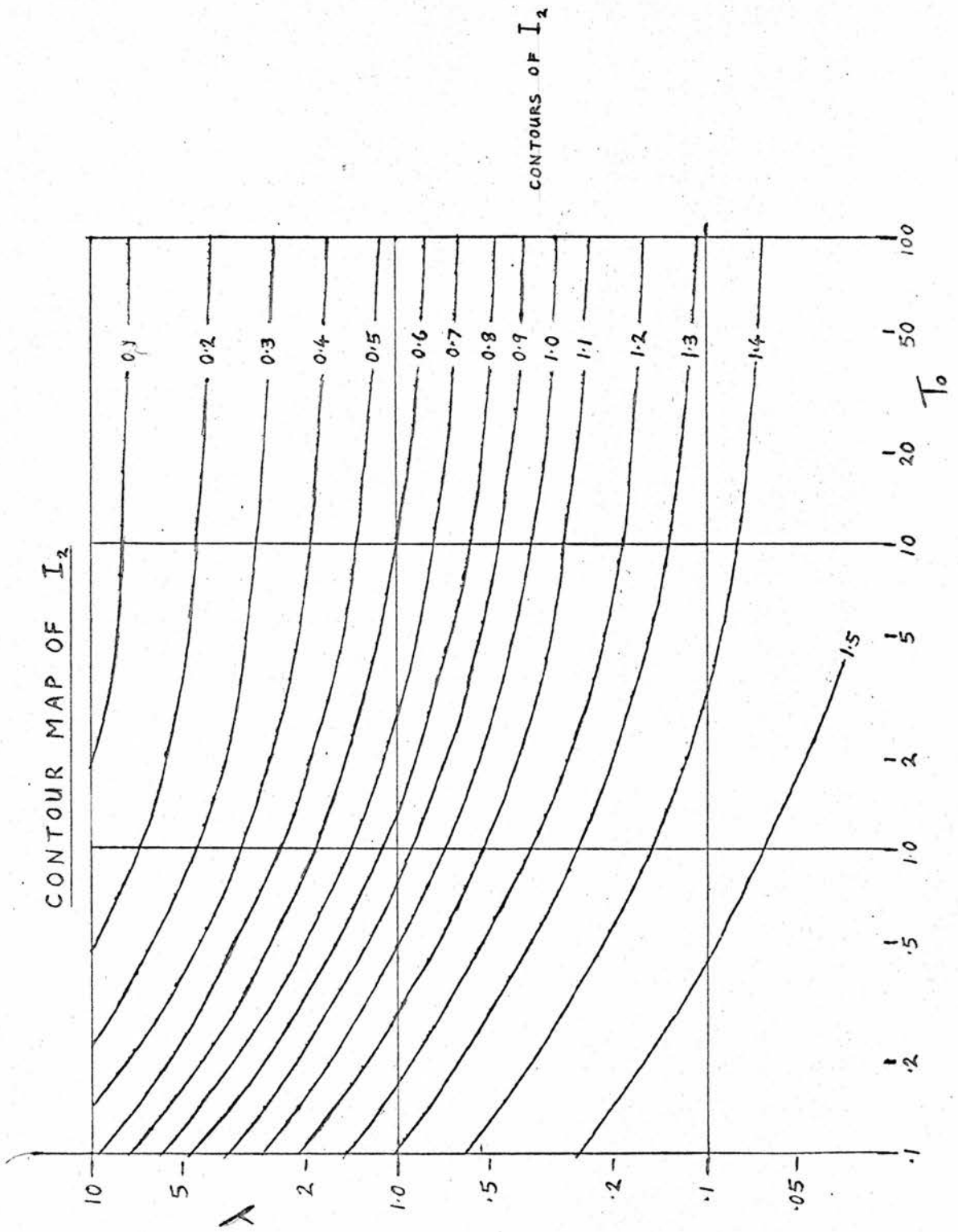


Figure 3.8

CONTOUR MAP OF T_I AGAINST λ & T_0

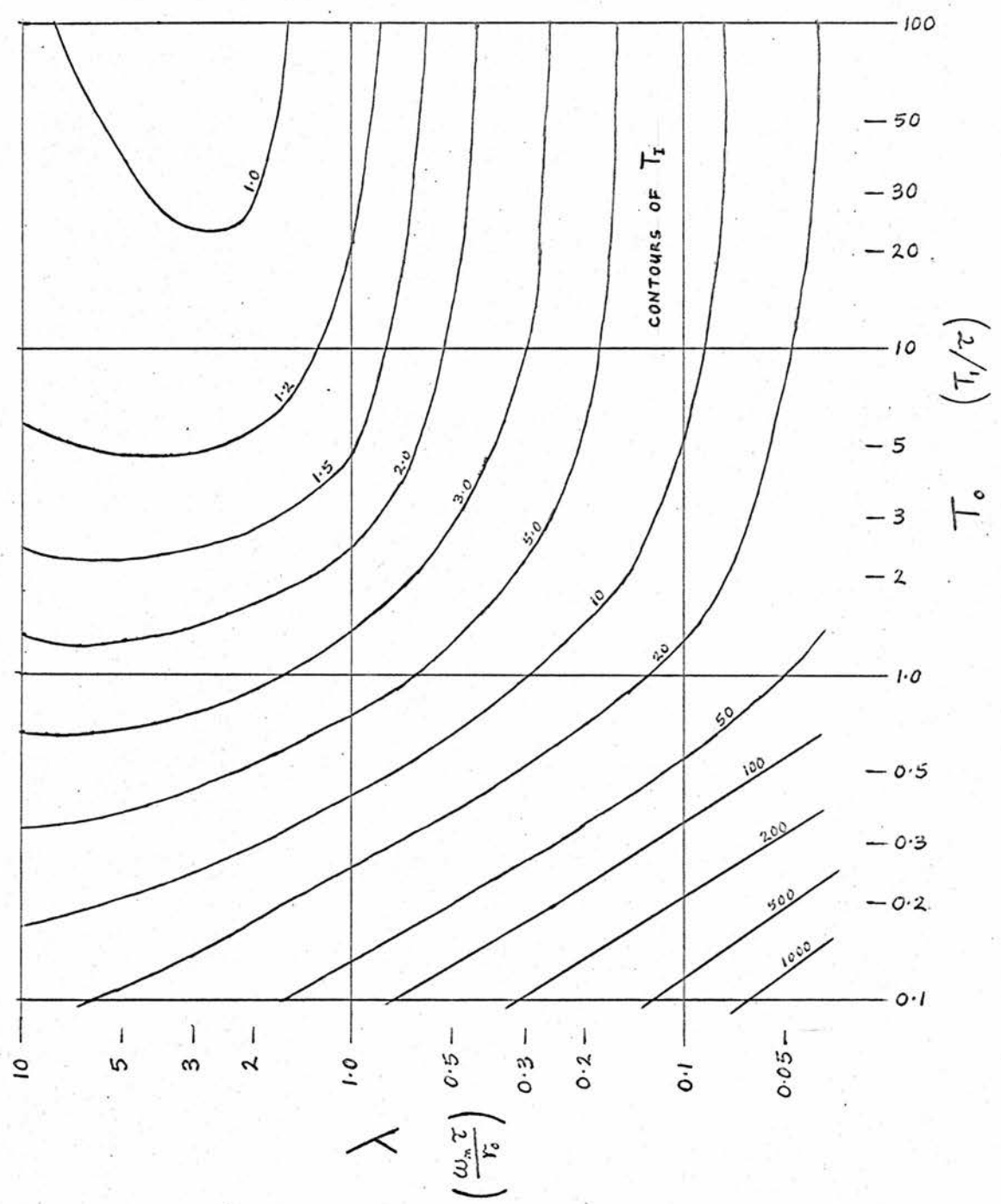


Figure 3.9

convenience of plotting. All the values of the trigonometric functions used in the program are computed in advance to save computer time. The interval of θ chosen was 1.8 degrees, giving 100 points over the range ($\theta = T$ in the program). This limits the validity of the calculation to the range $\lambda < 10, T_0 > 0.1$; more points and hence longer computing time would be required to extend this range.

The locus of the maximum value of $\lambda^{\frac{1}{2}} I_1$ for a given T_0 can be found from Figure 3.7 and is plotted in Figure 3.10. The optimum value of λ rises sharply as T_0 is reduced, but this occurs in a region where T_1 is also increasing sharply, indicating that the term in I_2 is becoming important. In this region, theoretically at least, sensitivity can be increased indefinitely by increasing τ and allowing the apparatus to behave as a derivative spectrometer. The case for maximising $\lambda^{\frac{1}{2}} I_1$ is only valid when T_1 is uncomfortably long (e.g. silicon, section 6.2) or where the spectrum is so wide that the term in I_2 is negligible.

The other feature to be noted is the rapidity with which I_1 vanishes as T_0 is reduced. This means that in order to observe the "integration" effect, τ must not be much greater than T_1 .

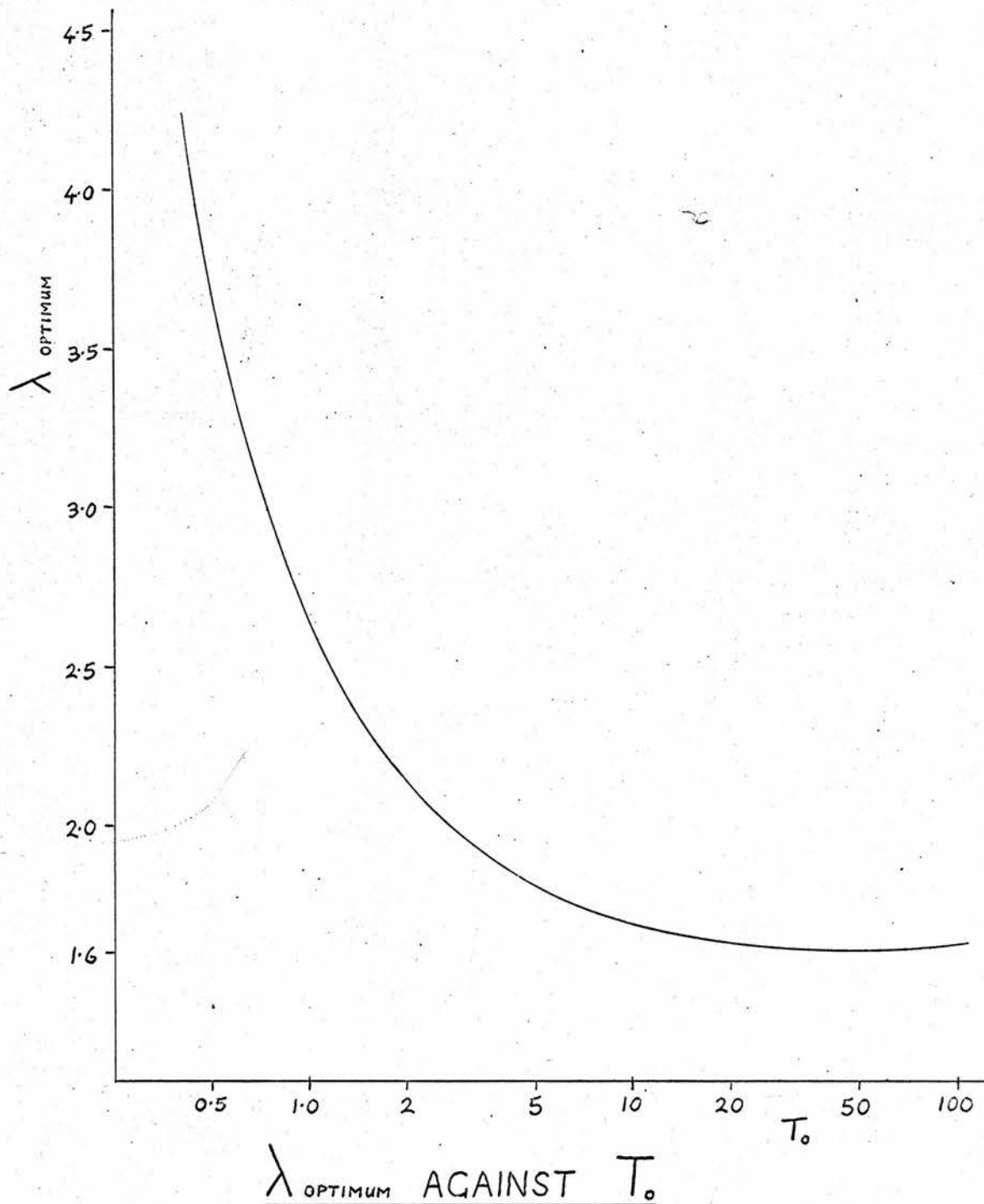


Figure 3.10

CHAPTER 4

THE APPARATUS.4.1 Introduction.

The apparatus is basically a reflection cavity superheterodyne X-band spectrometer, with an additional pulsed klystron. It is derived from the apparatus used by Campbell (Ref. 10) and Firth (Ref. 11) and was designed with the aim of observing paramagnetic relaxation processes having relaxation times of the order of milliseconds at liquid helium temperatures. A photograph of the apparatus is shown in Figure 4.1 and a block schematic diagram in Figure 4.2. This is the basic apparatus, and the output of the second detector can be used in two distinct ways:

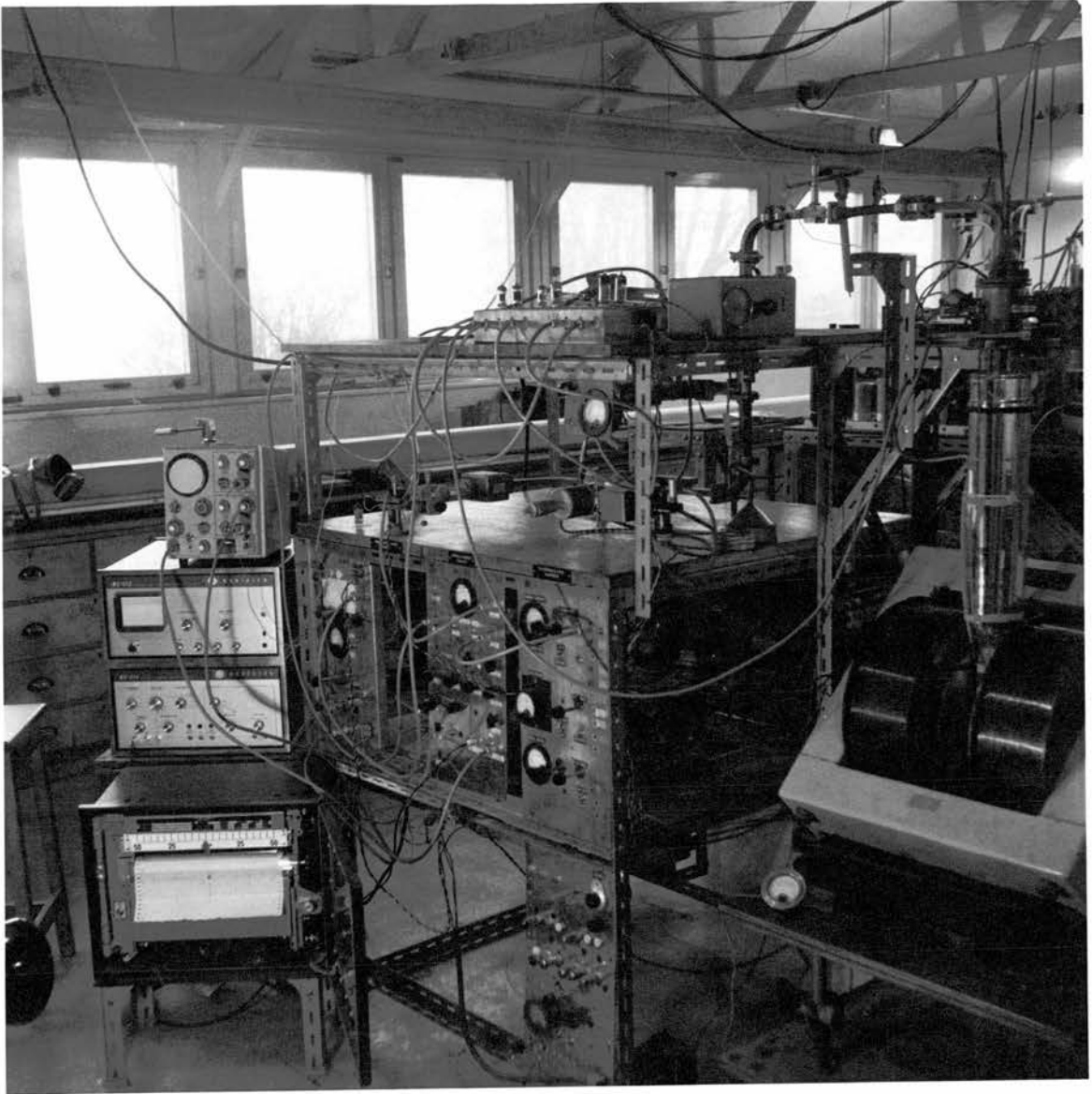
a) As a straight spectrometer. In this case the pulsed klystron is not used and the remainder of the apparatus is as shown in Figure 4.3, the "monitor" now being the signal klystron.

b) As a relaxation spectrometer (Figure 4.4). In this, the normal mode of operation, the spins are saturated or inverted by means of a short pulse of microwave power from the pulse klystron, and their subsequent recovery observed using a continuous low power signal from the monitor klystron.

It was decided to use valves as opposed to transistors in the electronics for the following reasons:

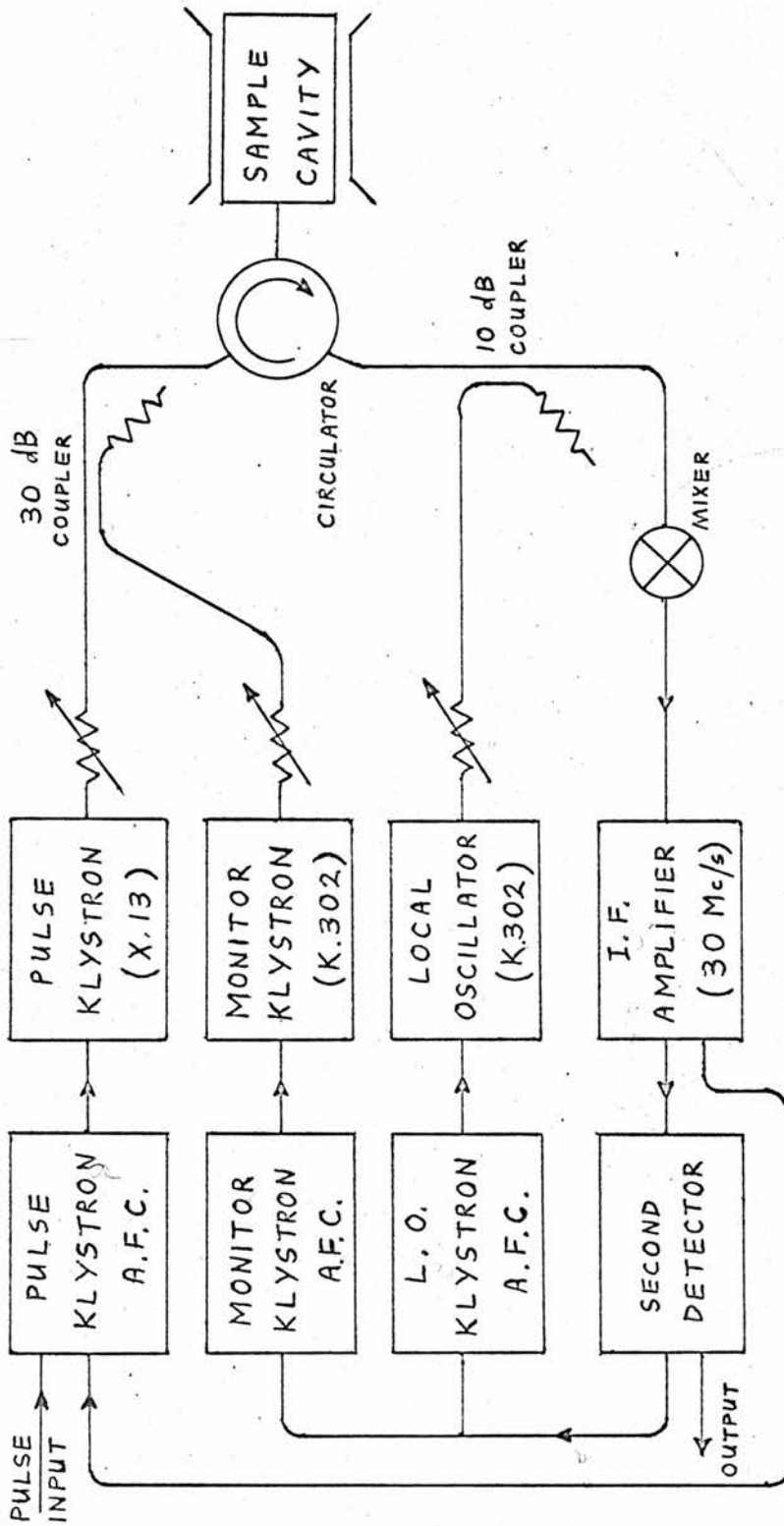
1) The existing power supplies, being high voltage, were more suitable for valves than transistors.

2) Many of the devices incorporated (for example, the gating and



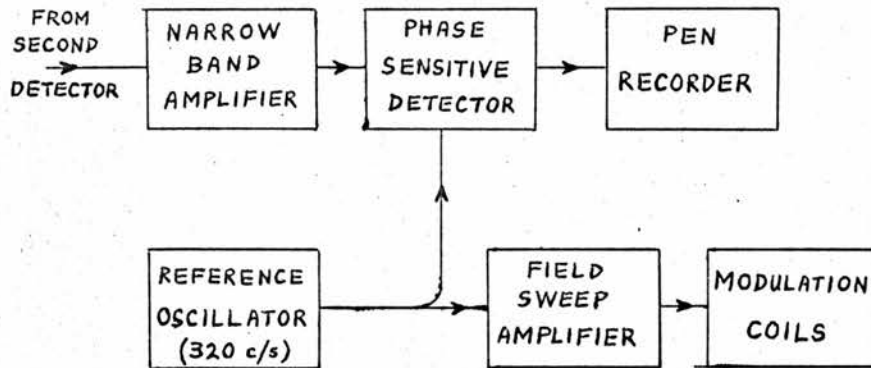
General View of the Apparatus.

Figure 4.1



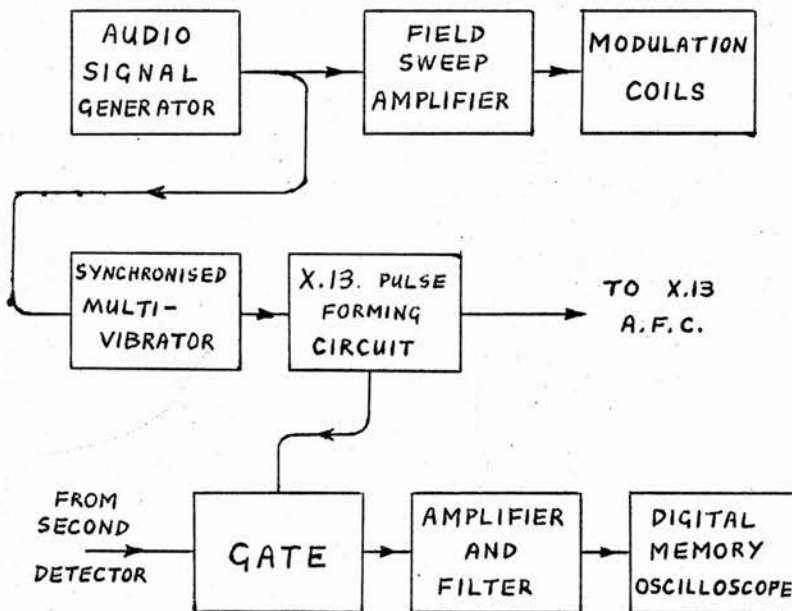
BLOCK DIAGRAM OF SPECTROMETER

Figure 4.2



THE APPARATUS AS A DERIVATIVE RECORDING SPECTROMETER

Figure 4.3



THE APPARATUS AS A RELAXATION SPECTROMETER

Figure 4.4

sampling circuits) depend for their operation on amplifying components having a very high input impedance. Transistors are not suitable for this purpose. Field-effect transistors could have been used, but these were unduly expensive at the time.

3) Valves are more robust electrically than transistors. The high voltages associated with klystrons constitute a definite hazard in this respect.

Use was made, however, of semiconductor diodes in many of the circuits.

4.2 Microwave Circuitry.

The microwave system, shown in block schematic form in Figure 4.2 is based on size 16 waveguide (0.9"x 0.4") and operates in the frequency range 9100 to 9500 Mc/s. The paramagnetic sample is mounted in the centre of a rectangular cavity, operating in H_{012} mode. The power reflected from the cavity is fed via a ferrite circulator to the first detector (mixer) where it beats with the local oscillator signal to produce a 30 Mc/s intermediate frequency (I.F.) signal. The pulse klystron is a Varian X.13, delivering up to 250 mW microwave power to the cavity via the circulator. The monitor klystron (K 302) couples into this section via a 30 db coupler, delivering about 10 microwatts maximum to the cavity. The circulator has the advantage of being much more efficient than the magic tee normally used in this position, having a total loss of only 1 db, as compared with 6 db for a magic tee. This is especially useful when it is necessary to use low monitor power. It also eliminates some awkward matching problems encountered with magic tees.

It was considered that no significant advantage would be obtained from the use of a balanced mixer. This is normally used to reduce modulation noise, which is only significant at somewhat higher signal powers, say approaching 1 mW, or in systems using a low intermediate frequency (e.g. 100 kc/s).

All the klystrons are immediately followed by ferrite isolators, except the X.13 pulsed klystron, where a sliding stub tuner is inserted between the klystron and the isolator, and adjusted for maximum power output.

The local oscillator and monitor klystrons are powered from a common -300 volt stabilised supply of standard design, while the X.13 klystron is powered from a similar -450 volt supply. The reflector potentials of all the klystrons are derived from an E.H.T. supply which is tied to the -300 volt line and delivers -1100 volts w.r.t. earth. A simple potentiometer system then provides the required potentials (-425 volts approx. for the monitor and local oscillator klystrons, and about -1000 volts for the X.13). These potentials are subsequently modified by the various A.F.C. systems, described later. All the klystron heaters are driven from 6 volt d.c. stabilised supplies.

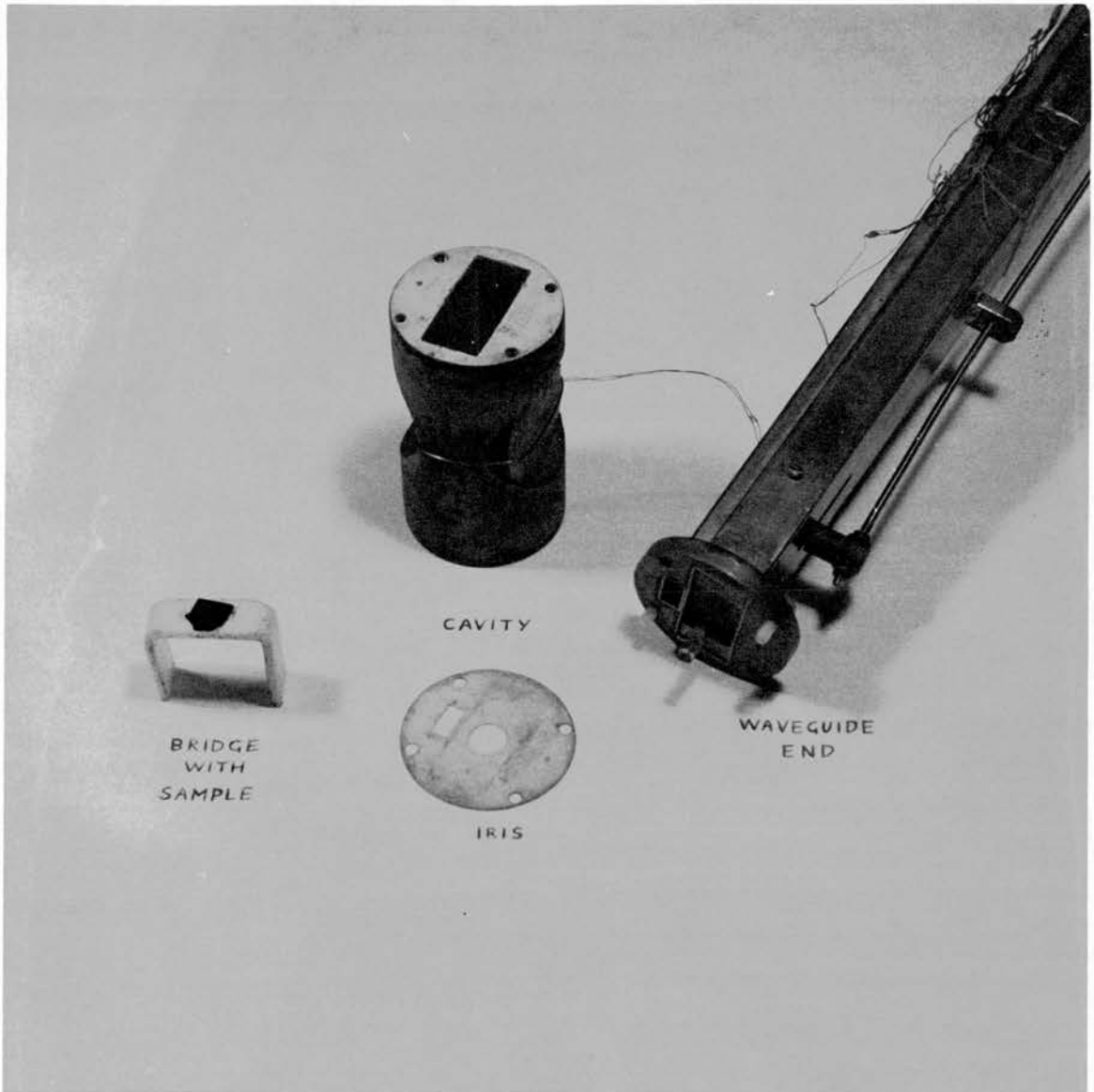
4.3 Cavity Design.

The microwave resonant cavity used was one of the "Araldite" epoxy resin mouldings made by Firth (as described in Ref. 31), but was re-silvered internally (Ref. 32) as the original coating was somewhat tarnished. Circular depressions were cut externally in each broad side

originally to take field modulation coils, but these were later abandoned and the space was used as the location of the field sweep search coil (section 4.9). After silvering, the internal surfaces were coated with a thin layer of nail varnish, which protects the silver from tarnishing and accidental scraping while inserting and removing samples. It gives no observable E.S.R. spectrum, nor does it affect the Q-factor of the cavity.

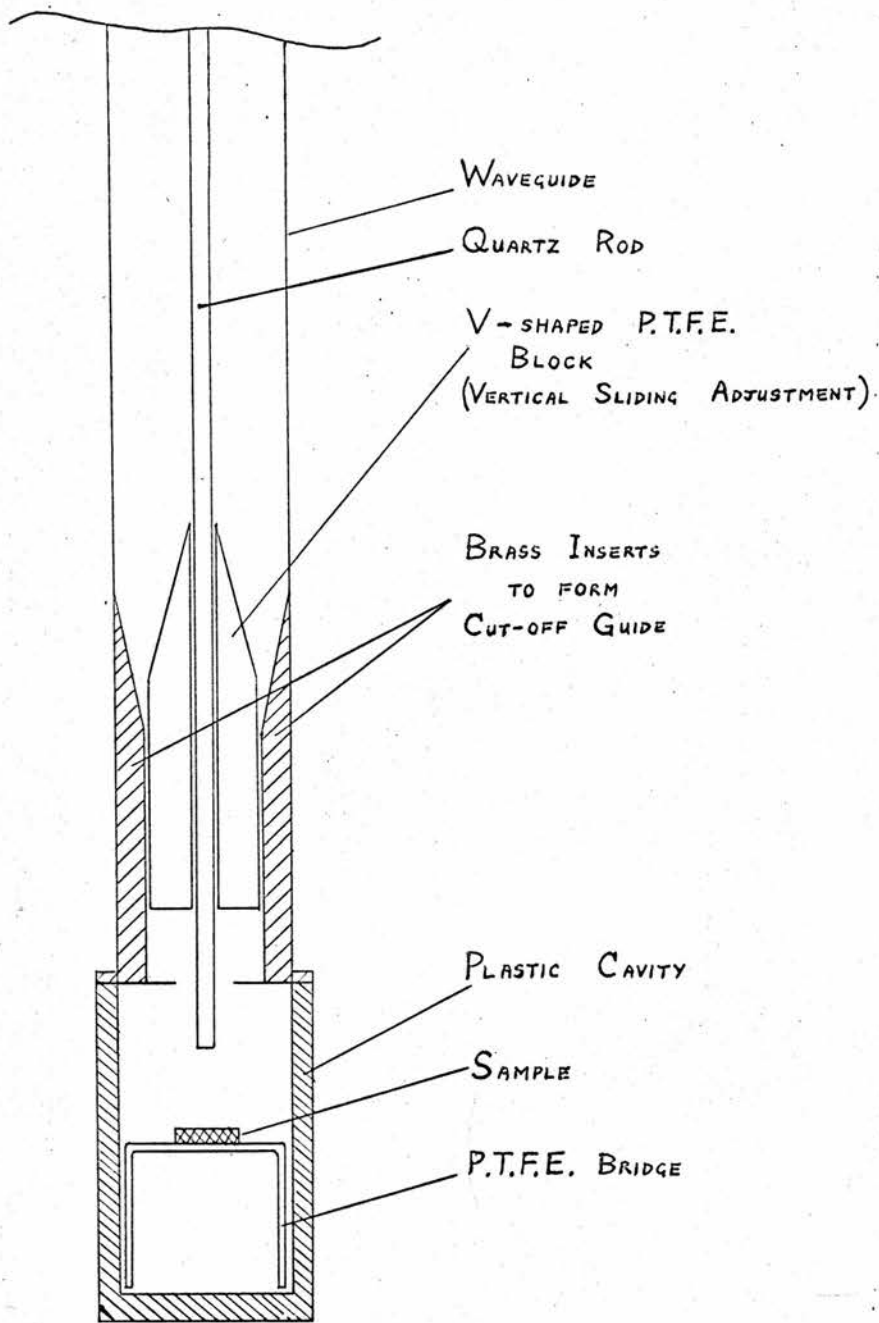
Samples were originally mounted on blocks of foam polystyrene, occupying half the cavity, but this was replaced by a solid P.T.F.E. bridge, shown in Figure 4.5. This bridge was designed to fit into the region of minimum electric field, and has the advantages that (a) it can be inserted or removed without scraping the cavity walls, as the foam mounting tended to do, and (b) it does not vary its size with pressure variations in the cryostat.

A variable coupler of the type described by Gordon (Ref. 42) has been installed. A vee-shaped block of P.T.F.E. moves in a short section of cut-off waveguide immediately before the cavity. The length of cut-off waveguide remaining between the end of the block and the coupling iris determines the reduction in coupling. The coupling iris is designed so that the cavity would normally be overcoupled. The arrangement is shown diagrammatically in Figure 4.6. Fine tuning is effected by means of a quartz rod passing down the centre of the waveguide, through the P.T.F.E. block and projecting a variable length into the E-field region of the cavity immediately above the sample. Both the quartz rod and the variable coupler are controlled from the top of the cryostat. One other alteration

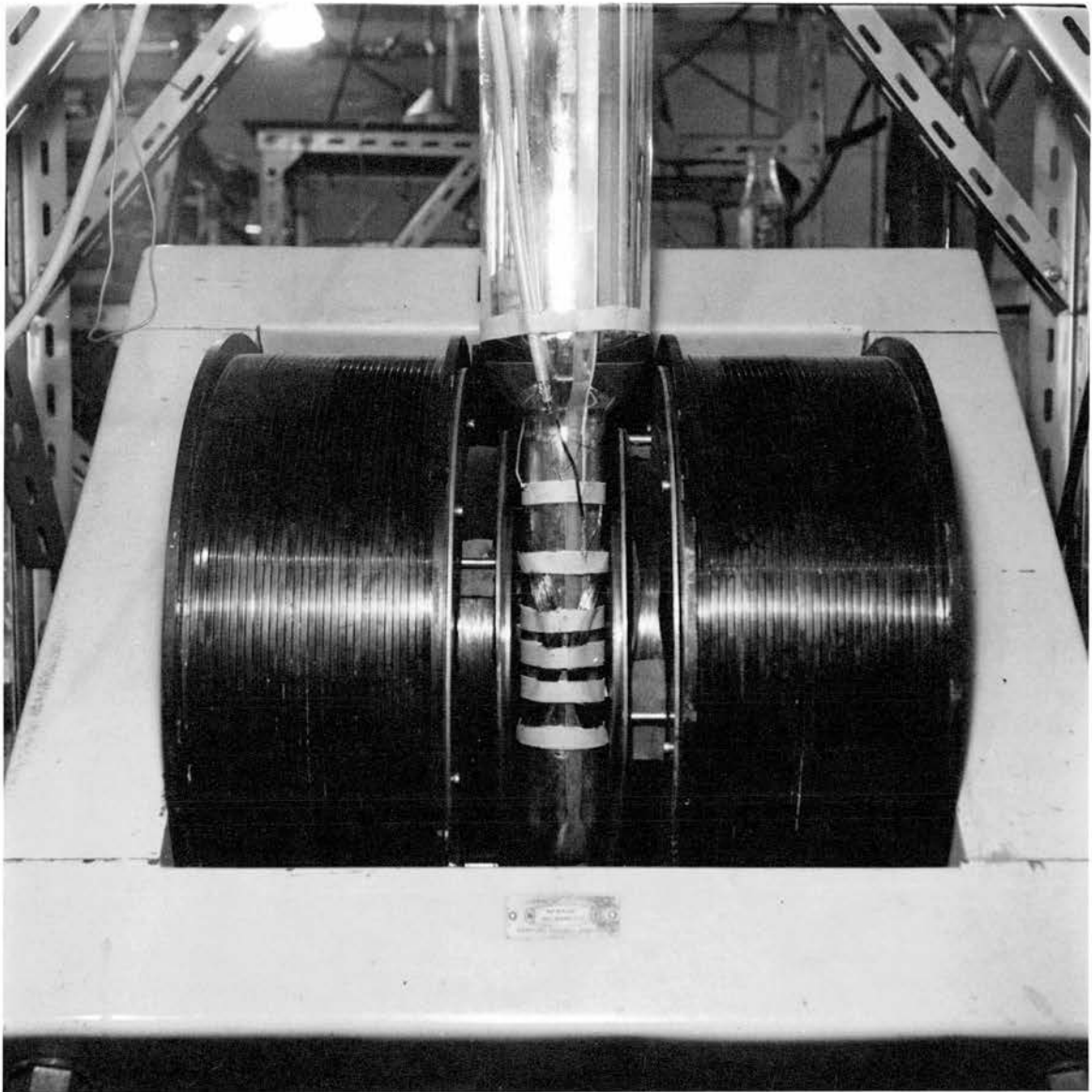


Resonant Cavity Details.

Figure 4.5



CAVITY AND VARIABLE COUPLER (DIAGRAM)



Cryostat Assembly between Magnet Poles,
showing Field Modulation Coils.

Figure 4.7

which has been made in the cryostat assembly is that the field modulation coils are now mounted on the outer (liquid nitrogen) dewar (see section 4.9). The cryostat assembly, in position between the poles of the magnet is shown in Figure 4.7. A fuller description of the cryogenics of the apparatus is given by Campbell and Firth (Refs. 10, 11).

4.4 Intermediate Frequency Amplifier.

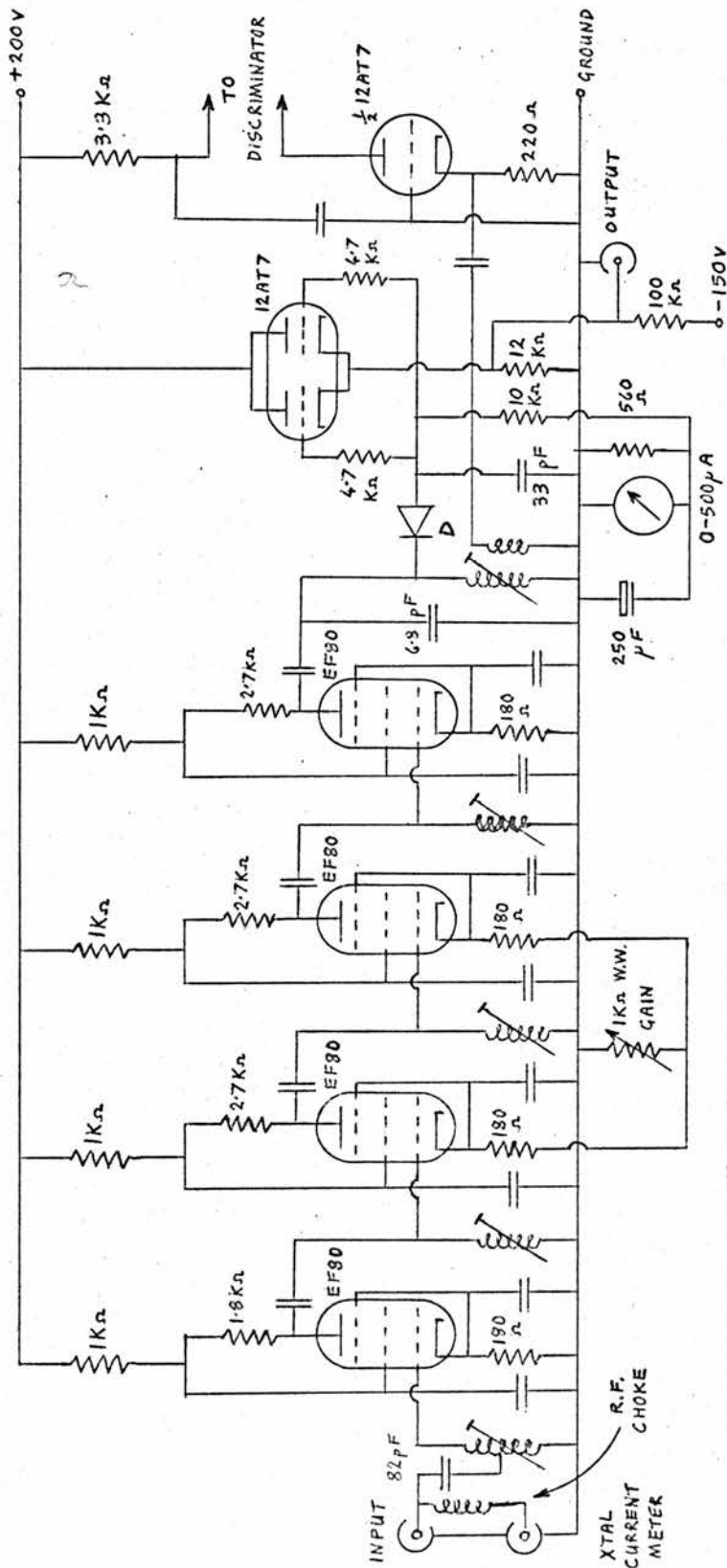
The circuit of this is shown in Figure 4.8. It was built specially for the apparatus, because the existing "Pye Strip" used by Campbell and Firth was found to be unsatisfactory in certain aspects. The design is fairly standard (Ref. 33) but one or two points deserve mention.

a) The amplifier was originally stagger-tuned to approximate to a four pole Butterworth flat-top response of 5 Mc/s bandwidth around 30 Mc/s, but this was found to be unsuited to the operation of the local oscillator automatic frequency control (L.O.A.F.C.) and was subsequently modified to synchronously tuned, with a bandwidth of about 3 Mc/s.

b) A gain control operates on the second and third valves. The first stage is left unaffected to ensure a good noise factor at reduced gain, and the last stage to avoid saturation. An overall gain variation of 20 db is obtained.

c) The detector is followed immediately by a cathode follower, giving an output impedance of about 100 ohms. A fraction of the I.F. signal is taken off at this point to a grounded grid buffer amplifier, from which the X.13. A.F.C. (section 4.6) is driven.

d) The crystal current meter may be replaced by an oscilloscope to



I.F. AMPLIFIER

ALL CAPACITORS .001 μF UNLESS OTHERWISE STATED
 D — HUGHES HIGH-SPEED SWITCHING SILICON DIODE
 TUNED INDUCTANCES ~ 1 μH

Figure 4.8

view the X.13 klystron mode for setting-up purposes (section 4.12). The local oscillator attenuator is adjusted to give a crystal current of 500 microamperes, this having been found to give the best overall noise figure.

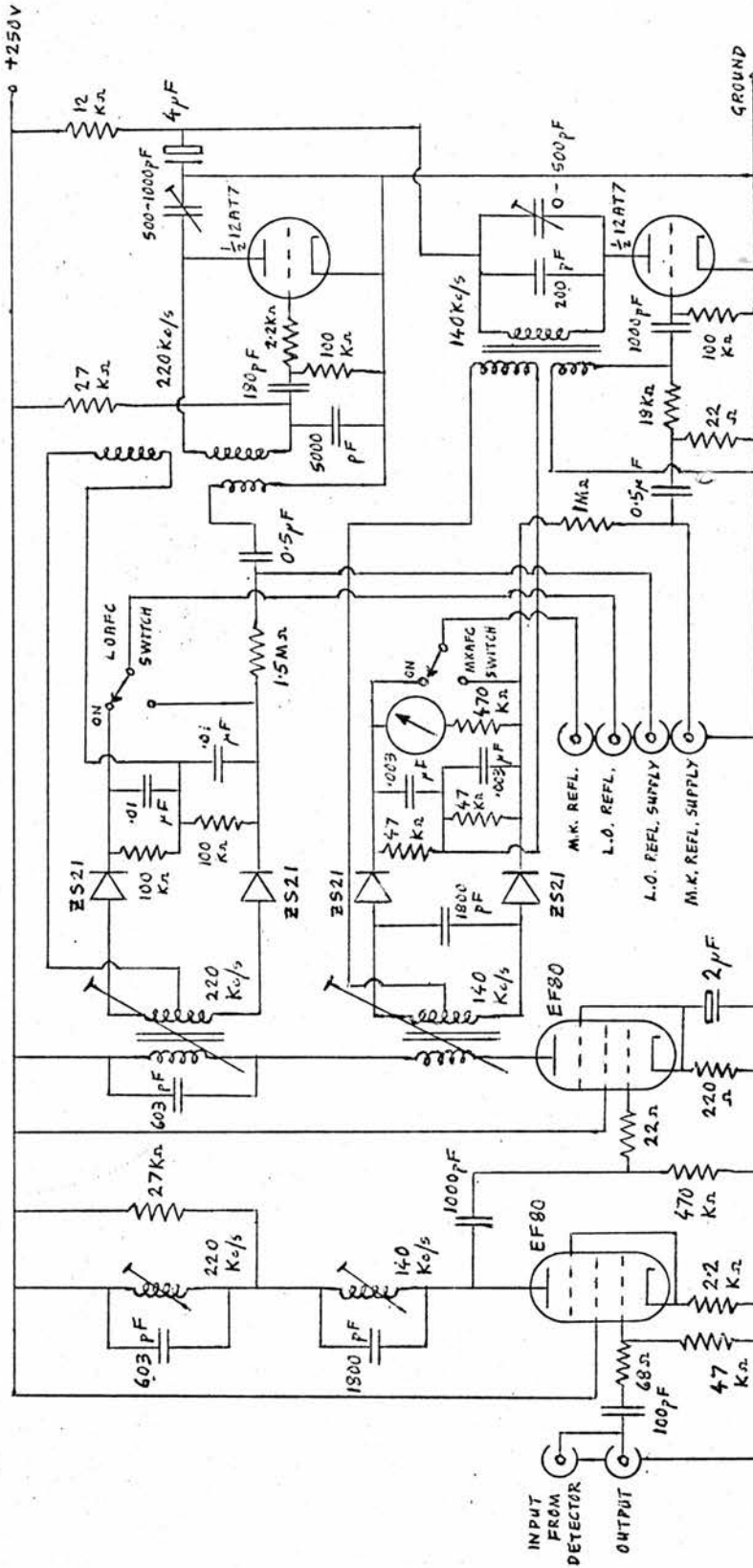
The overall maximum gain of the mixer plus I.F. amplifier is such that an input of 10^{-10} watts will give an output of 3 volts at the second detector. The second detector is in its most linear region at around 3 volts output.

The heaters of the I.F. amplifier are powered by direct current to reduce hum on the signal.

4.5 The Local Oscillator and Monitor Klystron A.F.C. Systems.

These both use the frequency modulation principle of the A.F.C. systems of Henning (Ref. 34) and Jung (Ref. 35). The circuit is shown in Figure 4.9.

Principle of Operation. The monitor klystron is frequency modulated at 140 kc/s, and the local oscillator at 220 kc/s by applying signals of those frequencies to their reflectors. These particular frequencies were chosen since they are high enough to be out of the range of most of the E.S.R. signals being observed, but low enough to avoid phase distortion by the I.F. amplifier. It is also advisable to have them harmonically unrelated in order that the two A.F.C. systems may operate independently. When the signal reflected from the cavity is mixed with the L.O. signal, a beat frequency of 30 Mc/s is produced, which will be frequency modulated at both 140 kc/s and 220 kc/s. Consider first the



MONITOR KLYSTRON AND LOCAL OSCILLATOR A.F.C. SYSTEM

Figure 4.9

effect of the L.O.A.F.C. system. The overall frequency response of the I.F. amplifier has a rounded top, centred on 30 Mc/s, by virtue of its being synchronously tuned. Suppose the I.F. signal is not exactly tuned to 30 Mc/s, and lies somewhere on the side of the response curve; then any frequency modulation will be converted into amplitude modulation, and appear at the second detector. This applies to the 220 kc/s modulation, which is subsequently amplified and fed to a phase sensitive detector, whose output controls the d.c. reflector voltage on the L.O. klystron.

If the monitor klystron frequency is not exactly centred on the minimum of the cavity resonance dip, then the 140 kc/s frequency modulation of the monitor klystron will be converted into amplitude modulation, and appear at the second detector. This signal is amplified and fed to a phase sensitive detector operating at 140 kc/s, the output of which controls the d.c. voltage on the reflector of the monitor klystron. This servo-system is phased to seek a minimum in the response, whereas the L.O.A.F.C. is phased to seek a maximum.

It is to be noted that whereas the response curve governing the L.O.A.F.C. system consists only of the I.F. amplifier response, that governing the monitor A.F.C. consists of both the cavity dip and the I.F. amplifier response. This means that for correct operation of the monitor A.F.C., the intermediate frequency must lie exactly on the top of the I.F. amplifier response. For if it lay on one side, the monitor A.F.C. would seek the minimum of the combined I.F. amplifier and cavity response, which would in fact be on the side of the cavity dip, thus

leading to a dispersive component in the E.S.R. signal. This is one reason why the L.O.A.F.C. is desirable.

It was decided from the point of view of economy of circuitry to use a common amplifier, doubly tuned to 140 kc/s and 220 kc/s. The two oscillators are the two halves of a double triode. The apparent difference in basic design is accidental and immaterial. A signal of about ± 20 mV is fed to the monitor klystron, giving a deviation of ± 30 kc/s. The deviation of the L.O. klystron is about ± 100 kc/s, the greater figure being necessitated by the fact that the I.F. amplifier response is less sharp, and hence less sensitive to frequency modulation than the cavity dip. The range of control is about ± 15 volts on each reflector, and the overall loop gain several hundred in each system. The time constant is of the order of one second, so that the response time is a few milliseconds.

4.6 Pulsed Klystron (X.13) A.F.C. System.

The X.13 klystron, being pulsed, was not amenable to the type of A.F.C. system described in section 4.5, as such a system can only tolerate a limited amount of interruption (i.e. requires a duty cycle of nearly unity). It was decided to make use of the I.F. signal caused by the pulse. The system designed (Figure 4.10) employs a Round-Travis discriminator following the I.F. amplifier, in addition to the normal second detector. This discriminator is tuned to the intermediate frequency, 30 Mc/s, and gives no output from any signal at this frequency. If, however, the frequency of the I.F. pulse deviates from 30 Mc/s, a pulse of the

appropriate polarity appears at the discriminator. This pulse is amplified and passed to a polarity detector (EB91) producing a d.c. signal proportional to the error in frequency. This d.c. signal is amplified by an integrating amplifier (EF91) of fairly long time constant (about 15 sec.) and the output used to control the height of the pulses generated by the A2134 pentode. This valve is normally held cut off, but is driven fully conducting during the pulse period. Negative-going pulses of about 120 volts amplitude are produced and fed to the reflector of the X.13 klystron, so that the klystron operates around the centre of its mode during the pulse, and completely off the mode during the rest period. A pulse of amplitude 120 volts was found to satisfy these requirements adequately.

The operation of the system is almost independent of the klystron power level, since the I.F. amplifier is nearly always saturated by the pulse signal. Pulse powers from 25 microwatts to 250 milliwatts, the range normally used, are easily handled. It is also relatively independent of pulse width, by virtue of the polarity detector, which detects the peak pulse height, but is not greatly influenced by pulse width or duty cycle. The long integration time constant of the d.c. amplifier was chosen because it permits the use of greater loop gain for a given stability, and also smoothes out irregularities which might occur when using a low pulse repetition frequency (say down to one or two per sec.). The other two A.F.C. systems are unaffected, since their operation is only interrupted for the duration of the pulse, which is short (i.e. the effective duty cycle is very near unity). However, they must be in

operation before the pulse A.F.C. can operate. One of the principal reasons for applying A.F.C. to this klystron is that when operating at power levels of 100 mW or over, it is essential that the klystron remains tuned to the cavity resonant frequency, otherwise the power reflected from the cavity may be sufficient to damage the mixer crystal.

The pulse klystron A.F.C. system is also described by the author in Reference 36.

The monitor and L.O.A.F.C. systems are unaffected by the relative placing of the monitor and L.O. frequencies, but the pulse A.F.C. reverses the phase of its feedback according to whether the L.O. frequency is above or below the main frequency, so that only one of these placings is satisfactory.

4.7 Magnet and Field Sweep.

The magnet is a Newport 7-inch electromagnet powered by a Newport type B Mk. II supply fitted with a post-stabiliser. Fine control and slow sweep are effected by feeding in a small potential in series with the internally derived reference potential. A change of one ampere in magnet current is produced by a potential of 700 mV. The power supply had to be located at some distance from the apparatus because it radiates a considerable 50 c/s magnetic field and is somewhat noisy. Hence a remote control was desirable. The circuit adopted for this is shown in Figure 4.12 although various modifications of it have been used. Slow sweep is achieved using a Miller integrator with a large feedback capacitor. The 10 K Ω fine control is a ten turn helical potentiometer,

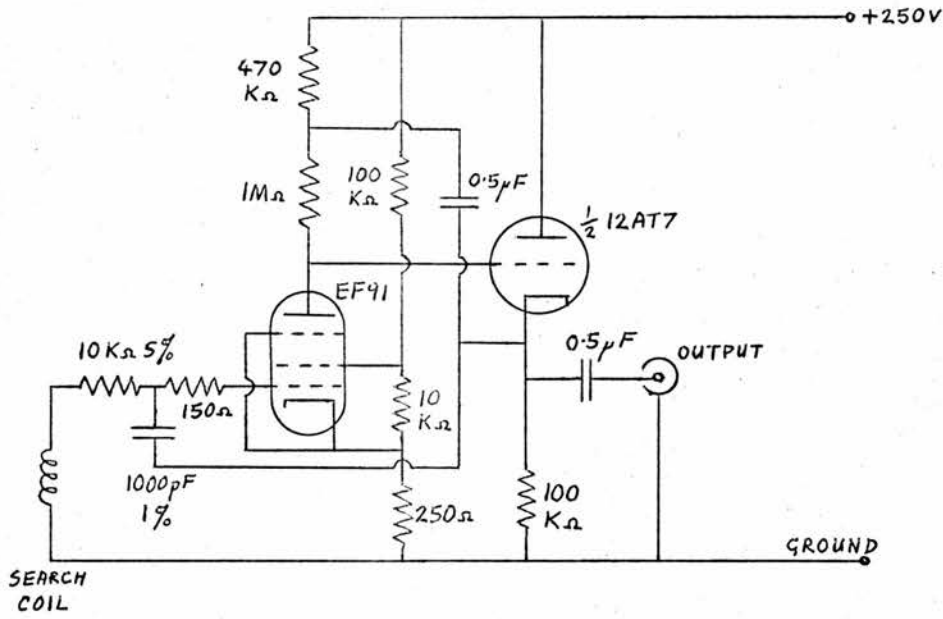
giving a control range of 2 amperes.

With a view to making the sweep more linear, a modification involving feedback from the auxiliary modulation coils on the magnet was tried. These coils were used as search coils, the idea being that if the sweep was linear, a constant potential would be induced across them. The system worked up to a point, but the loop gain obtainable was limited by the onset of oscillations, due to the considerable number of phase shifts and delays in the loop. Also, at very slow speeds, the induced potential was only of the order of a millivolt d.c., on top of which was nearly a volt of hum and other noise, making amplification and comparison rather difficult.

4.8 Field Modulation.

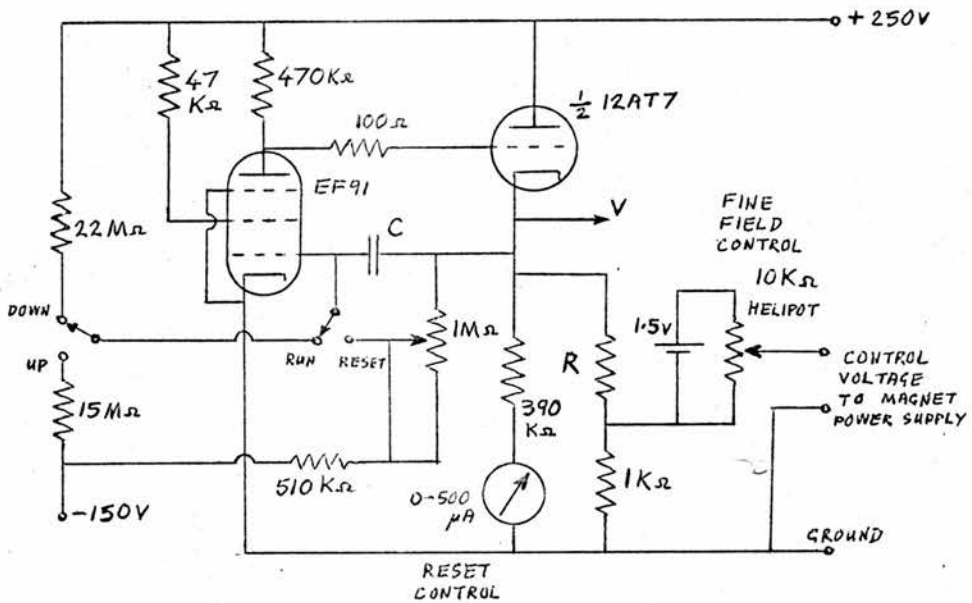
This is derived from an Advance H.1 signal generator, which is the basic timing unit in the apparatus. It covers the range 15 c/s to 50 kc/s, which is more than adequate, with sufficient accuracy (about 1% in the region normally used). It is set to give 10 volts r.m.s. to the reference input of the phase sensitive detector, and a variable signal to the field sweep amplifier, shown in Figure 4.13. This is basically a Williamson amplifier (Ref. 38) except that the feedback is current derived, in order that the field produced by the sweep coils may follow the input as closely as possible.

The sweep coils are mounted on the outer dewar of the cryostat, as shown in Figure 4.7 and are in the form of a distorted Helmholtz pair, each consisting of 75 turns of S.W.G. 34 enamelled copper wire, connected in series. They have a resistance of 20 ohms, an inductance of 8 mH and



INTEGRATING AMPLIFIER

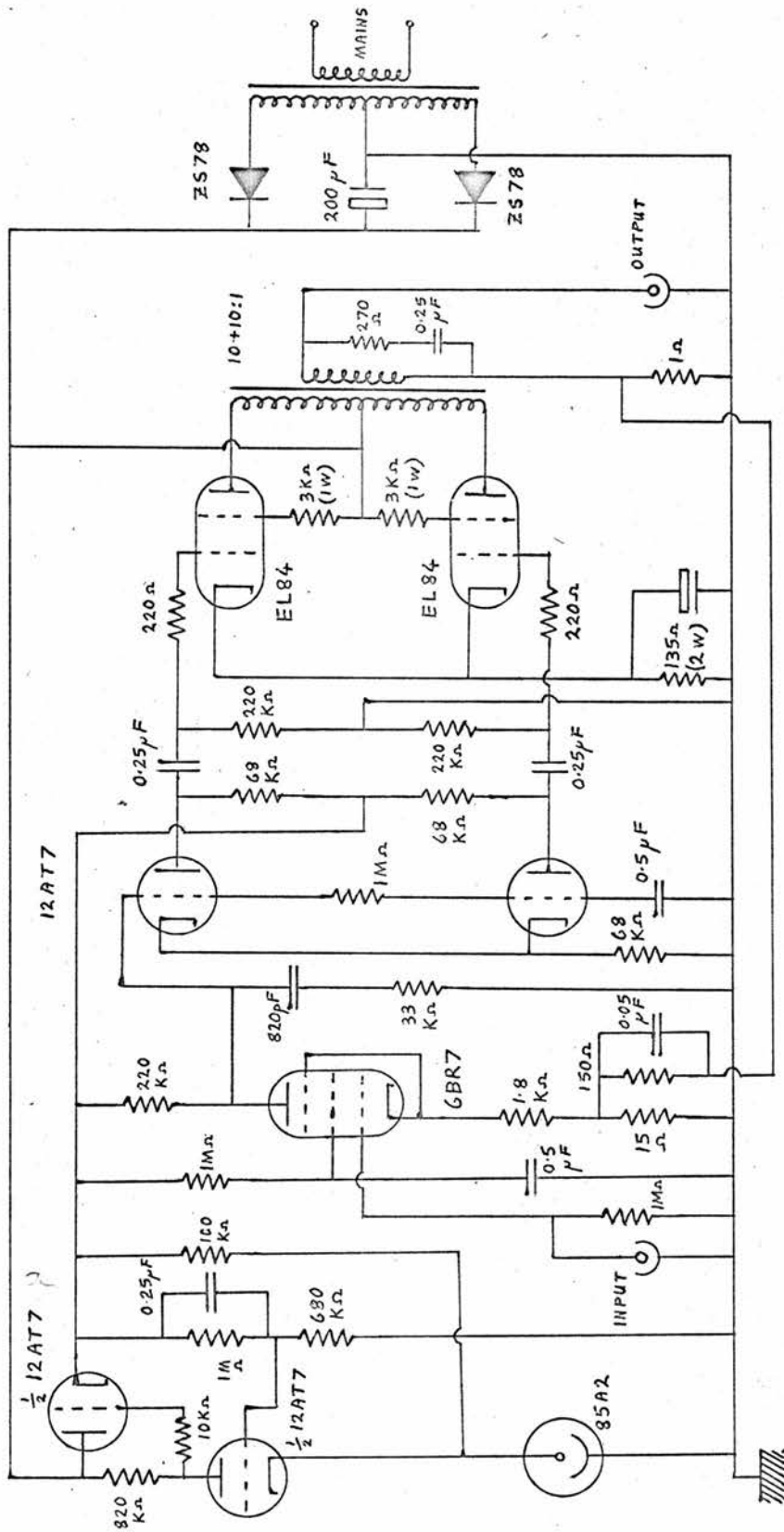
Figure 4.11



- R — SWITCHED 47K Ω , 100K Ω , 220K Ω , 470K Ω , 1M Ω , 2.2M Ω , ∞ .
- C — 18 μ F FOR SLOW SWEEP.
- $\frac{1}{2}$ OR 1 μ F FOR INTERMEDIATE SWEEP.

SLOW SWEEP CIRCUIT

Figure 4.12



FIELD SWEEP AMPLIFIER

Figure 4.13

produce a field of 40 gauss in the cavity for a current of one ampere. In conjunction with the power amplifier sweeps up to 80 gauss peak to peak are attainable at frequencies up to 400 c/s. Above this frequency, the maximum attainable sweep falls rapidly with increasing frequency, although the frequency response is fairly flat up to 2000 c/s. Without tuning, the maximum sweep rate is about 10^5 gauss per second. However, much greater rates can be obtained by tuning with a capacitor in series with the sweep coils. For example, a $0.25 \mu\text{F}$ capacitor tunes the system to 3600 c/s giving a maximum sweep rate of 6×10^5 gauss per second. This facility was made use of in the fast passage experiments described in Chapter 5.

A search coil of 200 cm^2 was mounted in one of the depressions on the side of the cavity, as close to the sample as was feasible. The output of this is amplified by the integrating amplifier shown in Figure 4.11 and presented on an oscilloscope for measurement, one volt corresponding to 5 gauss within the range of frequencies being used.

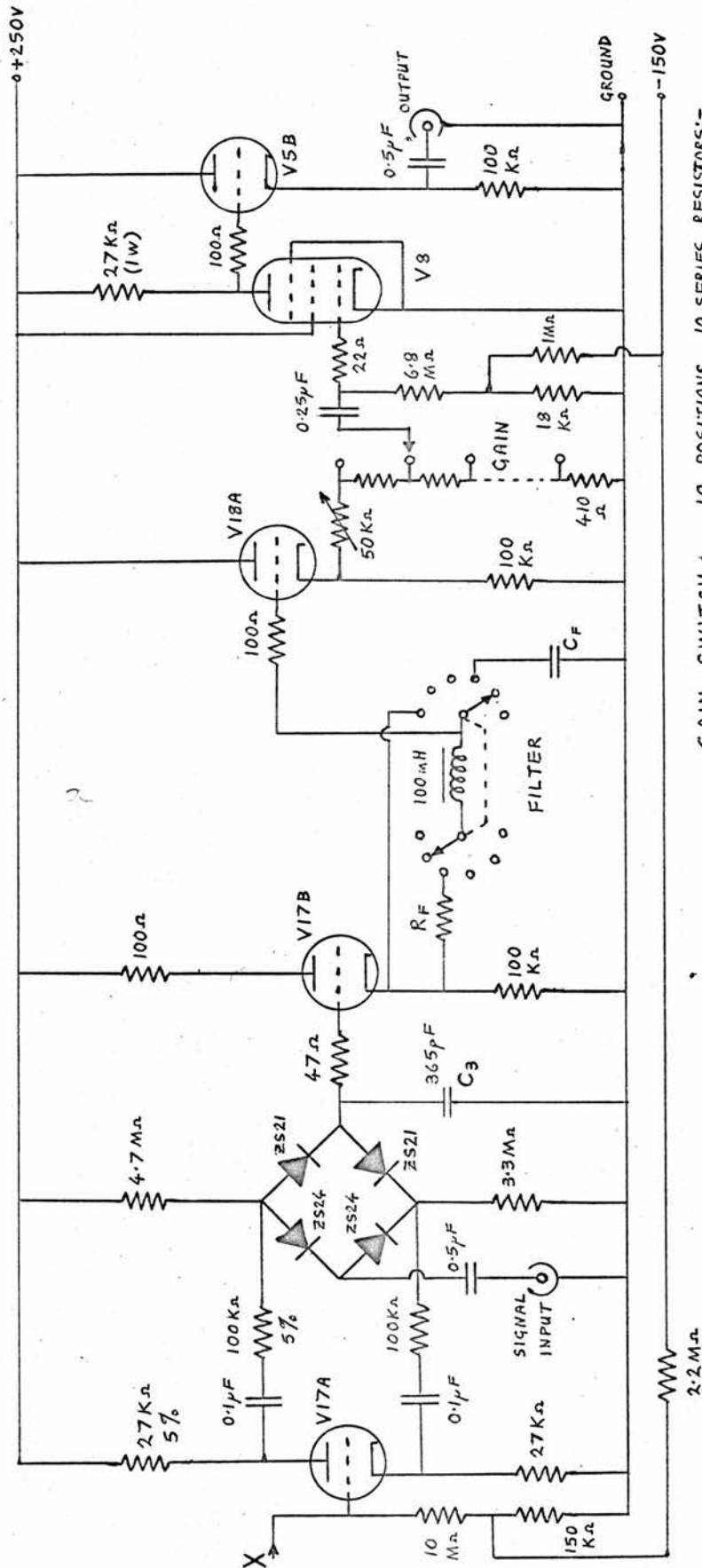
4.9 Pulse and Gate Circuits.

The pulse circuitry is shown in Figure 4.14. The field modulation waveform (obtained from the signal generator) is fed to a Schmitt trigger (V_1), designed to produce a trigger pulse at an appropriate point on each cycle, adjusted by VR_2 . The next stage (V_2) is an astable multivibrator, which determines the repetition frequency of the X.13 pulse, this being adjusted by the switched choice of C_1 and the fine control VR_3 . It is, however, always synchronised by the Schmitt trigger, so that

the pulse repetition frequency is an exact sub-multiple of the modulation frequency. The waveform from this stage is then differentiated, inverted (V_{15B}) and used to trigger a monostable multivibrator (V_3). This stage produces the actual X.13 pulse, the width being controlled by C_2 and VR_4 . The pulse is then fed to the pulse amplifier stage in Figure 4.10 and also to the gate circuit (Figure 4.15).

The gate consists of a four-diode bridge, the diodes of which are normally conducting, allowing the signal to pass freely. During the gating pulse (i.e. the X.13 pulse), they are driven into reverse bias by about 30 volts, so that no signal can pass, and the output potential remains at the value existing immediately before the gating pulse, being stored by C_3 . The diodes are fast switching silicon types (Ferranti ZS21) with a low charge storage to prevent breakthrough of the gating pulse into the following circuit. Even so, the breakthrough was reduced further by making use of stray capacities (i.e. adjusting the layout of connecting wires). The residual pulse is only of the order of millivolts. The cathode follower V_{17B} presents an infinite impedance to the gate, as required if the potential on C_3 is to remain fixed during the gating period, and a low output impedance to match the filter. A single stage LCR low-pass filter was found to be adequate, and is used mainly to eliminate signals due to the A.F.C. systems. Finally the signal is amplified (V_8, V_{5B}).

The low-frequency response of the signal path in this system extends well below $1c/s$. This is to preserve overall waveform shape. The system could not be direct coupled, because the d.c. signal level from the



GAIN SWITCH: 10 POSITIONS, 10 SERIES RESISTORS:-
 33K Ω , 18K Ω , 10K Ω , 5.6K Ω , 3.3K Ω , 1.8K Ω , 1K Ω , 560 Ω , 390 Ω , 4.0 Ω .

VALVES: V5, V17, V18 - 12AT7
 V8 - EF91

GATE AND FILTER

POS.	R _F (K Ω)	C _F (PF)	CUT-OFF FREQ (Kc/s)
1	1.5	50,000	1.5
2	5.8	5,000	5
3	13.3	1,000	11
4	28.5	200	25
5	55.5	50	50
6	∞	—	FLAT

FILTER SWITCH

Figure 4.15

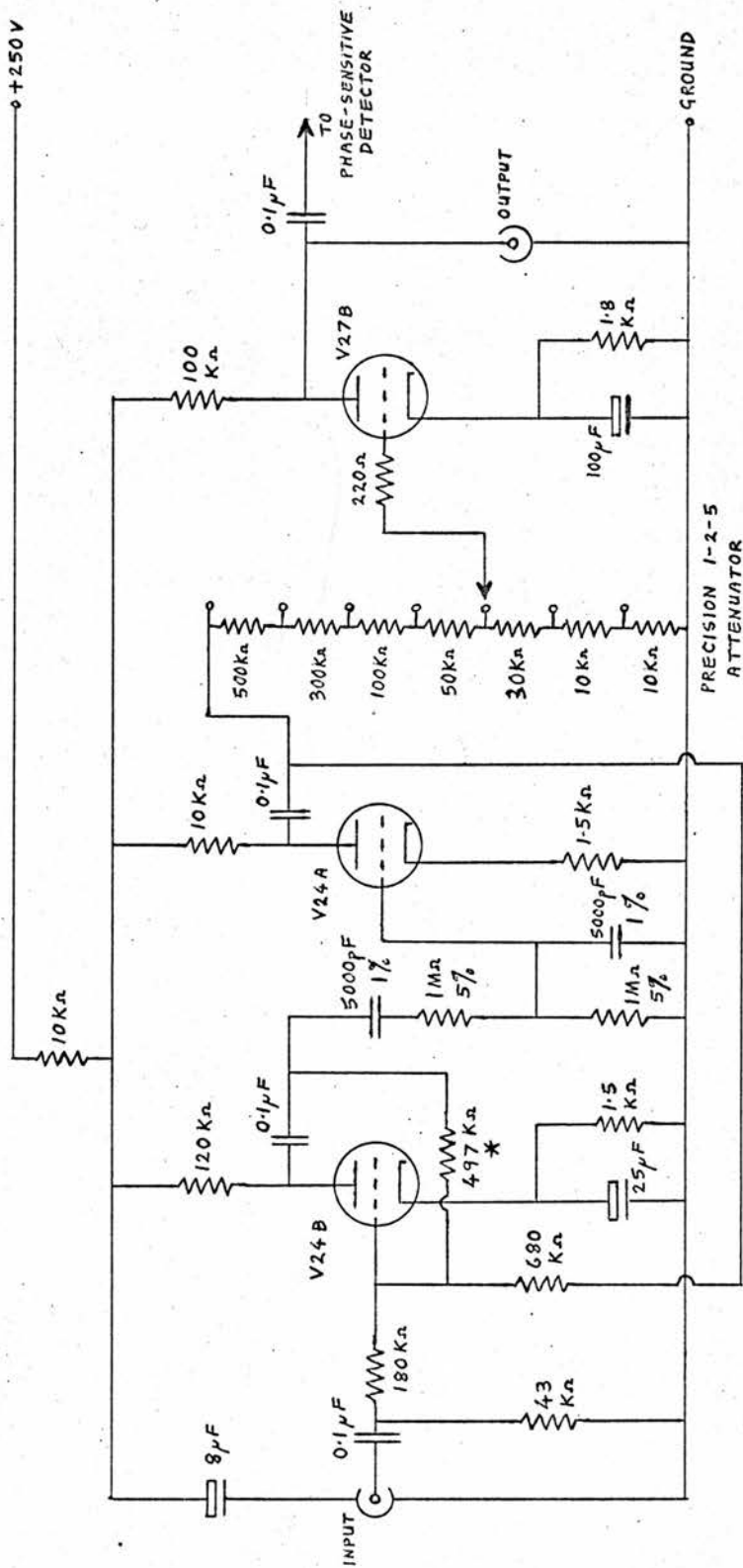
second detector changes with liquid helium level, cavity coupling and other factors. The essential point is to minimise phase distortion of the lowest frequency components in the signal waveform.

4.10 The Apparatus as a Derivative-recording Spectrometer.

For this the apparatus is set up as shown in Figure 4.3. The narrow-band amplifier (Figure 4.16) is based on the Wien Bridge, and has the advantage that it gives zero phase shift at resonance, unlike the more common twin-T system which gives 45 degrees phase shift. The amplifier resonates at 320 c/s ($\omega = 2000 \text{ sec.}^{-1}$) and has a bandwidth of ± 20 c/s ($Q=8$), adjusted empirically by R^* . A narrower bandwidth is not required, and only leads to instability of gain. A precision step attenuator was also incorporated to facilitate quantitative measurements.

The phase-sensitive detector (Figure 4.17) is based on Schuster's circuit (Ref. 37). A reference signal 10 volts r.m.s. at 320 c/s is derived from the signal generator, which also drives the field sweep amplifier. A choice of integration time constants from 0.2 to 5 seconds is provided, and the output may be either balanced, to feed the pen-recorder (Honeywell, ± 50 mV F.S.D.) or unbalanced (± 1 volt output) for use with the Digital Memory Oscilloscope (see section 4.11). For the intermediate passage experiments of section 7.6, a special two-stage RC filter having an approximate time constant of .04 seconds was used, the two stages being required to eliminate 320 c/s breakthrough while giving as short a time constant as possible.

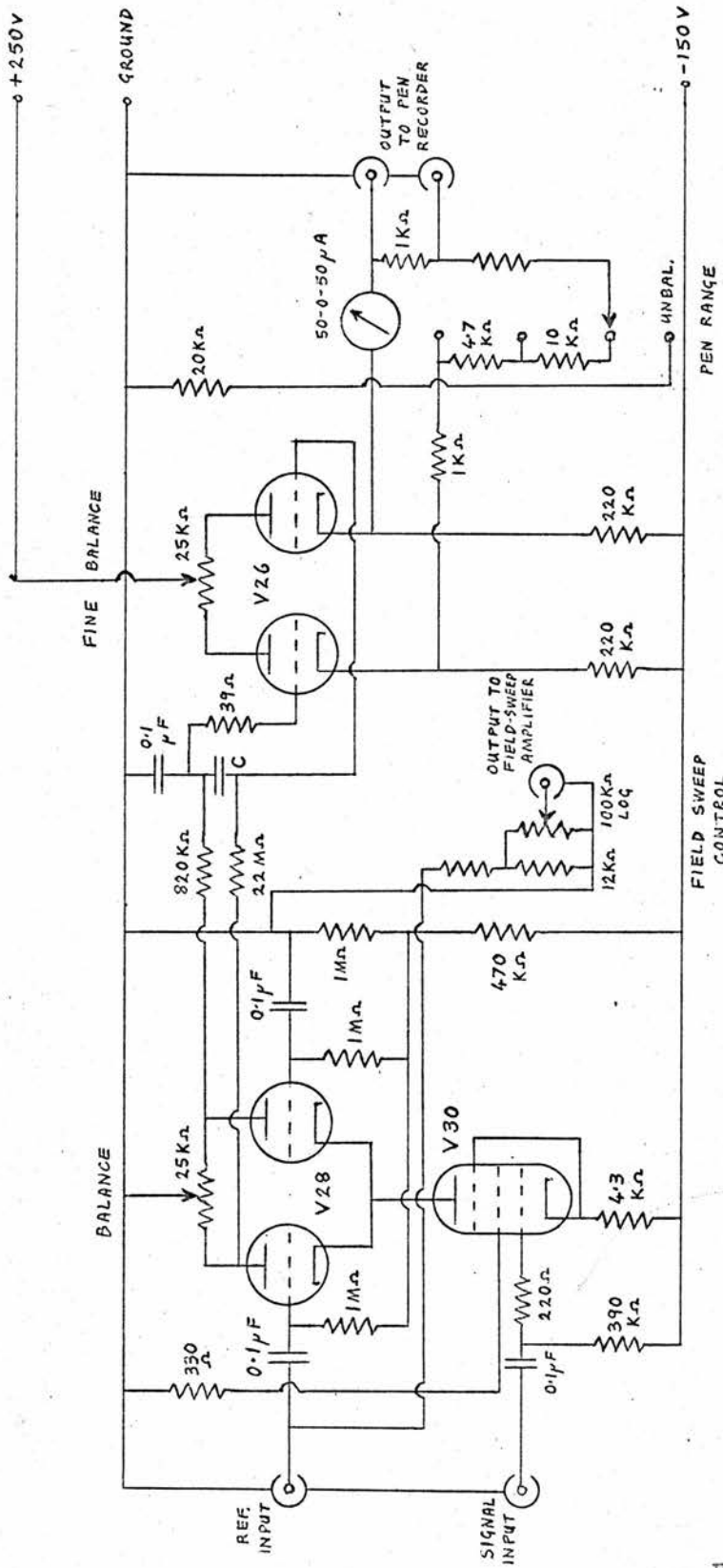
The spectrometer was standardised using a 5 mg sample of $\text{CuSO}_4 \cdot 5\text{H}_2\text{O}$,



* SEE TEXT

NARROW BAND AMPLIFIER

Figure 4.16



- V26 - 12AT7
- V28 - 12AT7
- V30 - 6AV6

C - SWITCHED 0.01, 0.05, 0.1 OR 0.25 μF
 TO GIVE 0.2, 1, 2 OR 5 SECONDS TIME CONSTANT

PHASE SENSITIVE DETECTOR

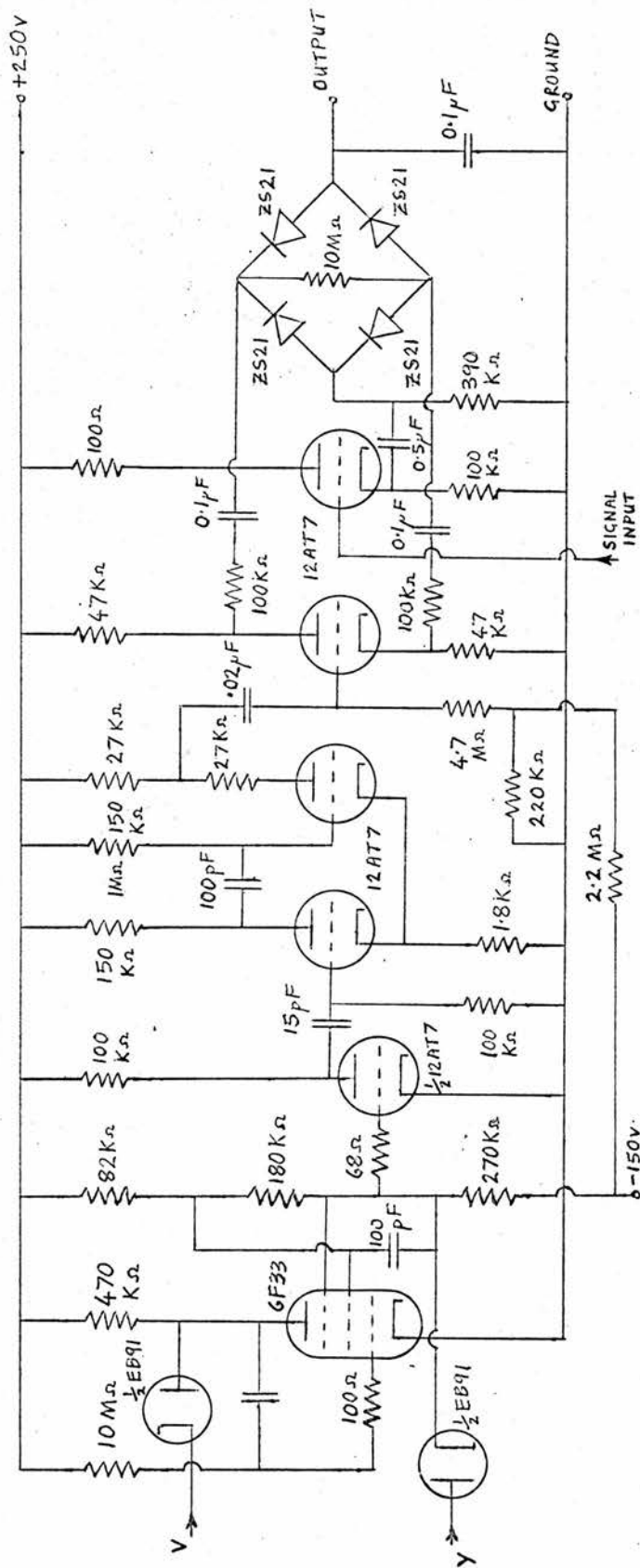
Figure 4.17

which contains 1.2×10^{19} spins. This gave rise to a line whose first moment was 6.1×10^5 units gauss² with a modulation of 2 gauss peak to peak (unit modulation). One unit of signal is that giving rise to 1 mV of pen-recorder signal at the lowest gain setting. The noise level is about .03 units peak to peak at 1 second time constant, indicating that the minimum detectable number of spins is about 10^{13} per gauss at room temperature.

4.11 Display and Recording.

Initially, the signal was displayed directly on an oscilloscope and photographed, but this method was found to be insufficiently sensitive for weaker samples and generally insufficiently accurate. However, it is still useful to make measurements directly on the oscilloscope screen, as in section 5.4, for example.

A sampling system was devised whereby a repetitive waveform lasting a few milliseconds could be converted into one lasting a few minutes, suitable for pen-recording, and which afforded a certain amount of noise reduction (e.g. Refs. 39, 40, 41). A 50 microsecond sample was taken each pulse cycle at a time t after the X.13 pulse, the interval t varying with real time T such that dt/dT was a constant, of the order of 10^{-4} to 10^{-5} . This sample was stored as a potential on a capacitor until the next sampling pulse. The circuit is shown in Figure 4.18. Noise was reduced by a factor of about ten, and 50 c/s hum on the signal eliminated, provided that the pulse repetition frequency was not harmonically related to the mains.



SAMPLING CIRCUIT

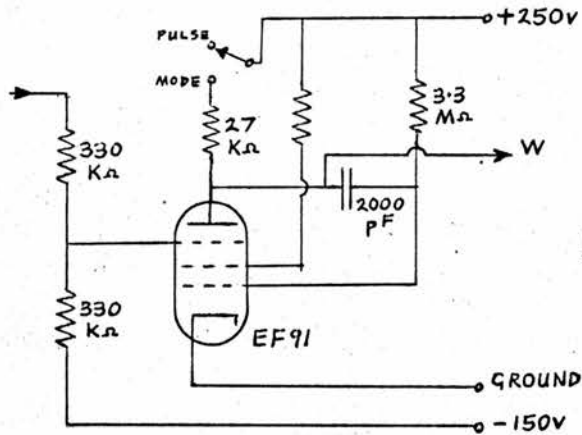
Figure 4.18

4.12 Setting-up Procedure.

Initially the apparatus is set up using a saw-tooth sweep of the X.13 klystron mode. This sweep is derived from the astable multivibrator, V_2 , in the pulse circuit (Figure 4.14), and is shown in Figure 4.19. The X.13 power is attenuated to about 1 mW, and the mode, as reflected from the cavity, is observed at the crystal current meter socket on the I.F. amplifier (see section 4.4). The cavity resonance dip is easily found by tuning the X.13 klystron manually. The microwave frequency can then be determined from the wavemeter (a Phillips direct-reading absorption wavemeter in series with the cavity arm, Figure 4.2) which causes a shallower, narrower dip, since it has a higher Q than the cavity.

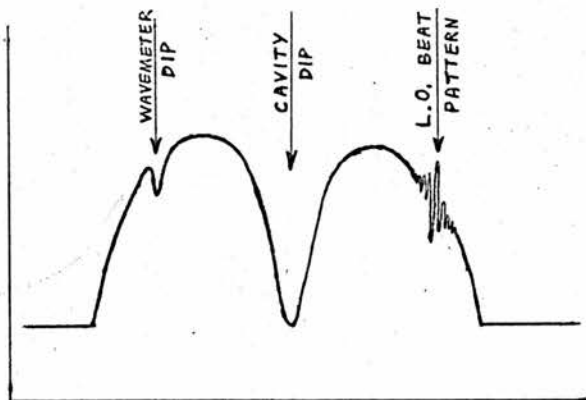
Next, the local oscillator klystron is tuned until a beat pattern appears on the mode, as illustrated in the sketch of Figure 4.20. It is then set about 30 Mc/s to the right of the cavity dip, using the wavemeter as a guide. The monitor klystron is then tuned in and set exactly on the dip; it produces a beat pattern similar to the local oscillator, but much smaller.

The X.13 klystron is then switched to pulse operation, using a narrow pulse. A signal should be appearing at the second detector. The local oscillator is tuned to maximise the second detector current, after which the L.O.A.F.C. is switched on. The cavity is then manually fine-tuned by means of the quartz rod to give a minimum second detector current, though not zero. If the second detector current is too low, indicating



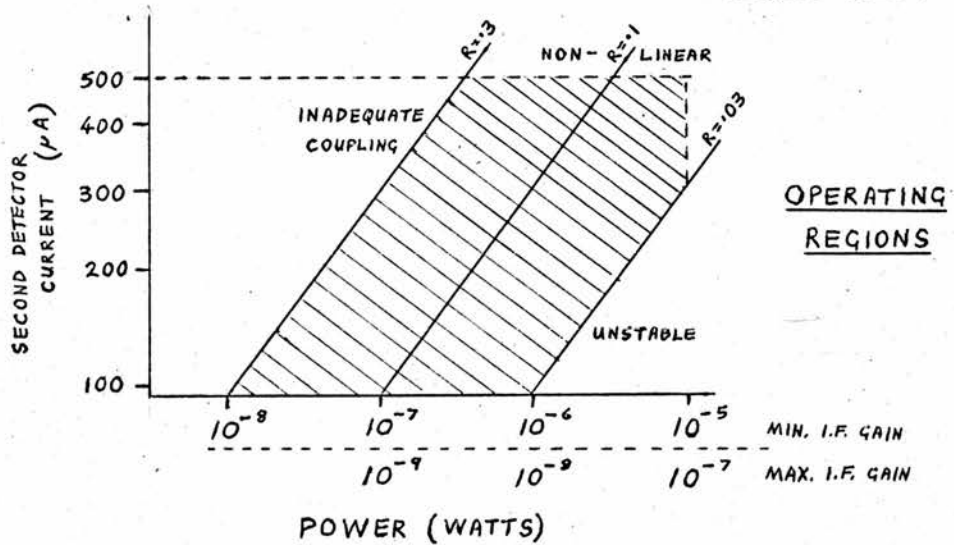
MODE SWEEP
CIRCUIT

Figure 4.19



TYPICAL
MODE
DISPLAY

Figure 4.20



OPERATING
REGIONS

Figure 4.21

With the monitor and L.O.A.F.C. systems on (tuned to the cavity), the second detector current is maximised by manually tuning the monitor klystron, while at the same time keeping the monitor A.F.C. meter at or near zero by means of the reflector voltage control.

The X.13 klystron is optimised by viewing the mode with the sawtooth sweep, adjusting the sliding-stub tuner for maximum output, and finally manually tuning the X.13 klystron to bring the cavity dip to the centre of the mode. This may be done before or after the other klystrons are set up. If it is done afterwards, the procedure will probably have disrupted the A.F.C.'s. All that is required, however, is to switch off all the A.F.C.'s, switch the X.13 to "pulse", switch on the L.O.A.F.C., then the monitor A.F.C., then adjust the X.13 reflector voltage as before until the X.13.A.F.C. meter is hovering between its two extremes, then switch on the X.13.A.F.C. The spectrometer is now fully optimised.

With the monitor klystron at full power (10 microwatts) the optimum cavity coupling is given by a second detector current of 300 to 400 microamperes (3 to 4 volts output) at minimum I.F. amplifier gain. Below 250 microamperes, the monitor A.F.C. becomes unstable, due to excessive loop gain, and above 400 microamperes, the second detector tends to become non-linear. This setting corresponds to a cavity reflection coefficient of .03 (V.S.W.R.=1.06). Down to a monitor power level of 10^{-7} watts, no increase in I.F. amplifier gain is required; the second detector current is kept above 100 microamperes by varying the coupling. Below 10^{-7} watts, the I.F. amplifier gain is increased in proportion to the attenuation of monitor power, down to the minimum usable power

of 10^{-9} watts, where full I.F. amplifier gain is required. These various operating regions are shown graphically in Figure 4.21.

4.14 Operation.

When the cryostat is filled with liquid helium, the cavity resonant frequency falls by about 200 Mc/s, since the dielectric constant of helium is 1.048. With this in mind, it is customary to tune the klystrons to the expected frequency before filling, to save time. A frequency of 9300 Mc/s is normally found to be satisfactory, although in the case of the large silicon sample used in the experiments of Chapter 6, 9200 Mc/s was used. The cavity resonant frequency varies slightly with temperature down to the λ -point of helium, but is easily re-tuned using the quartz rod. Below this temperature, the frequency is remarkably stable.

Since the helium is allowed into the waveguide, there is a top surface of helium in the guide, leading to a reflection coefficient of about .024. This is of the same order as that from the cavity (.03) and means that the coupling must be adjusted quite often as the helium level falls, since the two reflections interfere with a varying phase difference. The coupling can be altered during the course of a recording without producing unwanted signals, but it must be done carefully, and is to be avoided if possible.

When the X.13 klystron is delivering full power (250 mW) to the cavity, the reflection coefficient must be low. If a limit of 2.5 mW is placed on the pulse power arriving at the mixer crystal, the reflection coefficient must not exceed 0.1.

In the above discussion, the microwave power by-passing the ferrite circulator has been neglected. It is less than 1% of the total, and is automatically compensated for in the coupling adjustment. Provided that the cavity arm is not too long, the amount of dispersion signal introduced due to this leakage is negligible. In most of the experiments, no trouble was experienced with unwanted dispersive components, although the observations of section 7.6 could be explained by incomplete suppression of the dispersion signal which, at such a high level of saturation, greatly outweighs the absorption. The monitor and L.O.A.F.C. systems were specifically designed with the intention of removing dispersive components from the signal.

4.15 Limitations of the Apparatus.

Since the apparatus is intended for the investigation and measurement of passage effects, it is desirable to know its limitations in this respect. For measurements of inversion efficiency, the E.S.R. line must be narrow enough that it can be swept through completely over a wide range of sweep rates. Inverting passage is normally carried out by timing the X.13 pulse to occur over one complete half cycle of the modulation, from peak to peak as illustrated in the top drawing of Figure 5.2, with the line in the middle of the modulation range. Since the sweep must be reasonably linear in the vicinity of the line to approximate to the conditions of Chapter 2, a lower limit of about five times the line width must be set on the usable modulation depth; the sweep is part of a sine wave and therefore not strictly linear. The

lowest modulation frequency which can be used is set by the spin-lattice relaxation of the line, T_1 . If too much relaxation takes place within half a cycle of the modulation, the allowance made for T_1 in extrapolating back to the time of passage (see section 5.4) will be too large and subject to error. With this in mind, T_1 should be at least three times the modulation period. As an example, a line of width 1 gauss and $T_1 = 5$ milliseconds would set a lower limit on the modulation of 5 gauss peak to peak, and 600 c/s; i.e. the minimum usable sweep rate would be 10^4 gauss / second.

At the other extreme, the maximum sweep rate which can be used is limited by the field sweep amplifier. As pointed out in section 4.8, this can be increased by tuning, and sweep rates up to 6×10^5 gauss / second have been achieved and used. However, another complication arises at such high sweep rates; the signal bandwidth required becomes very large. Now the bandwidth is necessarily limited to 50 kc/s to eliminate signals due to the A.F.C. systems, so that in the case of the above sweep rate on a line of width 1 gauss, a considerable attenuation and broadening of the line signal would result. This does not materially affect the measurements, since the amplitude of the signal on each half cycle is still proportional to the magnetisation, but it does result in a loss of sensitivity (i.e. an increase in noise). From the sensitivity measurements of section 4.10, it can be deduced that for a signal bandwidth of 50 kc/s, the minimum detectable number of spins at 4.2° K should be 7×10^{13} per gauss. A useful signal would be at least ten

times noise level and this, combined with the necessity of a considerably reduced monitor klystron power to avoid any saturation of the spins during observation (10^{-7} watts or less) leads to a lower limit of about 2×10^{16} spins per gauss.

Due to the fact that the amplifying chain following the second detector is not direct coupled, there is a limit to the low-frequency response of the system, and this leads to an upper limit of about 20 milliseconds for the relaxation time which can be conveniently handled or measured. In trying to measure times greater than this, errors are introduced due to "sagging" of the waveform. This limitation is encountered in section 7.8.

As a derivative-recording spectrometer, the following limitations may be noted:

- 1) Microphonic pickup from the modulation coils becomes noticeable at modulation depths exceeding 5 gauss peak to peak. It gives rise to spurious drifts in the recorded trace.

- 2) The maximum monitor klystron power is only 10^{-5} watts, which restricts the use of the apparatus as a general purpose spectrometer. It is, however, adequate for the use intended.

CHAPTER 5

EXPERIMENTS ON NEUTRON-IRRADIATED MAGNESIUM OXIDE.5.1 Nature of Spectrum.

Neutron-irradiated magnesium oxide has already been studied with regard to its E.S.R. properties (Refs.43, 44) and as a potential two-level maser material (Refs.10, 11). The spectrum consists of a single intense narrow line (width about 0.7 gauss at liquid helium temperatures) at $g = 2$ and some associated hyperfine structure. The line is interpreted (Ref.44) as arising from F-centres induced in the material by neutron bombardment. Those F-centres having only Mg^{24} and Mg^{26} neighbours give rise to the single line, while those with one and two Mg^{25} neighbours (nuclear spin $5/2$) give hyperfine patterns of six and eleven lines respectively. This hyperfine pattern is not very well resolved, and appears as a complicated structure around the base of the main line.

The spin-lattice relaxation time is of the order of 5 to 10 milliseconds (section 5.3) and this, combined with the narrow intense line makes this a suitable material for the study of inversion efficiency, in view of the discussion of section 4.15.

5.2 Samples.

The neutron-irradiated MgO samples used by Campbell and Firth (Refs.10, 11), as listed in Table 2, were used. Samples 2 and 3 were found to be too strong for the spectrometer, in that they gave rise to instability of the A.F.C. systems. This is most probably due to the fact

TABLE 2.

Neutron-irradiated MgO Samples.

Sample	Weight (gms.)	Dimensions (mm)	Estimated Spin Density (cm^{-3})	Total Spins	Dosage (1 MeV neutrons)
2	0.75	12.7x2x9.3	5.2×10^{18}	1.1×10^{18}	2.4×10^{18}
3	0.75	12.7x2x9.3	5.2×10^{18}	1.1×10^{18}	2.4×10^{18}
7	0.30	11 x 2 x 4	6.0×10^{17}	5×10^{16}	?
2(b)	0.133	2 x 2 x 7.5	5.2×10^{18}	1.9×10^{17}	-

that the resonance signal is so large that it distorts the cavity resonance dip to such an extent that two minima are produced, and the monitor klystron A.F.C. cannot decide which of these to seek. In any case, the signal was too large for the second detector to handle in a linear manner. It was therefore decided to cut a small slice from sample 2 to form sample 2(b).

Samples 2 and 3 were irradiated at Harwell in 1959, and are a distinct blue colour. Sample 7 was irradiated at Dounreay in 1961, but its dosage is unknown. Although quoted by Firth (Ref.11) as being light blue, it no longer has any trace of blue coloration, and is in fact somewhat yellowish, suggesting either deterioration or subsequent heat treatment. Also, the main line in sample 7 is much broader than in samples 2 and 3

at room temperature.

These samples also exhibit a spectrum of six equally spaced isotropic narrow lines, whose intensity is independent of neutron dosage (in sample 7, these lines are almost as intense as the main one). Comparison with the work of Wertz et al. (Refs. 45, 46) has shown that these lines are caused by the impurity Mn^{++} , whose nuclear spin $5/2$ gives rise to a hyperfine sextet with a splitting parameter of $.00814 \text{ cm}^{-1}$; this agrees with the observed splitting of 83 gauss $\pm 10\%$ between adjacent lines. Each of these six is further split into a pentad of lines by the cubic crystalline field, due to the fact that it is the ${}^6S_{5/2}$ state of Mn^{++} which is being observed. ($I = 5/2$ and $S = 5/2$, giving 36 levels; subject to the rule $\Delta m_I = 0$; $\Delta m_S = \pm 1$, there are 30 transitions, in 6 groups of 5). An experiment involving three consecutive levels of this system is described in section 5.6.

5.3 Measurements of Spin-lattice Relaxation Time.

Two different techniques for measuring the spin-lattice relaxation time, T_1 , both using saturation-recovery, were compared.

a) The magnetic field is modulated at some frequency f_m such that $f_m T_1 > 1$, and a microwave saturating pulse applied over half a cycle of the modulation, and the recovery of the line is observed by noting the size of the signal on successive half cycles. The modulation is such as to sweep through the line completely each half cycle.

b) The magnetic field is held constant at the resonance value and only the saturating pulse applied. The signal recovery is then monitored

continuously.

The Digital Memory Oscilloscope was used in conjunction with both these techniques. The results of these experiments are shown in Figure 5.1 (a) and (b), as graphs of the relaxation time T_1 against temperature. In method (a), T_1 was calculated by plotting S_N against S_{N+2} , where S_N is the amplitude of the signal on the Nth half cycle after the saturating pulse, and taking the gradient of the best straight line through these points. The relaxation rate is then

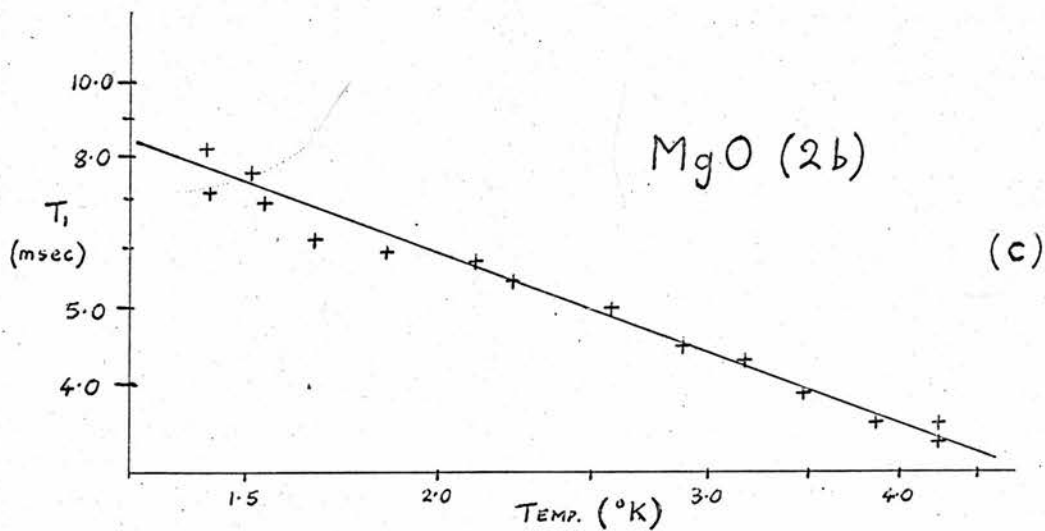
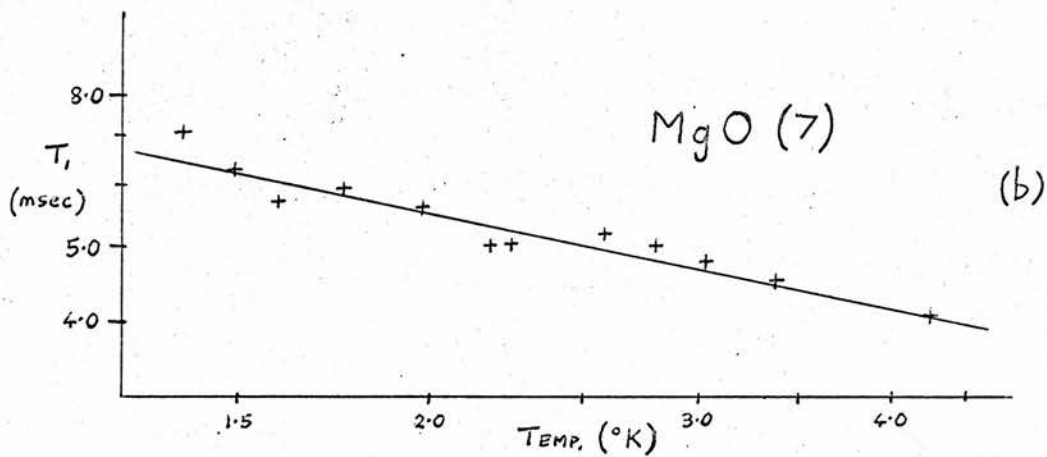
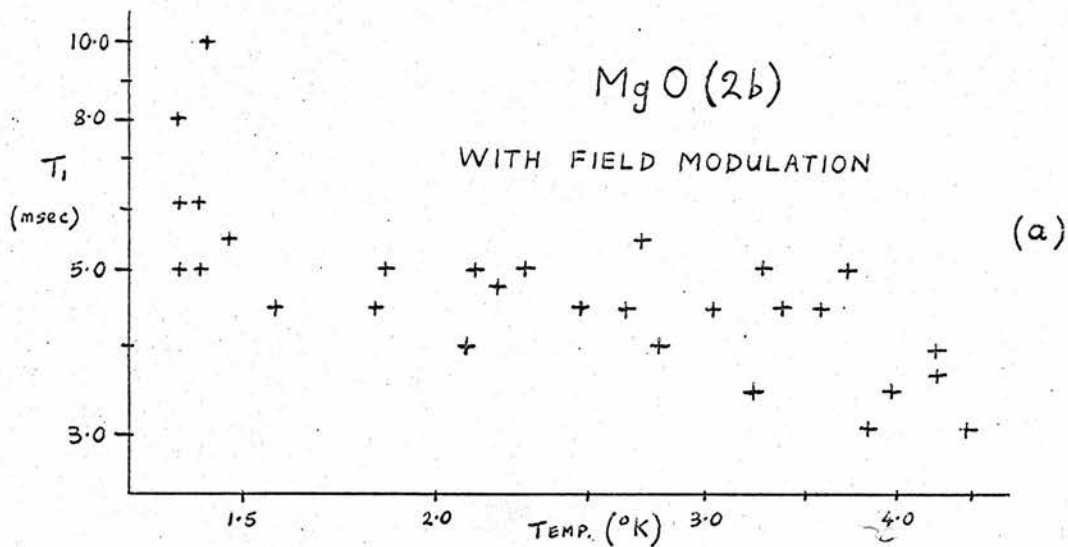
$$T_1^{-1} = f_m \log_e (\text{gradient}) \quad (5.1)$$

A similar process is used in method (b), except that points are taken on the relaxation curve at intervals of ΔT , giving

$$T_1^{-1} = \log_e (\text{gradient}) / 2\Delta T$$

Both methods assume, of course, that the relaxation can be represented by a single exponential decay of time constant T_1 . If the relaxation is a mixture of decay times, the longest of these can theoretically be isolated by neglecting the initial part of the decay. This has been done using the IBM 1620 to compute a best fit straight line, starting off by taking all the points, and successively neglecting one, two, three initial points, and so on. If too much of the initial decay is neglected, the fitting error will increase because the signal in the tail of the decay is small. In general, the smallest fitting error was obtained by neglecting two initial points.

Method (a) gives a larger estimated error in each value of T_1 and a



TEMPERATURE DEPENDENCE OF T_1 IN MgO

Figure 5.1

considerably larger spread of points on the graph of T_1 against temperature than method (b). It appears that a great deal of this extra error arises from the operation of the Digital Memory Oscilloscope, not due to any inherent inaccuracy, but rather to the fact that the signal is digitised in time. Whether the peak of the line signal during each half cycle occurs at a sampling time or between two sampling times makes a considerable difference to the value ascribed to that peak, whereas in the smooth curve generated in method (b) no such considerations apply. This type of error is characteristic of digitising systems. The situation might be improved if the sampling frequency could in some way be locked to the field modulation frequency, but this does not seem to be feasible in the Digital Memory Oscilloscope. It is, however, necessary to use method (a) when dealing with inhomogeneously broadened lines, as will be discussed in Chapter 7.

The results presented in Figure 5.1 (b) were taken using a monitor klystron power level of -20 dB (i.e. about 10^{-7} watts). At 4.2° K, the relaxation rate rises from 280 sec.^{-1} to 360 sec.^{-1} for sample 2(b) when the incident power is increased to 10^{-5} watts. From this it is estimated that the error in using a power of 10^{-7} watts is of the order of 1 sec.^{-1} , i.e. insignificant. The experimental points fit a curve of the form

$$T_1^{-1} \propto T^{.74} \quad \text{for sample 2(b), and}$$

$$T_1^{-1} \propto T^{.42} \quad \text{for sample 7 (Figure 5.1(c))}$$

This deviation from the expected $T^{1.0}$ law is in agreement with the

observations of Firth (Ref. 11) for sample 2(b) but not for sample 7, where much less temperature dependence is found. The temperature, T , of the sample was deduced from the helium vapour pressure (Ref. 47). It is quite probable that much of the discrepancy is due to the fact that what is being measured is partly an initial, faster relaxation, and that the true T_1 process only appears in the tail of the curve, where errors of measurement are much greater due to the smaller signal. The true T_1 may well be considerably greater than that observed. This mixture of relaxation times is consistent with the idea of a hybrid line, as suggested in section 8.3.

5.4 Inversion Measurements - Extended Pulse Technique.

In view of the fact that a wide range of modulation depths would be used in inversion measurements, it was decided that some technique should be devised in which the existence of an absolute base line, that is, a signal level corresponding to zero absorption, is not a prerequisite of any observation. This is especially important in a multi-line system where the zero-absorption base line may only be evident in some parts of the spectrum. In MgO in particular, each important line is surrounded by a complicated structure of less significant and unwanted lines. These only amount to a fraction of the wanted signal, but are sufficient to distort the apparent base line, especially if a small field modulation is being used.

Since the line can only be observed a finite time after passage, a correction must be made for the spin-lattice relaxation occurring between

passage and observation. This is incorporated in the technique which is described below.

The difference in amplitude between the signal during the Nth half cycle after the inverting pulse and the amplitude of the signal immediately before the pulse is called Y_N . The time interval between pulses is such that the system has more or less fully relaxed before each inverting pulse (i.e. $\geq 3T_1$). A relation of the form

$$Y_N / Y_{N+1} = \lambda = \exp(1 / 2 f_m T_1) \quad (5.2)$$

should hold. The quantity Y_N is related to the relative magnetisation Z_N by

$$Y_N = k (1 - Z_N) \quad (5.3)$$

where k is a constant depending on the line intensity and the overall sensitivity of the apparatus. $Z = 1$ represents a fully relaxed line.

After this measurement of Y_N is taken, the X.13 pulse is extended to cover a complete cycle of the modulation as shown in Figure 5.2, so that the line is re-inverted on the second passage. Suppose that the magnetisation relative to the thermal equilibrium value after the first passage is Z_f (see section 2.6); this will relax to Z_i' immediately before the second passage, where

$$(1 - Z_f) / (1 - Z_i') = \lambda$$

After the second passage the magnetisation will be

$$Z_i' = Z_i' Z_f = Z_f [1 - \lambda(1 - Z_f)] \quad (5.4)$$

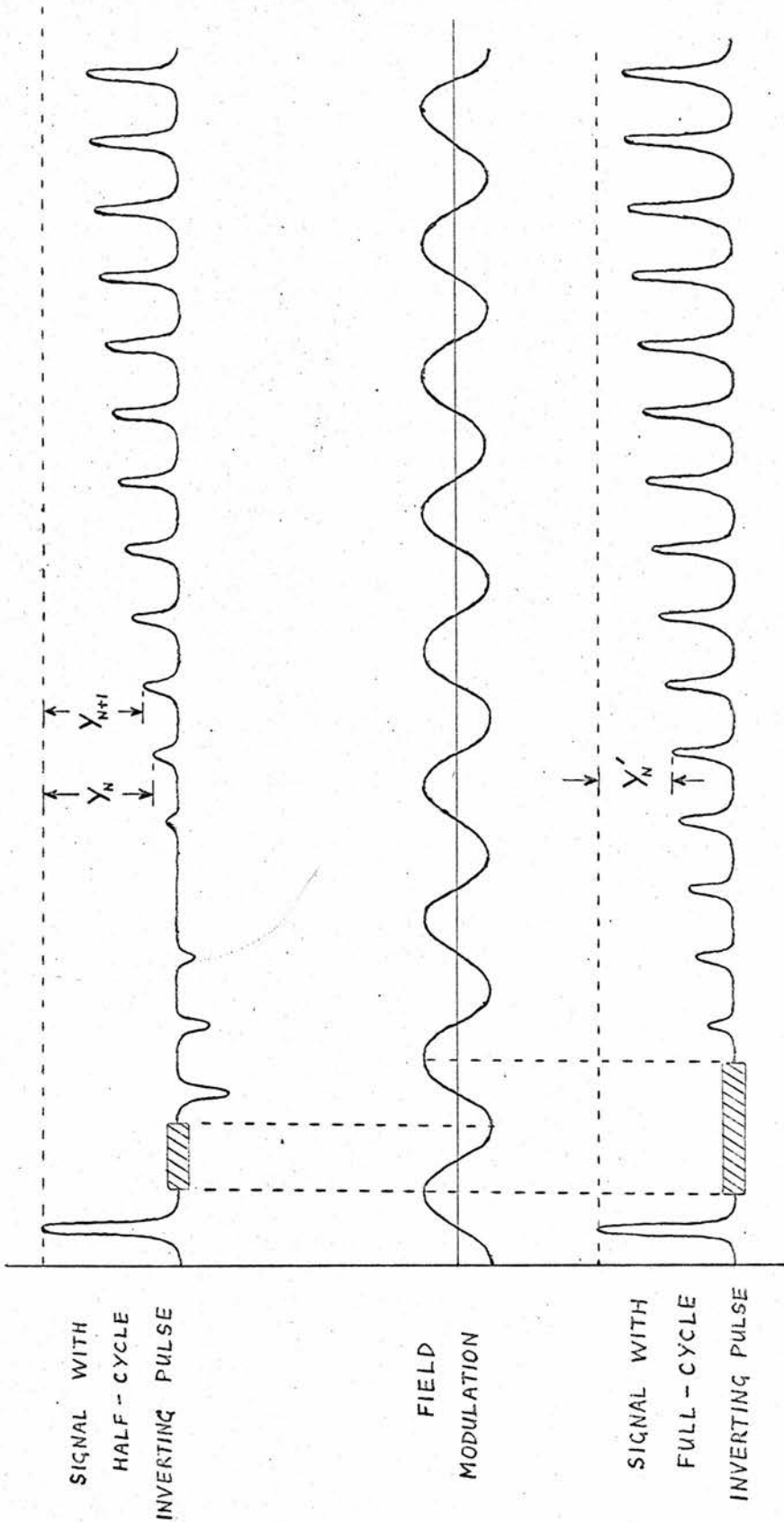


DIAGRAM ILLUSTRATING EXTENDED-PULSE TECHNIQUE

Figure 5.2

as compared with the value on the first half cycle after the pulse in the half-cycle pulse case

$$z_1 = 1 - \lambda(1 - z_f) \quad (5.5)$$

From equations 5.3, 5.4 and 5.5,

$$z_f = (Y'_N / Y_N) - \lambda \quad (5.6)$$

where Y'_N is the difference in amplitude between the signal during the Nth half cycle after the first passage in the double passage case, and the signal immediately preceding the pulse. The technique is illustrated in Figure 5.2.

Measurements were made directly on the oscilloscope screen (a Solartron CD 1014). This was sufficiently stable and noise-free. Use of the Digital Memory Oscilloscope was avoided for the reasons given in section 5.3. The noise on the signal was averaged out by eye, since it was only of the order of a millimetre in several centimetres of signal.

5.5 Inversion Measurements - Results.

The results of measurements on the main line in sample 2(b) are shown as a contour map of Z_f against pulse klystron power and magnetic field sweep rate in Figure 5.3, for comparison with the theoretical map, Figure 2.6. Two field modulation frequencies were used, 900 c/s for low sweep rates and 3600 c/s for higher sweep rates. In the latter case, the sweep coils were series tuned with a $0.25 \mu\text{F}$ capacitor to increase the available sweep, as mentioned in section 4.8. Power level was varied in

steps of 2 dB and sweep rate in steps of ratio $^{10}\sqrt{10}$. At the highest sweep rate used, 6.3×10^5 gauss / second, the rate of evaporation of the helium increased considerably, the return line pressure rising from 2 mm to 6 mm. This would give rise to a change in T_1 due to the rise in temperature, but the correction for relaxation was only 3% ($\lambda = 1.03$) so that this was not considered important. The monitor klystron power was -26 dB (2.5×10^{-8} watts).

It can be seen that although there is a similarity of form between Figures 2.6 and 5.3, the agreement is not very good. In particular, the inversion at high power and moderate sweep speed is greater than expected from the theory developed in Chapter 2. This point is discussed in more detail in section 8.1. Another point is that the inversion efficiency did not exceed 4.7% ($Z_p = -.47$) and this was only obtained at the maximum sweep rate of 6.3×10^5 gauss / second, which is at least an order of magnitude higher than that quoted by Firth (2.87×10^4 gauss / second; Ref. 11, p 177). Only in the region of high sweep rate and lower pulse power do the two maps agree. This is to be expected, since in this region Z_p is almost independent of $\beta (1 / \gamma_{H_1} T_2)$.

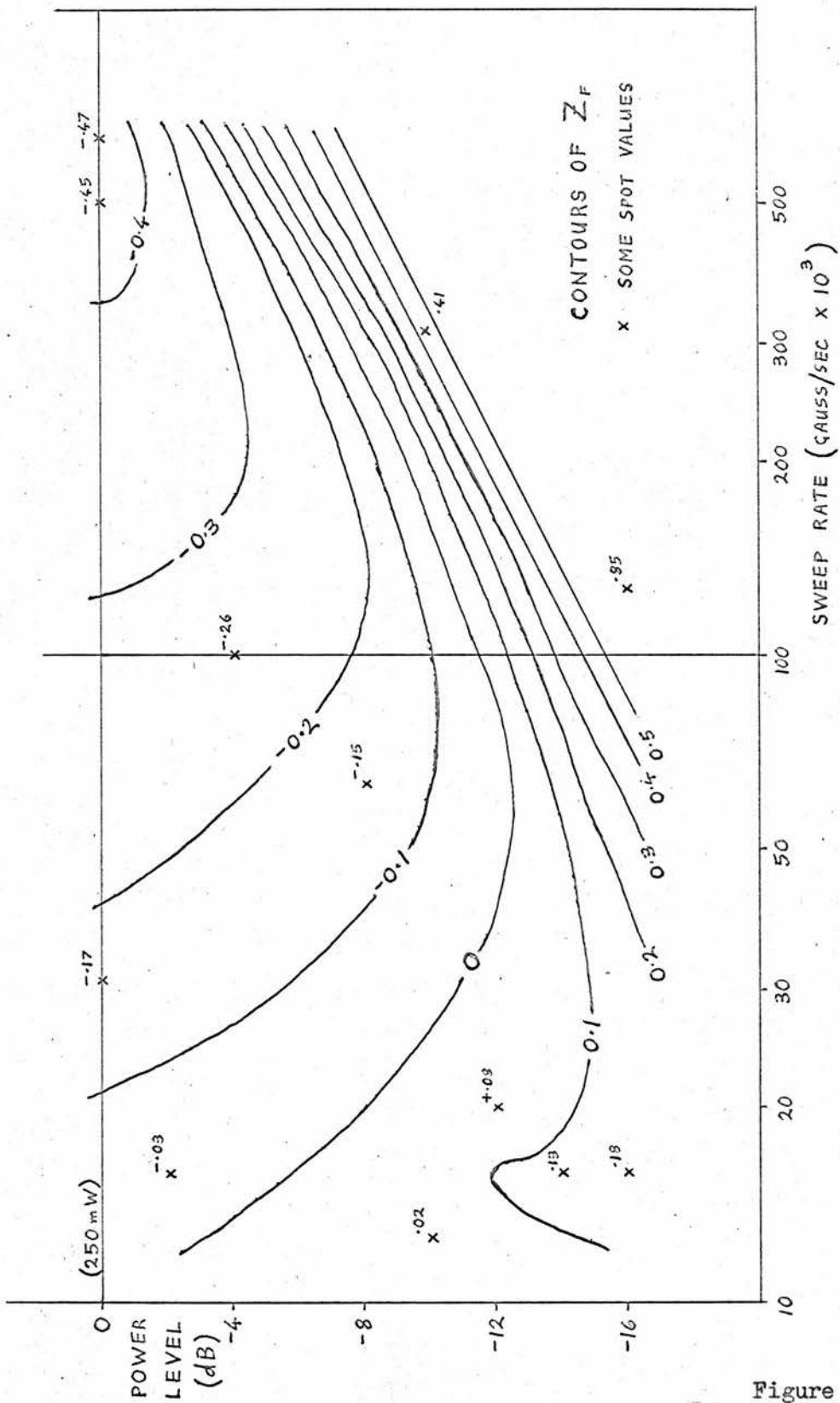
Figure 5.4 shows a similar map derived from inversion measurements on the lowest-field satellite of sample 2(b). This satellite was chosen because it had the least amount of unwanted structure around its base.

The experimental conditions were:

Field modulating frequency = 3600 c/s (tuned by 0.25μ F capacitor)

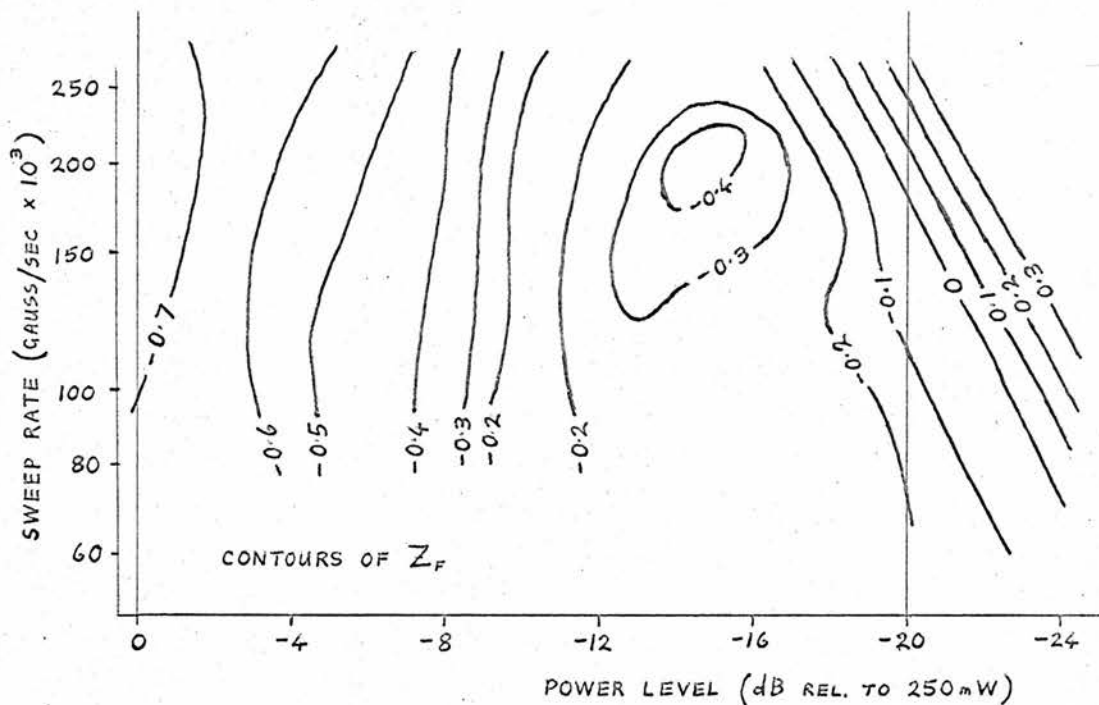
Monitor klystron power = - 20 dB (10^{-7} watts).

This map bears even less resemblance to the theoretical map, Figure 2.6,



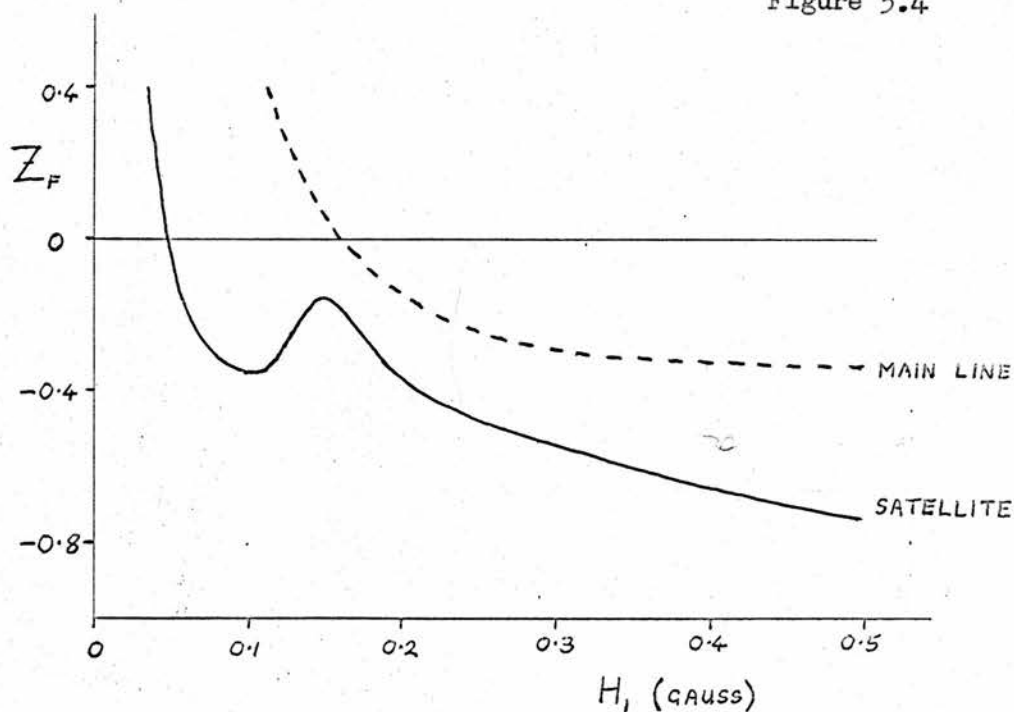
INVERSION MAP FOR MgO (2b) MAIN LINE

Figure 5.3



INVERSION MAP OF $MgO(2b)$ LOWEST SATELLITE

Figure 5.4



INVERSION AGAINST MICROWAVE FIELD

Figure 5.5

than that for the main line, but nevertheless contains some interesting features.

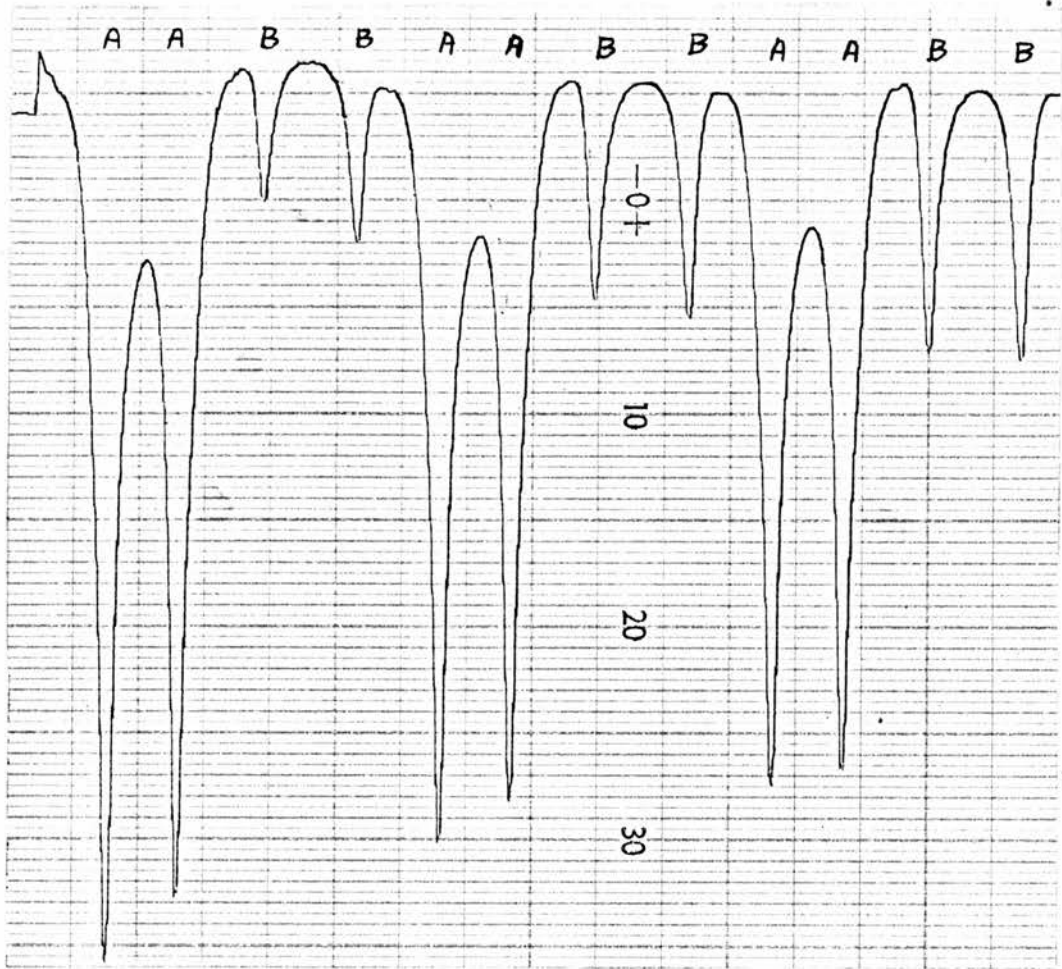
1) The inversion efficiency reaches 77% ($Z_p = -.77$) at one point on the map ($P = 250$ mW, $dH / dt = 2 \times 10^5$ gauss / second). This is a considerable improvement on the main line.

2) There is a pronounced, well defined valley at a power level of - 11 dB (20 mW), almost parallel to the field sweep rate axis. The fact that this dip in inversion efficiency is almost independent of sweep rate, yet critically dependent on power level would suggest some relatively time-independent process involving the magnitude of H_1 , which is approximately 0.15 gauss at this point (from Appendix 2). A graph of Z_p against H_1 is drawn in Figure 5.5 for $dH / dt = 1.6 \times 10^5$ gauss / second, and shows the effect quite clearly.

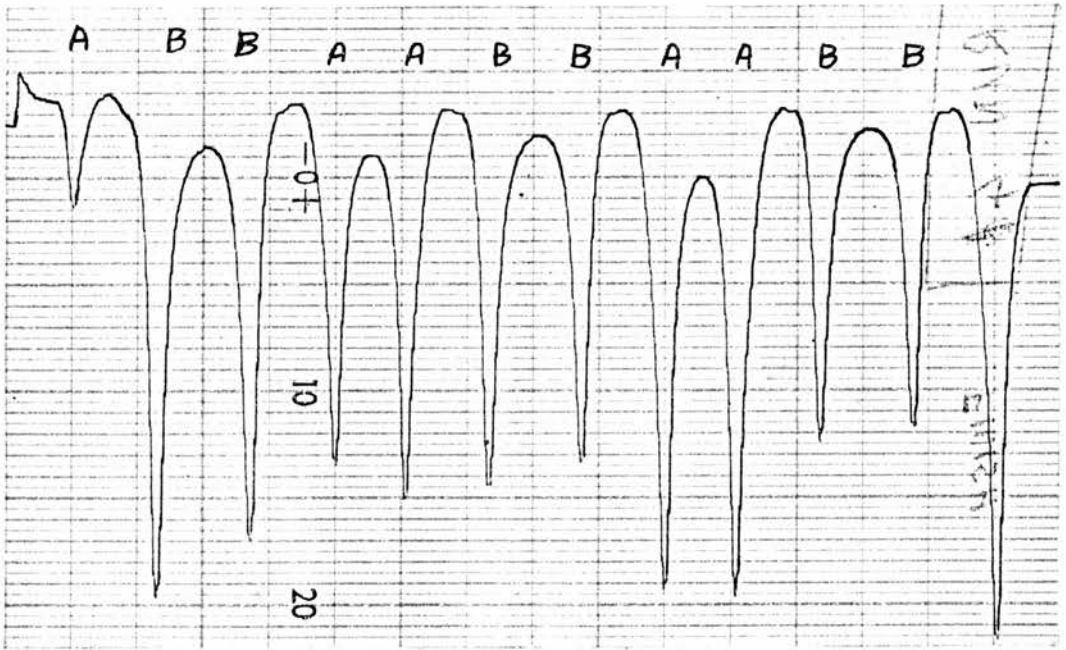
5.6 Observation of Reverse Relaxation.

Of particular interest is an observation of a reverse relaxation process occurring in the lowest of the six satellites of sample 7, and is shown in Figure 5.6. The recording was made using the Digital Memory Oscilloscope, and a field modulation of 30 gauss peak to peak at 80 c/s, the X.13 pulse being adjusted to cover the sub-satellite (line B) in one case, and the main satellite (line A) in the other. In both cases, the unsaturated line is seen relaxing from a state of greater-than-equilibrium population difference (reverse relaxation, i.e. from $Z > 1$ to $Z = 1$).

This effect is easily explained by assuming that the two transitions



A



B

RECORDINGS OF REVERSE RELAXATION

Figure 5.6

involved have a common energy level. Then saturation of one transition will immediately produce an increase in the population difference for the other transition, and hence a greater-than-equilibrium signal. In fact these three consecutive energy levels belong to the ${}^6S_{5/2}$ state of Mn^{++} , as pointed out in section 5.2, with $m_I = -5/2$; the main satellite (A) corresponds to the $m_S = +1/2 \rightarrow -1/2$ transition, and the sub-satellite (B) to either the $m_S = +3/2 \rightarrow +1/2$ or the $m_S = -1/2 \rightarrow -3/2$ transition.

5.7 Locus of the $Z_F = 0$ Contour.

When β is small in the normalised Bloch Equations (2.7), the $Z_F = 0$ contour tends towards a straight line given by $r = 2.26 (\pi/\ln 4)$. This also means that the ratio of sweep rate to incident power is constant, and using the relation given in Appendix 2, it can be shown that

$R^* = (dH / dt) / P = 40 \text{ gauss} / \text{microwatt second}$

using the same cavity parameters as in Appendix 2. The corresponding values obtained from experiment were

$R^* = 6.3 \text{ gauss} / \text{microwatt second}$ for the main line, and

$R^* = 67 \text{ gauss} / \text{microwatt second}$ for the lowest satellite.

The quantities P and Q_L are subject to an appreciable error in measurement, + 20% being a reasonable estimate for each. The discrepancy in the two values of R^* can not, however, be explained by such errors, since they were taken from the same sample on the same run. This point is discussed further in section 8.3.

CHAPTER 6

EXPERIMENTS ON PHOSPHORUS-DOPED SILICON.6.1 Introduction.

Phosphorus-doped silicon has already been extensively studied with regard to its E.S.R. properties and relaxation processes (see, for example, Refs. 28, 48 - 54). However, it is of interest because of its extremely long spin-lattice relaxation time, which can in some cases be measured in hours. The spectrum consists of two lines, each about 3 gauss wide, separated by 42 gauss, the splitting being due to the nuclear spin ($\frac{1}{2}$) of the P^{31} donor nucleus. Three relaxation processes are involved in this system:

- 1) The transitions $\Delta m_S = \pm 1$, $\Delta m_I = 0$ are the observed ones, characterised by a relaxation time T_S .
- 2) $\Delta m_S = 0$, $\Delta m_I = \pm 1$ are the nuclear transitions, characterised by a time T_N .
- 3) $\Delta m_S = \pm 1$, $\Delta m_I = \mp 1$ are the forbidden transitions, characterised by T_x . T_N is typically > 10 hours and T_x of the order of 30 hours at liquid helium temperatures (Ref. 52), thus leaving the T_S process dominant.

Phosphorus-doped silicon has also been used in an experimental two-level maser (Ref. 28), using isotopically pure silicon. By removing Si^{29} nuclei, which contribute to local field inhomogeneity by virtue of their magnetic moment, the line width can be reduced to 0.22 gauss, showing that most of the line broadening is inhomogeneous.

The sample used in the experiments described in this chapter was a rectangular block measuring 1.80 cm x 0.95 cm x 0.28 cm, weight 1.11 gms. The resistivity was measured and found to be 0.25 ohm cm, indicating a donor concentration of 3×10^{16} per cm^3 (Ref. 55). The total number of spins in the sample was estimated to be 1.4×10^{16} .

6.2 Measurements of Spin-lattice Relaxation Time (T_S).

Since the apparatus was primarily designed to measure relaxation times in the millisecond region, a new technique had to be devised to measure times in the range of seconds and minutes. The possibility of observing the recovery continuously was immediately discounted, since it was estimated that in ~~order~~^{order} to observe continuously a relaxation time of the order of ten minutes without affecting the system, a power level of less than 10^{-12} watts would be required. Apart from the inconvenience of such a low power, the sensitivity of the spectrometer would only be of the order of 10^{17} spins at liquid helium temperatures, in fact not enough to detect the sample.

It was decided to use the derivative-recording mode of the apparatus, with a fairly fast sweep rate, so that the "integral" line shape was observed, and the line completely saturated in the process. The field was kept about 15 gauss away from the line during the relaxation periods, and then swept through the line to about 15 gauss on the other side in about 5 seconds. A power level of 10^{-6} watts (-10 dB) was found to be suitable, being large enough to saturate the line fully, yet small enough to yield a reasonable signal. In this case the conditions of section 3.6

apply. The empirically optimised conditions (i.e. those giving apparently the best signal on the pen recorder) were:

Modulation depth	= ± 1 gauss
Sweep rate	= 6 gauss / second
Power level	= 10^{-6} watts.

Using the relationship between power level and H_1 derived in Appendix 2, this gives

$$\lambda = \omega_m \tau / r_o = 3.0$$

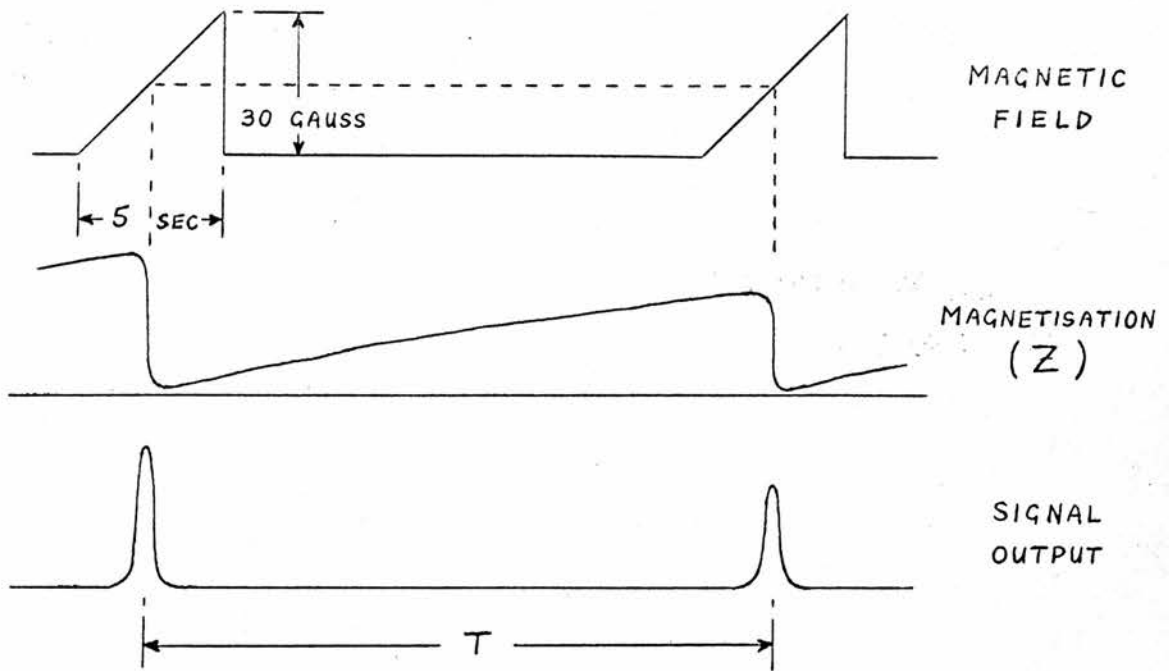
($\tau = 1/6$ sec., $r_o = 110$, $\omega_m = 2000$ sec. $^{-1}$) which is remarkably close to the theoretical optimum of 1.66. The degree of saturation of the line is given by

$$Z_f = \exp(-\pi\lambda) = 8 \times 10^{-5} \text{ when } \lambda = 3$$

and 5×10^{-3} when $\lambda = 1.66$

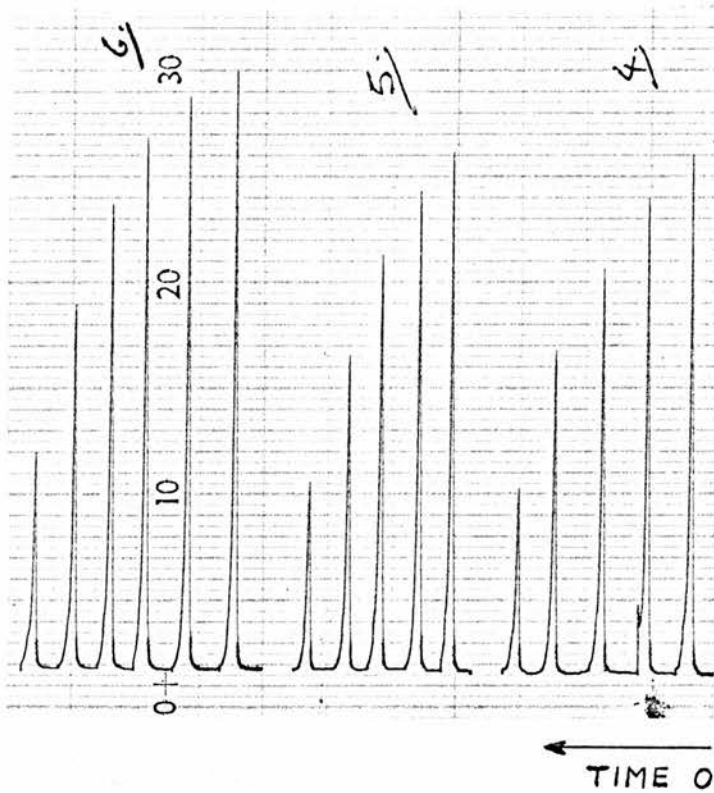
In either case it can be seen from Z_f that the line is well saturated, but since saturation is imperative, it is better to err on the side of large λ . The loss of sensitivity in taking $\lambda = 3$ is only 5% (using the first of equations 3.10 to compute $\lambda^{\frac{1}{2}} I_1$).

The procedure for measuring such long relaxation times is shown diagrammatically in Figure 6.1. When the field has been swept through the line, it is quickly returned to its steady value. This, of course, means another passage through the line, but it is very much faster than the first one, and consequently has very little effect on the line. Even if it were not fast enough, the error introduced by it would be of the order of 3 seconds, the time interval between passages, which is small



PROCEDURE FOR MEASURING LONG RELAXATION TIMES

Figure 6.1



TYPICAL
TRACES

Figure 6.2

compared with T_S in general. In any case, it does not give rise to any appreciable signal at the pen recorder, indicating that it has little effect on the line.

Signal height is measured over a series of time intervals (T in Figure 6.1) and fitted to an exponential recovery by the method discussed in Appendix 3. It is not necessary to have an arithmetic progression of time intervals, as is the case with the method discussed in section 5.3, nor is it necessary to know the equilibrium value of the signal. A typical sequence of pen-recordings is shown in Figure 6.2. The recorder drive is stopped during the time interval to save paper; hence the irregular spacing between lines has no significance and only the heights of the traces are important. The results are plotted in Figure 6.3.

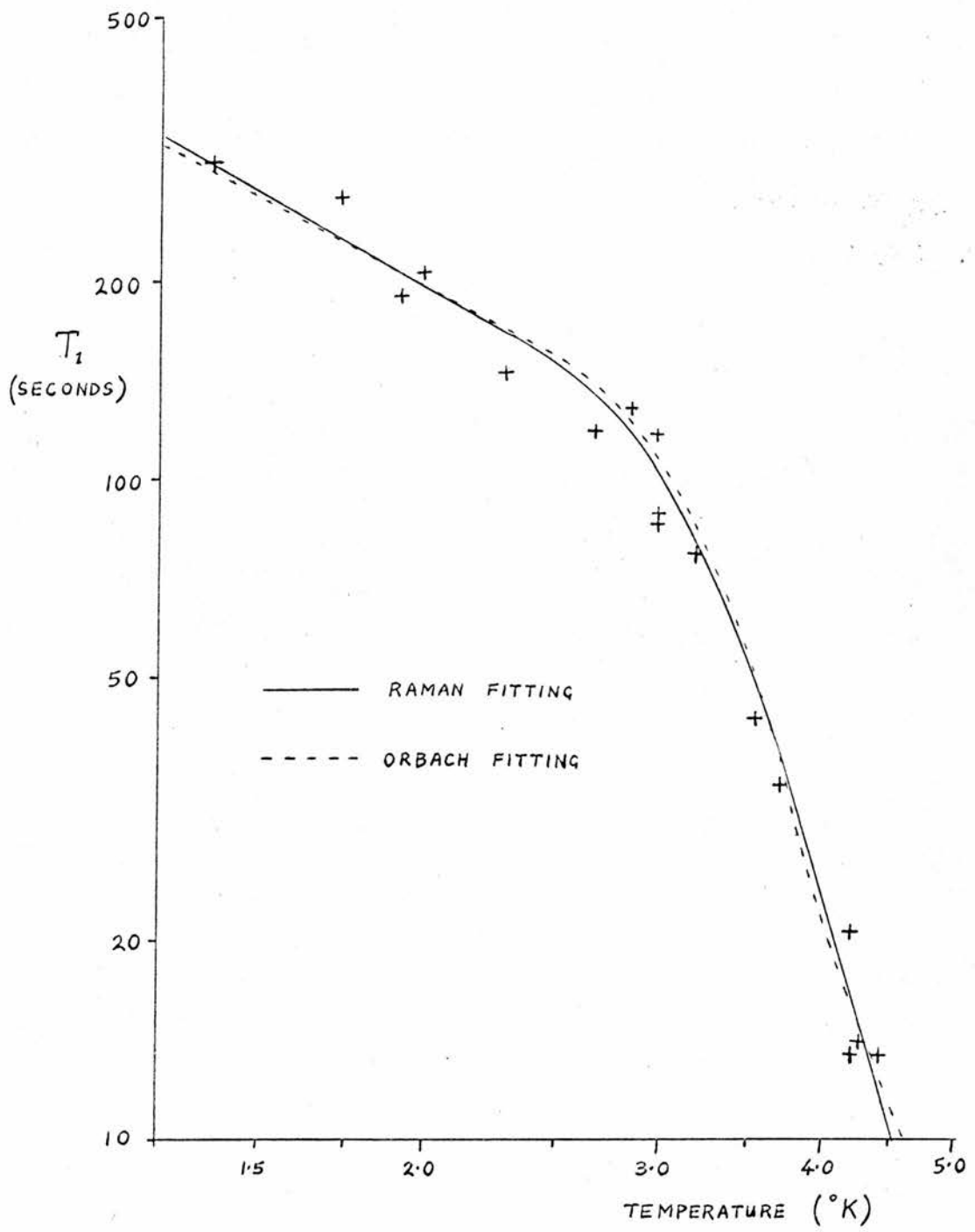
The curve of relaxation rate against temperature is seen to consist essentially of two portions, meeting at about 3° K. It has already been proposed (Refs. 52, 54) that a relationship of the form

$$T_S^{-1} = AT + BT^7$$

representing the Direct process and Raman process respectively, should hold. (A review of the various types of spin-lattice relaxation processes encountered in Electron Spin Resonance is given in Ref. 56.) It is, however, a fairly straightforward process to fit the observed points to a curve of the form

$$T_S^{-1} = AT + BT^G$$

This has been done by the method discussed in Appendix 4, which chooses



TEMPERATURE DEPENDENCE OF T_1 IN
P-DOPED SILICON

Figure 6.3

a curve giving the least mean square percentage error in T_S , and the following values are obtained for the sample under investigation:

$$A = 2.446 \times 10^{-3}$$

$$B = 1.792 \times 10^{-7}$$

$$C = 8.658$$

All times are measured in seconds, and all temperatures in degrees Kelvin.

By a similar method, the points can also be fitted to a curve of the form

$$T_S^{-1} = AT + B \exp(-C / T)$$

which would be expected for a combination of the Direct process and an Orbach process. This gives

$$A = 2.515 \times 10^{-3}$$

$$B = 121.1$$

$$C = 33.15$$

This value of C would indicate an excited state 23 cm^{-1} above the donor levels. In fact the conduction band in phosphorus-doped silicon is 350 cm^{-1} above the donor level (Ref. 57), so that an Orbach process is most unlikely. However, the value $C = 8.658$ for the Direct + Raman case would point to a T^9 Raman process. Carrying out the curve-fitting procedure on Feher's points (Ref. 53) yields an exponent of 8.3.

6.3 Inversion Measurements.

Because of the long relaxation time, it was not possible to carry

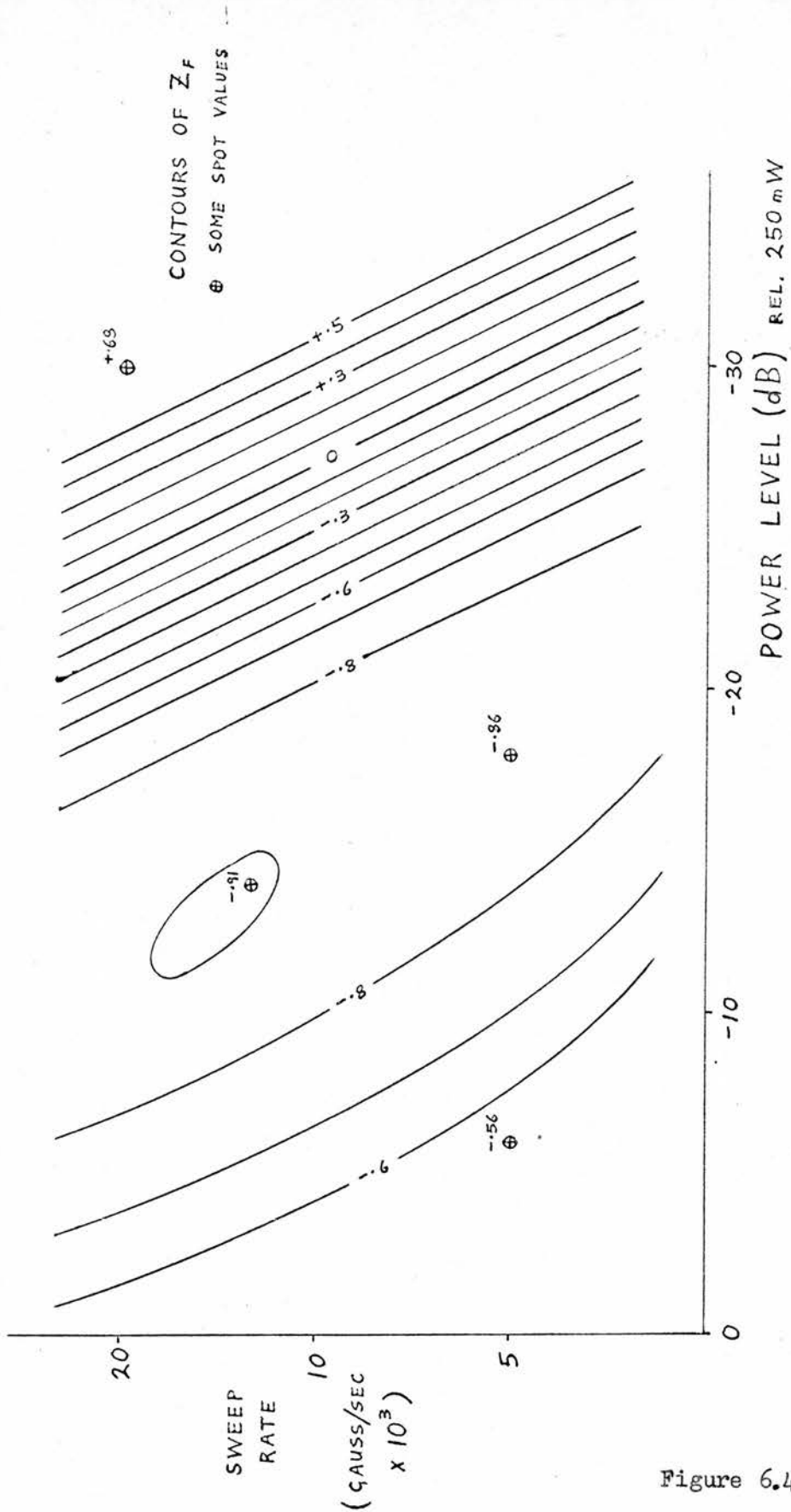
out inversion measurements by the technique described in section 5.4, as the recovery time would be prohibitively long from the point of view of observation. Furthermore, the pulse circuits were not designed to cover such low repetition rates as would be required. A multiple inversion technique was devised in which the line, initially fully recovered, is successively inverted and re-inverted by consecutive X.13 pulses. Each time the signal diminishes by a factor Z_f . It is monitored continuously using a very low monitor klystron power (-30 dB, or 10^{-8} watts). All the experiments were carried out at 4.2° K, where T_1 is of the order of 20 seconds, to avoid an inconveniently long recovery time. The number of inversions, N , required for the signal to reach 1/10 of its initial size (i.e. approximately noise level) was noted. Hence

$$|Z_f| = \sqrt[N]{0.1}$$

The results are shown in Figure 6.4 and are discussed in section 6.4. There are, however, a number of possible sources of error in this technique as it stands.

1) Strictly speaking, the relaxation time should be infinite and the monitor power level zero. The error is of the order of $\Delta T / T_0$, where ΔT is the time interval between inverting pulses, and T_0 is the effective relaxation time, i.e. that observed in the presence of monitor klystron power. Since $\Delta T = 1/5$ second and $T_0 > 10$ seconds, the error in Z_f from this cause should be of the order of 2%.

2) The estimate of when the signal reaches 1/10 of its initial value



INVERSION MAP FOR P-DOPED SILICON

Figure 6.4

is subjective, since this is of the order of noise level. The error from this cause decreases as $Z_f \rightarrow -1$, since N is then large (in taking the N th root, the fractional error is reduced to $1/N$ of its original value). The only other case which shows up accurately is when $Z_f = 0$, since then the signal disappears after the first passage.

3) To allow the line to recover, it is necessary to shift the timing of the X.13 pulse with respect to the modulation, so that it occurs mainly at one extreme of the modulation, well away from the line. It must then be shifted manually onto the line within the $1/5$ second between pulses. This procedure can sometimes fail; if the operation has not been completed by the time the pulse arrives, there is a chance that the leading edge of the pulse will occur somewhere on the line. Because the line is inhomogeneously broadened, the effect of this is to invert part of the line and leave the rest of it. Since it is necessary to wait at least half a minute for the line to recover, this can be quite annoying.

An attempt was made to overcome the subjective errors in this experiment by pen-recording the signal. To do this, the field modulation frequency had to be 320 c/s, and the line positioned somewhat off-centre with respect to the modulation, to give a useful 320 c/s component in the signal. A block diagram of the system used is shown in Figure 6.5. The signal from the second detector is passed through the gating circuit to remove the signal due to the inverting pulse, then to the narrow band amplifier and phase sensitive detector to extract the 320 c/s component. The output of the phase sensitive detector is smoothed by a filter having a short time constant (about .04 seconds) and fed to the Digital Memory

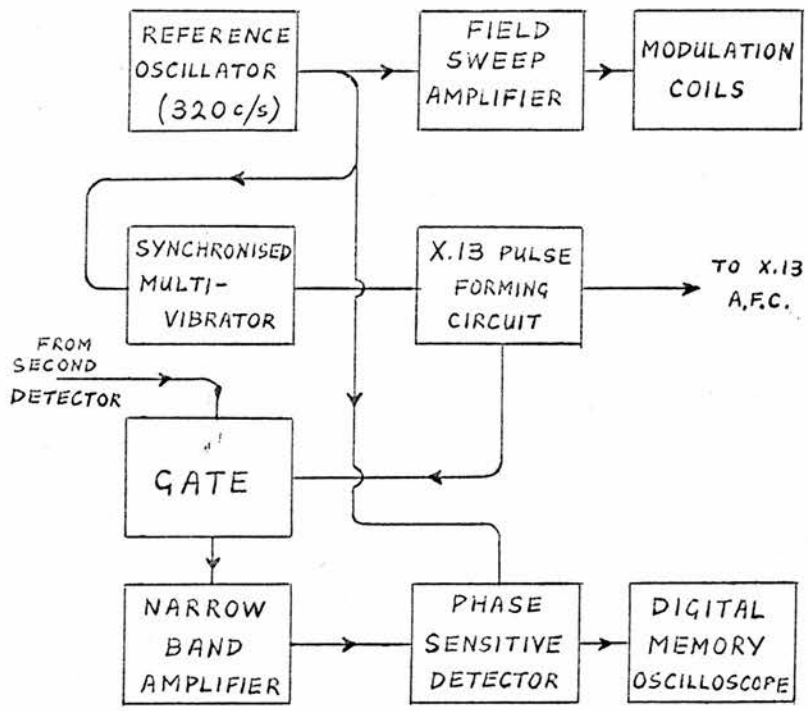
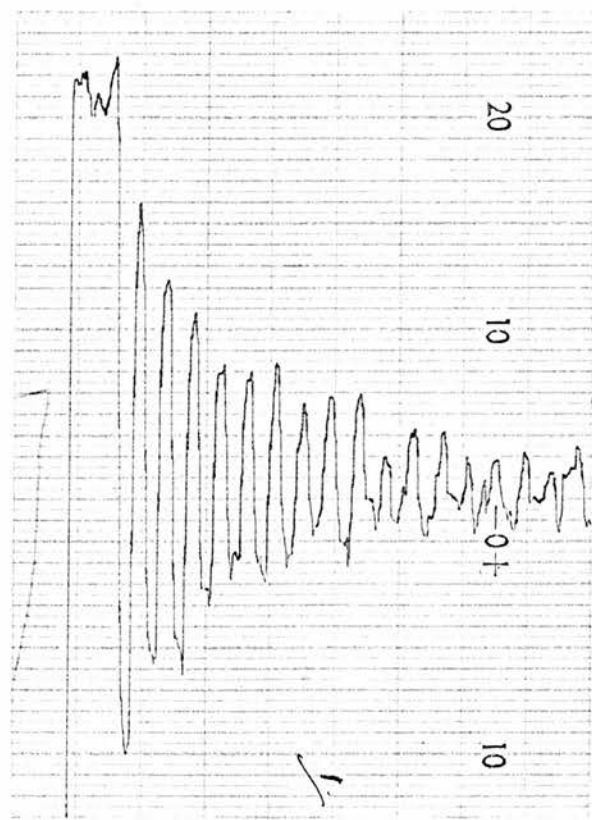


Figure 6.5

SYSTEM FOR RECORDING MULTIPLE INVERSION



TYPICAL
RECORDING

Figure 6.6

Oscilloscope, which in this case merely stores the signal for subsequent pen-recording. Figure 6.6 shows a typical recording. It can be seen immediately that the recording is noisy, and would not seem to give much better results than direct observation on the oscilloscope. Much of this noise is due to the fact that the signal due to the line occupies only a small fraction of the total time, and if the signal from the second detector was gated every modulation cycle to allow only this useful signal to pass, the noise could be reduced considerably.

6.4 Estimate of T_2 .

Figure 6.4 shows that over a wide range of sweep rate and power level, inversion in phosphorus-doped silicon is very efficient, reaching an estimated 91% at 13,000 gauss / second and 10^{-2} watts (-14 dB). This does not take into account the factors of relaxation and monitor power level, so that the true value could well be higher. The map corresponds much better to the theoretical one (Figure 2.6) than do those for MgO, since it exhibits a fall in inversion efficiency at high power levels, unlike MgO. This is, in fact, an example of region III in Figure 2.5, and should therefore obey the law

$$Z_f = - \exp (-\pi r / \beta) \quad \text{from Appendix 1.}$$

For a given sweep rate, $r \propto \text{power}^{-1}$ and $\beta \propto \text{power}^{-\frac{1}{2}}$. Taking the point where sweep rate = 5000 gauss / sec. and power = 50 mW (-7 dB), the value of $Z_f = -0.6$, corresponding to $r / \beta = 0.17$. At the same sweep rate, the power corresponding to $r = 2.26$ ($Z_f = 0$) is 0.25 mW (-30 dB),

indicating that $r = .011$ at the point in question. Hence $\beta = 1.9 \times 10^{-3}$.

Taking $H_1 = 0.22$ gauss (corresponding to 50 mW, by Appendix 2), this gives $T_2 = 0.13$ milliseconds, which is long by E.S.R. standards (T_2 is normally less than a microsecond), but is nevertheless consistent with the picture of well isolated donor units in the silicon lattice. Other workers have shown by ENDOR techniques (Ref. 58) and isotopic purification (Ref. 28) that much of the observed 2.7 gauss line width in silicon is due to inhomogeneous broadening by Si^{29} nuclei. The fact that holes can be burnt in the line with great ease indicates a considerable amount of inhomogeneous broadening. $T_2 = 0.13$ milliseconds corresponds to a basic line width of only 4×10^{-4} gauss.

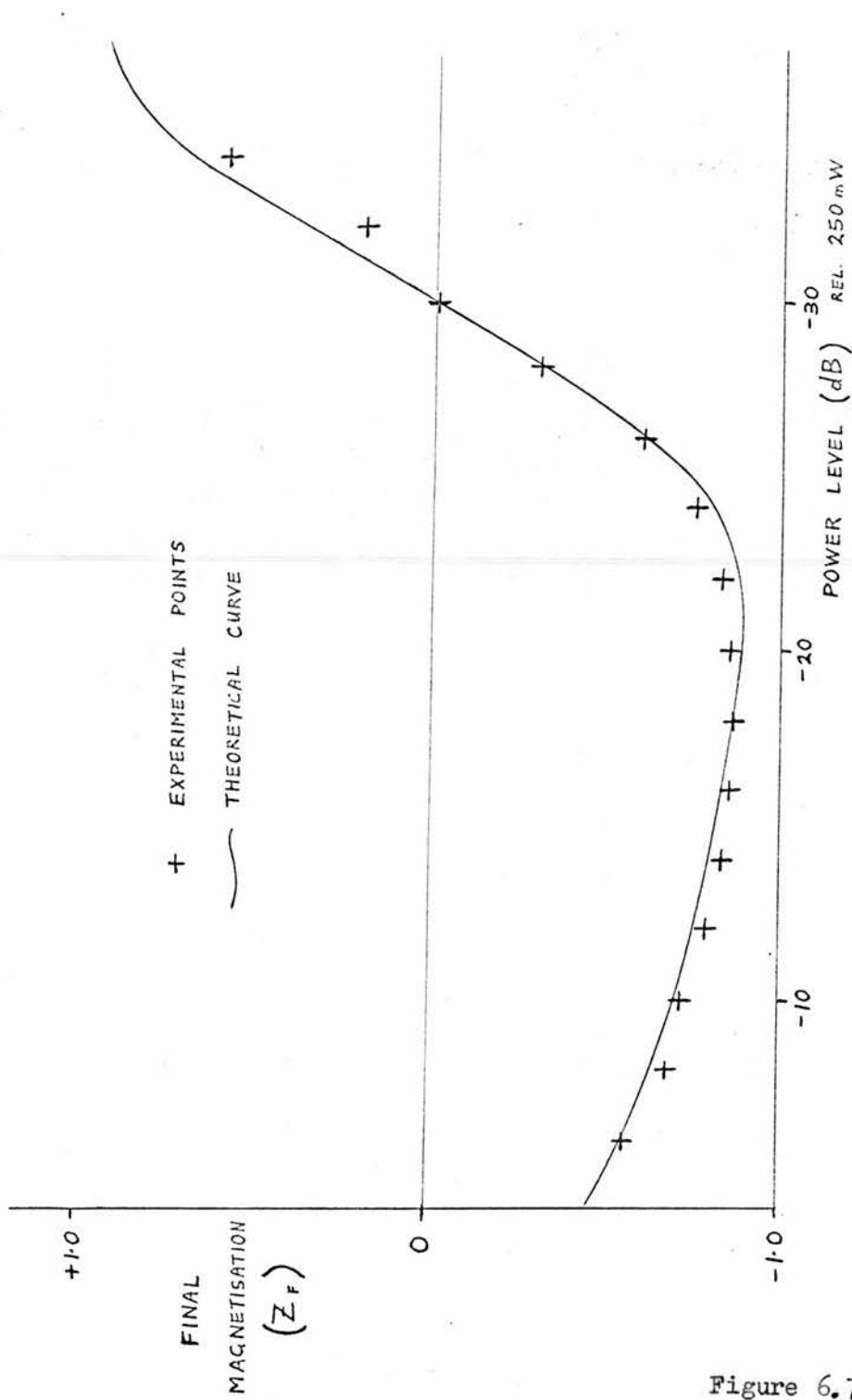
Inversion (Z_p) has been plotted against power level for a sweep rate of 5000 gauss / second in Figure 6.7, along with the theoretical estimate, based on $T_2 = 0.13$ milliseconds. The agreement between experiment and theory is seen to be quite good.

6.5 Locus of the $Z_p = 0$ Contour.

This contour is well defined for silicon, and gives a sweep rate to power ratio

$$R^* = 30 \text{ gauss / microwatt second}$$

which agrees with the calculated value of 40 gauss / microwatt second within the limits of experimental error. In this region, both T_1 and T_2 are unimportant, and apart from the presence of a shift due to the nuclear spin of P^{31} , the spins are effectively free. It would be very surprising, then, if R^* were significantly different from that expected



INVERSION IN P-DOPED SILICON AT 5×10^3 GAUSS/SEC.

Figure 6.7

for free spins.

6.6 Optical Stimulation.

The effect of light on the relaxation processes in silicon is already well known (Ref. 52). Optical stimulation was used in the experiments described in this thesis mainly to accelerate recovery of the line at low temperatures. It was achieved by passing light from a tungsten lamp down the quartz tuning rod of the cryostat, using the rod as a light pipe. This excites electrons from the donor levels and allows them to diffuse and settle in other donor sites. It also excites electrons from the valence band, some of which will find their way into donor sites, and in consequence some originally in donor states will drop into the valence band. The first process will give rise to a sharp decrease in T_N , since the orientation of the nuclear spin in the new donor site is independent of that in the initial site. Also, during the process of changing site, symmetry is lost, resulting in an increase in the spin-lattice relaxation rate (T_S).

What is observed under optical stimulation in the present experiments is that the two lines tend to equalise first, one growing while the other shrinks, followed by an increase of both lines towards their equilibrium size. The first of these is distinctly a T_N process, and the slower one is a T_S process. No evidence of a T_X process has been observed.

CHAPTER 7

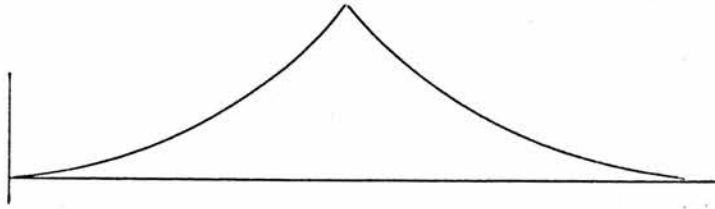
EXPERIMENTS ON NEUTRON-IRRADIATED DIAMOND.7.1 Introduction.

Six specimens of neutron-irradiated diamond were made available by courtesy of the University of Reading, and irradiated by A.E.R.E., Harwell. In two of the specimens, D 23 and D 24, the initial neutron dose was insufficient to give useful E.S.R. signals, and these were re-irradiated to intermediate dosages. A list of the specimens with their dosages and estimated spin concentrations is given in Table 3. The diamonds are thin wedge-shaped slices of type II diamond, cut from a natural stone. The shapes are irregular, but roughly 5 mm square and less than 1 mm thick. One of them is shown in Figure 4.5, mounted on the bridge sample-holder.

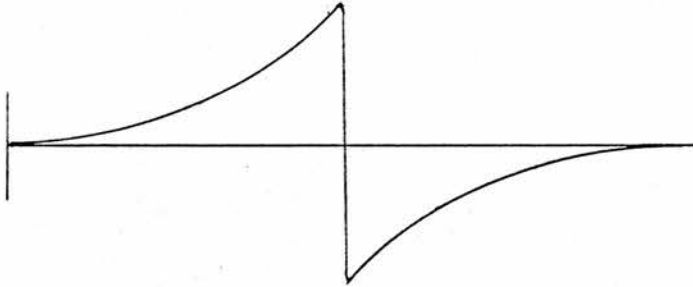
The E.S.R. spectrum of neutron-irradiated diamond has been fairly well studied (Refs. 59 - 63) but no work has so far been reported on its relaxation properties, except briefly by Campbell (Ref. 10).

7.2 Nature of Spectrum.

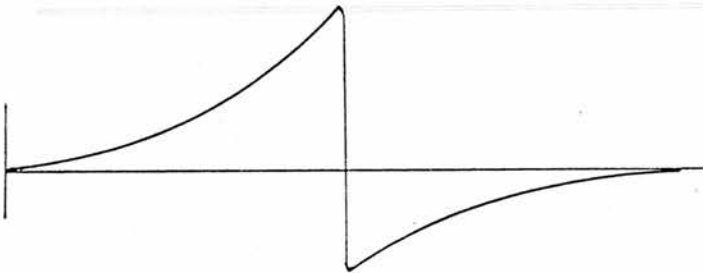
Faulkner et al. (Refs. 59, 62) have suggested four distinct systems of lines which they label a, b, c and d. These systems are also found in electron-irradiated diamond, but in neutron-irradiated specimens, the "d" system predominates. The spectrum may be described as "volcano-shaped" (shown in simplified form in Figure 7.1) and has a half-power width of about 80 gauss, independent of dosage. It is suggested (Ref. 59)



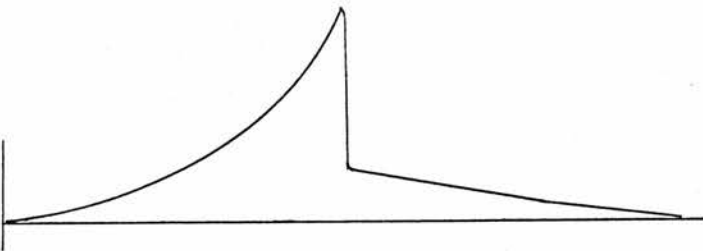
DIAMOND LINE
SHAPE



DERIVATIVE
SPECTRUM



EFFECT OF A
SMALL AMOUNT
OF
"INTEGRATION"



EFFECT OF A
LARGE AMOUNT
OF
"INTEGRATION"

DIAMOND SPECTRA (DIAGRAMMATIC)

Figure 7.1

that this system is built up from a range of triplet systems ($S = 1$) caused by vacancy-interstitial pairs. The intensity of the line is more or less proportional to neutron dosage.

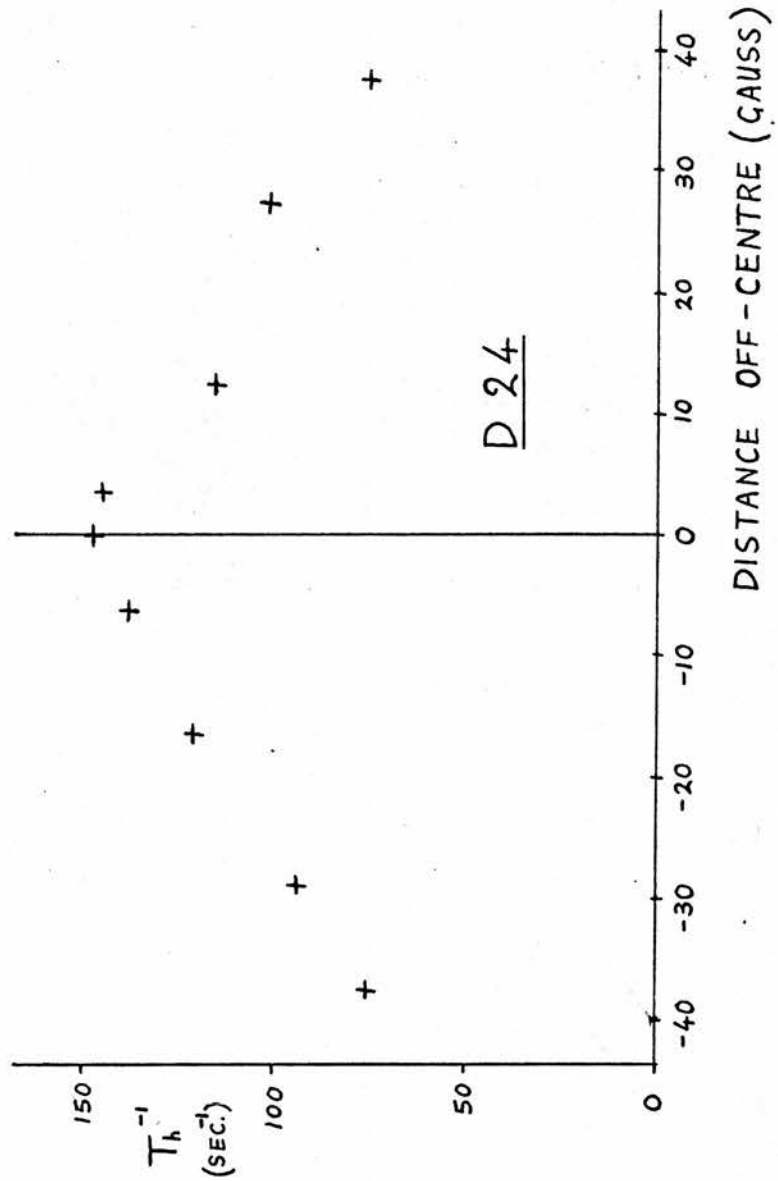
7.3 Relaxation of Holes.

If, instead of saturating the whole line, the X.13 pulse is applied over a small fraction of the line, say one gauss or less, using a modulation of 2 to 3 gauss, a "hole" may be burnt in the line (see section 3.2), and it is of interest to observe the decay of this hole on successive half-cycles of the modulation. This decay has a characteristic time T_h , and represents the relaxation time of the spin packets constituting the hole. The following points were observed:

1) The relaxation rate T_h^{-1} is practically independent of hole width, at least for holes which are narrow compared with the overall line width.

2) T_h^{-1} is dependent on which part of the line the hole is burnt in. It is substantially higher in the central region of the line than in the wings, as is shown in Figure 7.2, which shows the variation of T_h^{-1} with hole position in D 24 at 1.4° K.

3) T_h is strongly dependent on spin concentration, much more so than \bar{T}_1 , the overall relaxation rate for the whole line, discussed in section 7.8. In D 29, for example, T_h is only 160 microseconds at the centre of the line at 1.4° K, whereas in D 23, it is seemingly longer than \bar{T}_1 , being of the order of 70 milliseconds. More details are given in Table 3. The figure for T_h^{-1} in D 23 is questionable because it is inconveniently low for accurate measurement. In general, all the results for D 23 must



VARIATION OF HOLE RELAXATION RATE WITH POSITION

Figure 7.2

TABLE 3.Properties of Neutron-irradiated Diamond Samples.

Sample	D 23	D 24	D 25	D 26	D 27	D 29
Weight (gms.)	.104	.082	.034	.044	.076	.070
Neutron Dose (n / cm ²)	3x10 ¹⁶ †	1.8x10 ¹⁷ †	10 hours*	30 hours*	120 hours*	1000 hours*
Estimated Spin Density (cm ⁻³)	6x10 ¹⁶	3x10 ¹⁷	1x10 ¹⁶	3x10 ¹⁶	1.2x10 ¹⁷	1x10 ¹⁸
Colour	Green	Very dark green	Very pale green	Pale green	Dark green	Black
T _h ⁻¹ (centre) at 1.4°K (sec. ⁻¹)	15 ?	160	-	-	80	6250
T _l ⁻¹ at 1.4°K (sec. ⁻¹)	23	53	-	-	29	260

† 1 MeV neutrons, Dounreay.

* Dose at pile factor 6, B.E.P.O., Harwell.

be regarded with some caution, since the signal is weak due to the low concentration of spins. As a rough estimate,

$$T_h^{-1} \text{ (centre)} \propto (\text{concentration of spins})^{2.5}$$

7.4 Other Characteristics of Holes.

In the most concentrated sample, D 29, some difficulty was found in burning holes in the line, because of the very short relaxation time. One significant observation is that the sides of the hole are noticeably rounded off, to the extent of about $\frac{1}{2}$ gauss. This is to be compared with the holes burnt in D 24 and weaker samples which are all as sharp as the limits of resolution of the apparatus; that is, about 0.1 gauss. Also, in the weaker samples, the sharpness of the holes decreases at higher pulse powers, as discussed in section 3.2 and illustrated in Figure 3.1. At full X.13 power, the rounding off is of the order of $\frac{1}{2}$ gauss, which is as expected, since $H_1 \doteq \frac{1}{2}$ gauss at maximum power ($P = 250$ mW). The unsharpness of the holes burnt in D 29 is due to spin-spin broadening of the basic spin packet.

7.5 Variation of Hole Depth with Sweep Rate and Power.

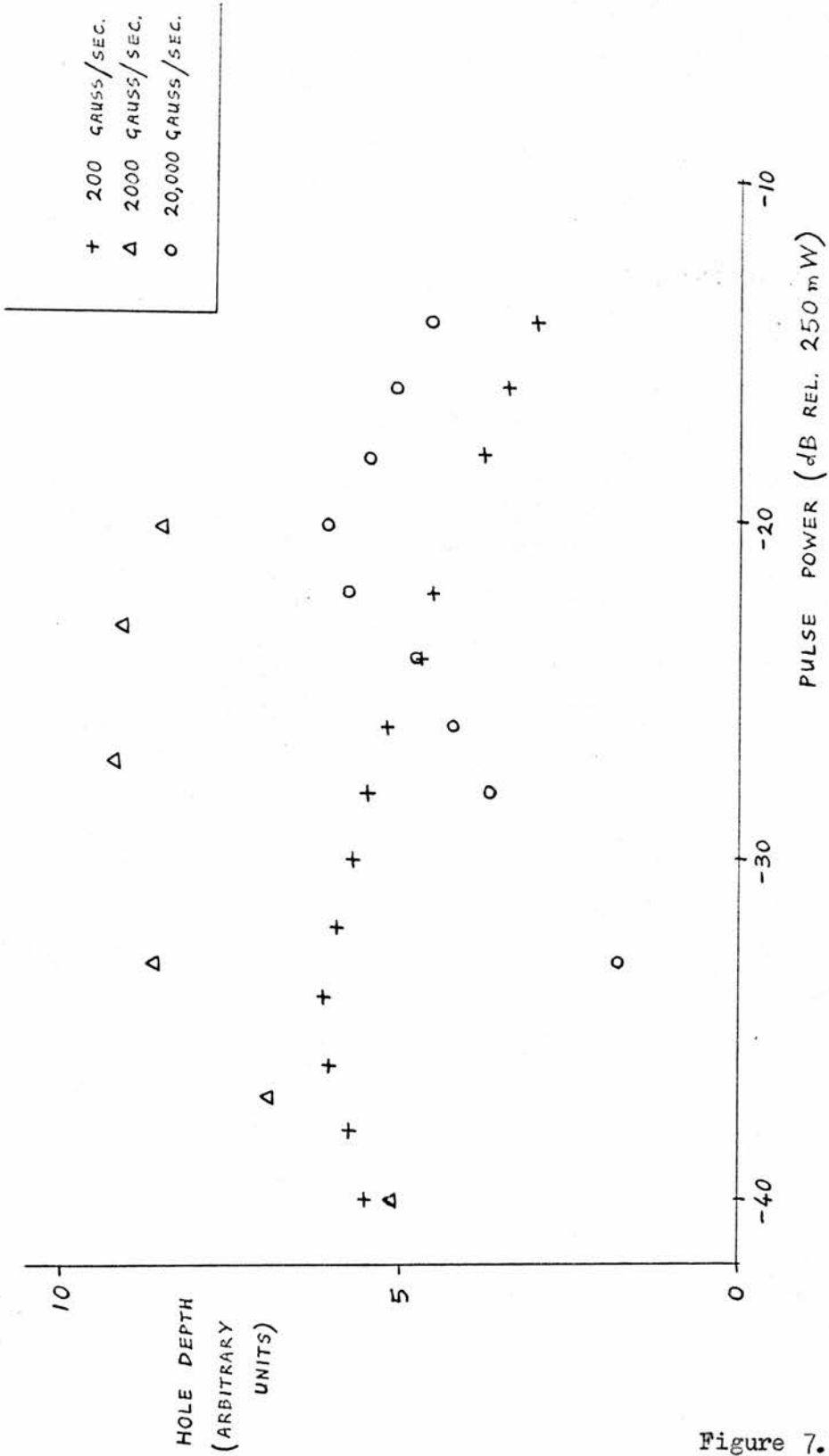
These experiments were of a similar nature to the inversion experiments carried out on MgO and silicon except that in this case only a fraction of the total spins was involved, i.e. those within the bounds of a "hole". Since the complete line is not covered, there can be no definition of a $Z_f = 0$ base line. The depth of a hole is proportional to $1 - Z_f$, and is plotted against pulse power level for three different

sweep rates in Figure 7.3. The shape of these curves would indicate that the holes do in fact represent inverted spins at maximum depth, since the hole depth decreases again at higher pulse powers. If the holes were merely saturated spins, this decrease would not occur. On the assumption that the maximum hole depth in the 2000 gauss / second case represents nearly complete inversion, $Z_f = 0$ occurs at about -40 dB, or 25 microwatts. This would indicate $R^* = 80$ gauss / microwatt second, about double the value expected (see section 5.7). However, it is consistent with the idea of $S = 1$, which leads to double the transition probability expected for $S = \frac{1}{2}$, as deduced in Appendix 5.

7.6 Intermediate Passage Experiments.

The nature of the E.S.R. spectrum of neutron-irradiated diamond makes it a suitable substance for the study of intermediate passage effects since, with the exception of D 29, the basic line width (i.e. of one spin packet), as indicated by the hole-burning experiments is very small. Thus, almost all the line broadening is inhomogeneous, so that the conditions of Chapter 3 should hold.

For these experiments, the apparatus is used in its derivative-recording mode, as shown in Figure 4.3 and discussed in sections 4.10 and 4.11. A very short integrating time constant is used, of the order of .04 seconds, and the signal output initially stored on the Digital Memory Oscilloscope, as the pen-recorder is not sufficiently fast. Sweeps of the order of 10 seconds were used, followed by reverse sweeps at the same rate. This was carried out using the induction feedback discussed



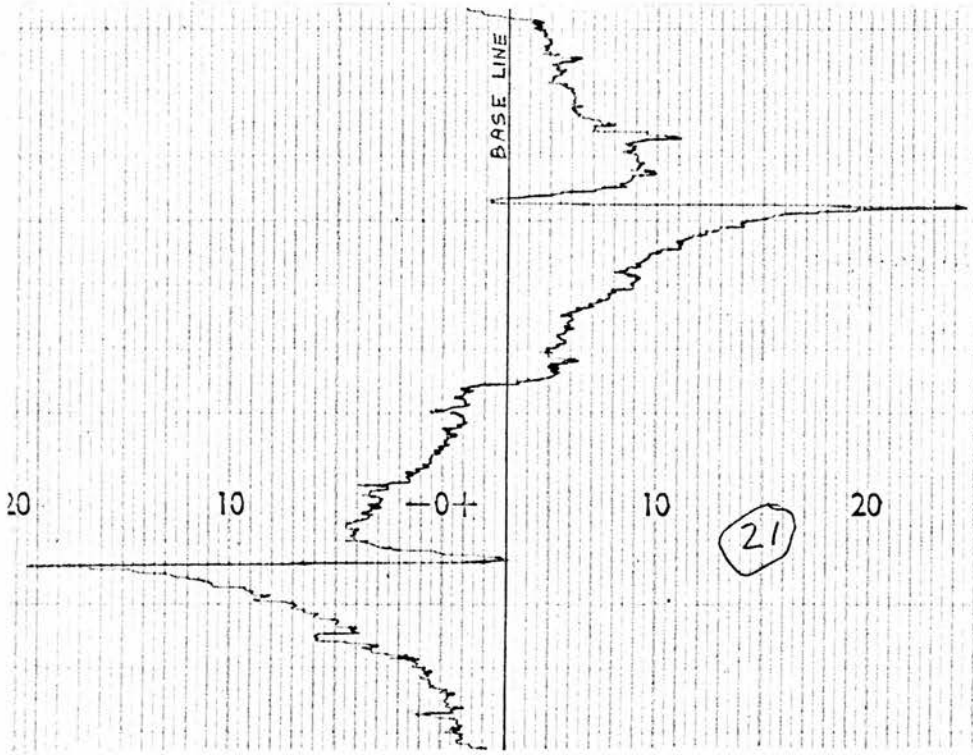
VARIATION OF HOLE DEPTH WITH PULSE POWER

Figure 7.3

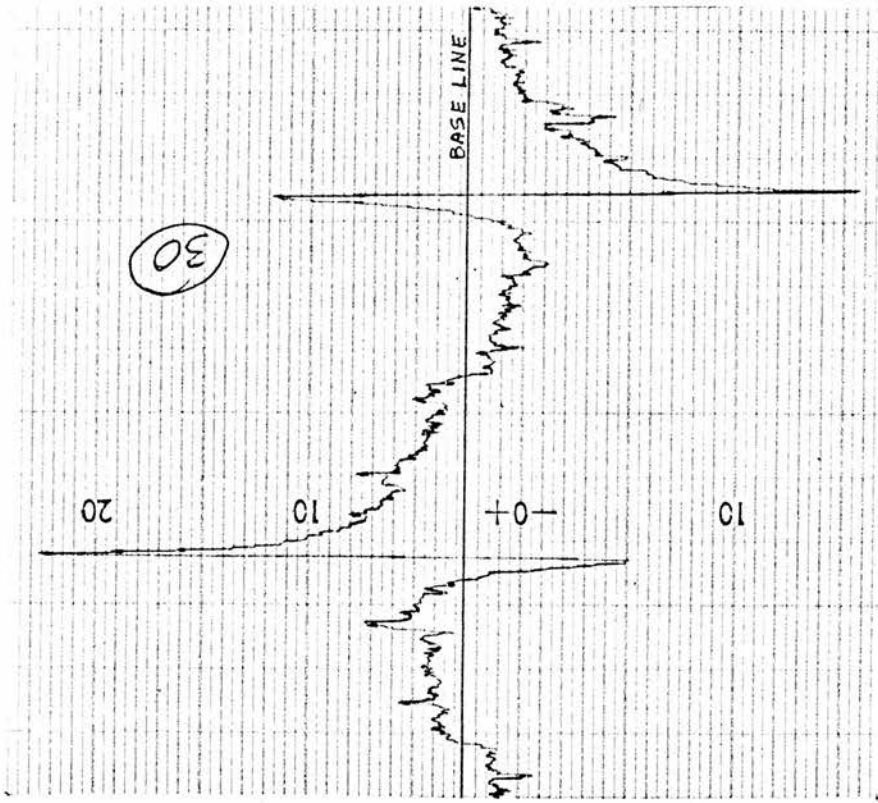
in section 4.8, since this worked reasonably well at such high sweep rates (normally sweeps last several minutes in derivative recording). The forward and return sweeps could be set to the same rate within the limits of accuracy of the voltmeter connected to the search coils (AVO meter). A selection of the signals obtained is shown in Figure 7.4, the details of the experimental conditions being listed in Table 4.

It is not easy to interpret these traces quantitatively (see below), although it can be seen that they differ in amounts of "integration", the phenomenon discussed in Chapter 3. This "integration" leads to an asymmetry of the recorded line shape as illustrated diagrammatically in Figure 7.1. Also, on the reverse sweep (the second half of each trace in Figure 7.4), the sign of the "integral" component is reversed. Hence, the extent to which the second half of the trace differs from a mirror image of the first half gives an indication of the amount of "integration" present.

As pointed out in Chapter 3, the number of separate parameters involved in any one recording is appreciable, many being assumed to take extreme values. For example, the theory of section 3.5 assumes that $\omega_m T_1$ (T_1 here is the relaxation time of an individual spin packet and hence in theory equal to T_h , the hole relaxation time) is large, which is not strictly the case for this sample, D 27, where T_h is just over 10 milliseconds (i.e. $\omega_m T_1 = 20$), indicating that a certain amount of relaxation takes place between successive cycles of the modulation. However, r_0 is fairly large, as required by section 3.5.



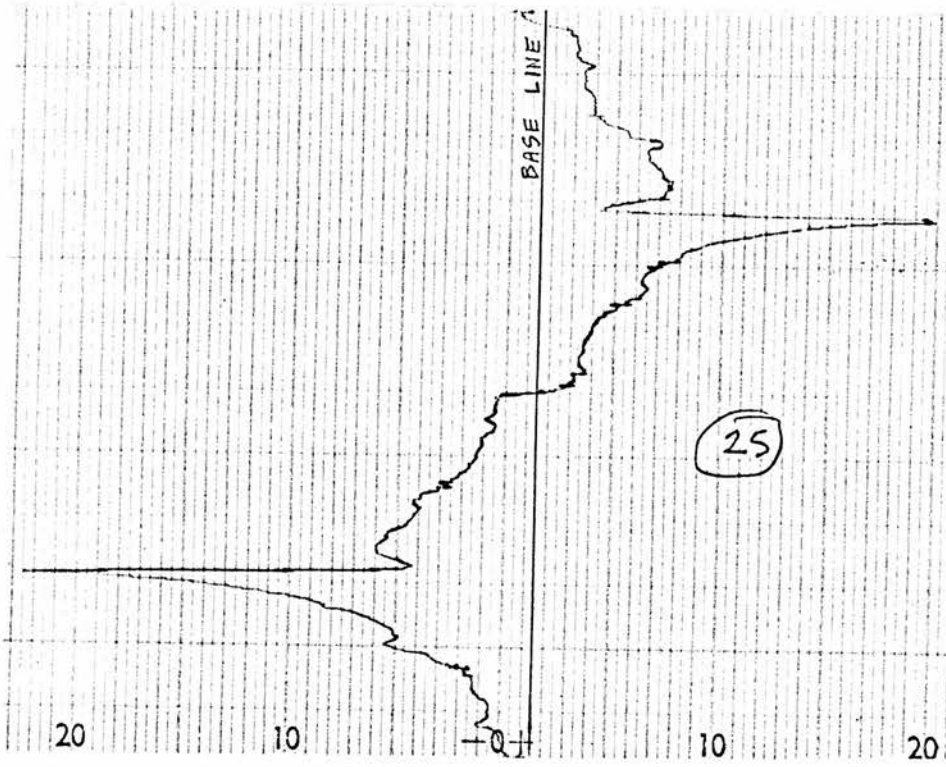
B



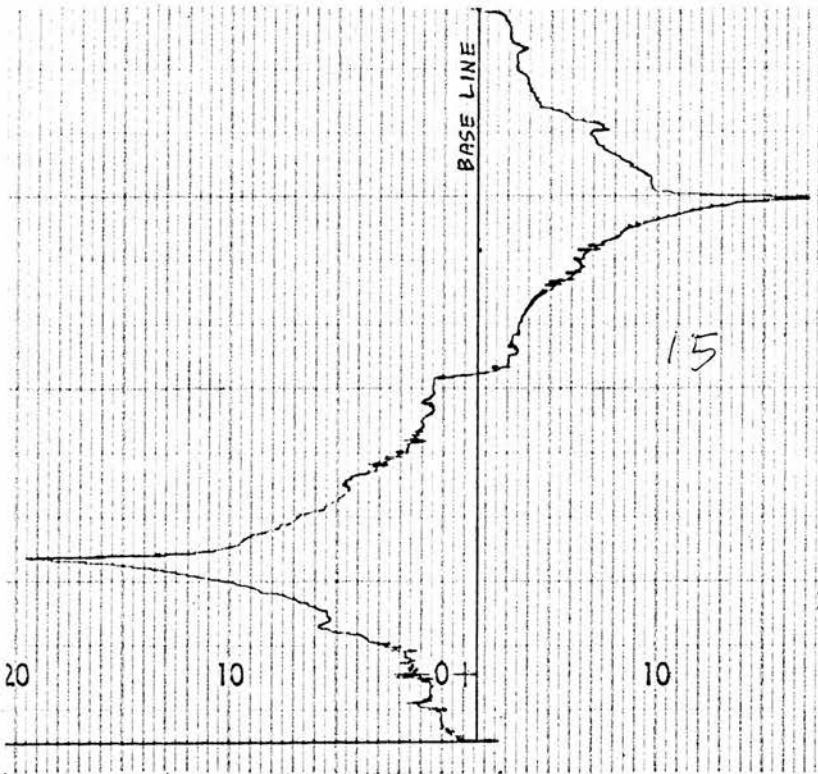
A

SIGNALS ILLUSTRATING THE "INTEGRATION" PHENOMENON

Figure 7.4



D



C

Figure 7.4
(continued)

TABLE 4.

Experimental Data for the Recordings shown in Figure 7.4.

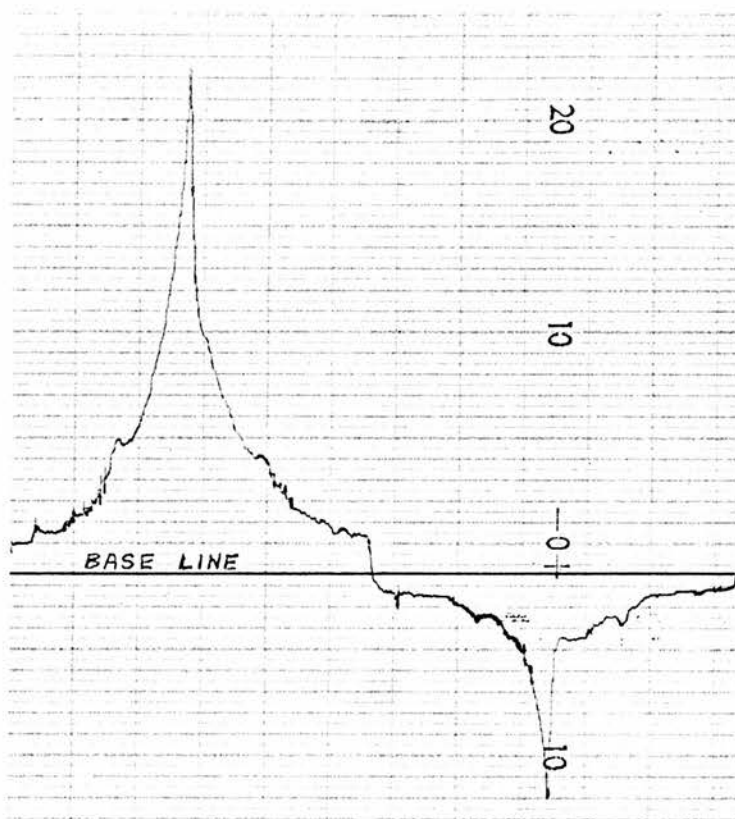
Trace	A	B	C	D
Modulation (gauss)	± 0.5	± 0.25	± 0.25	± 0.5
Klystron Power (dB rel. 10^{-5} watt)	-20	-20	-7	-7
H_1 (gauss)	3.2×10^{-4}	3.2×10^{-4}	1.4×10^{-3}	1.4×10^{-3}
τ (milliseconds)	17	8.5	8.5	17
r_o	560	280	14	28
$\lambda (\omega_m \tau / r_o)$.067	.067	1.3	1.3
T_o (based on $T_1 = 12.5$ msec.)	0.7	1.4	1.4	0.7
T_I (theory)	50	25	2.8	5.0
Modulation x T_I	25	6.25	0.7	2.5

Linear sweep rate (forward and reverse) = 29 gauss / second.

Modulation frequency = 320 c/s.

Taking $T_1 = 12.5$ milliseconds from Table 3, values of T_0 have been estimated and hence, by referring to Figure 3.9, the "integration time constant", T_I . These estimates are listed in Table 4. It must, however, be borne in mind that T_I is expressed in terms of the modulation depth, A . Thus, to obtain a figure for the "integration time constant" in terms of gauss (and hence length on the recording chart), the value of AT_I has also been tabulated. The amount of "integration" of the signal should be inversely proportional to this quantity, and it can be seen from Figure 7.4 that there is a fair correspondence, inasmuch as it can be judged by eye.

The amount of integration observed increases with power level (i.e. λ) up to a certain point, after which there is no significant increase. For example, at a power level of 0 dB (10^{-5} watts, $\lambda = 6.7$) the trace is not significantly more integrated than at -7 dB ($\lambda = 1.3$), although it distorts somewhat. This distortion is shown in Figure 7.5, where the signal on the reverse sweep is noticeably smaller than that on the forward sweep. The most likely reason for this is the breakthrough of some dispersion signal which, in the case of saturating passage, becomes very large in proportion to the absorption signal, and may not be completely suppressed by the A.F.C. systems, as pointed out in section 4.14. Furthermore, since the polarity of the dispersion signal is independent of field sweep direction, it would augment the signal in one direction and reduce it in the other, as observed. A fairly extensive treatment of dispersion signals under passage conditions is given by Weger (Ref. 25).



DISTORTED INTEGRATION
(SEE TEXT)

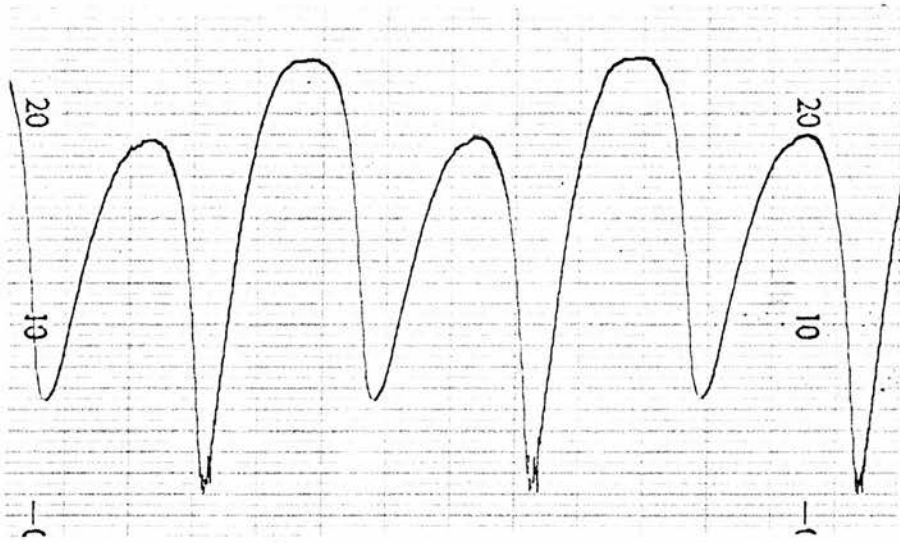
Figure 7.5

Another complication in these experiments is the non-uniformity of the spin packets constituting the line. Those in the wings of the line relax more slowly than those nearer the centre (Figure 7.2), giving a higher value of T_0 and hence a lower T_I in the wings. Thus the wings are more "integrated" than the central part, making the line appear wider than the original spectrum.

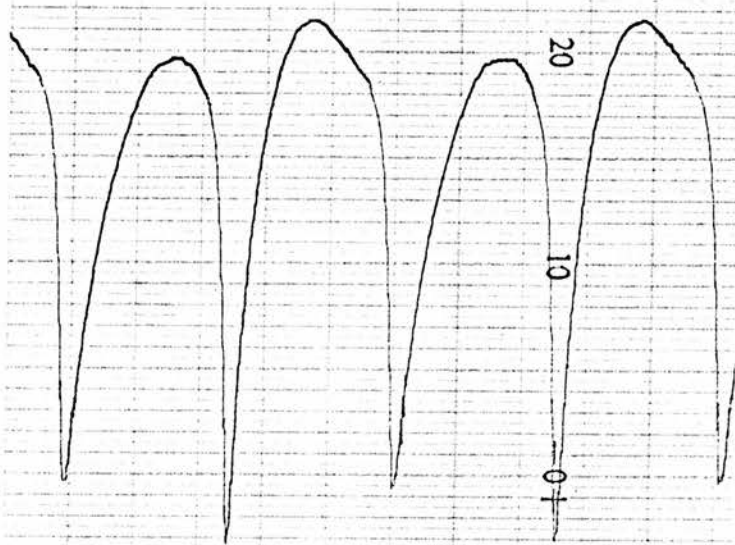
It was hoped that comparison of the signals obtained on the forward and reverse sweeps would enable a separation of the "integral" and "derivative" parts of the spectrum to be carried out, and hence compare experiment with theory quantitatively. Working from the pen-recordings alone, this is an extremely laborious task, and could not be undertaken successfully. Had it been possible to feed the digital output of the Digital Memory Oscilloscope to a computer, the procedure would have been greatly simplified, and some quantitative analysis might have been possible.

7.7 Even Harmonic type Signals.

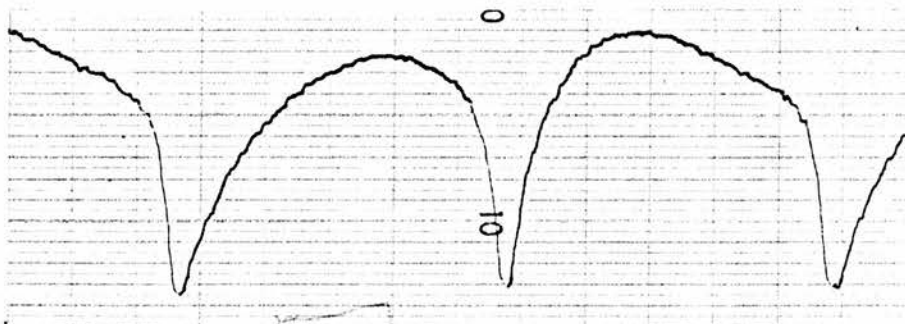
Some examples of the type of even harmonic signal discussed in section 3.4 are shown in Figure 7.6. The experimental conditions are listed in Table 5. Since it is impossible to obtain a distribution of spins which is completely uniform in density and relaxation time, as required by theory, the best that can be done is to find a part of the spectrum which is most nearly uniform, and this explains why the second half cycle is not quite the same shape as the first. Despite this, at least a qualitative similarity to Figure 3.3 is demonstrated. The fact



A



B



C

EXPERIMENTAL EVEN - HARMONIC
SIGNALS

Figure 7.6

TABLE 5.Experimental Conditions for the Recordings shown in Figure 7.6.

Trace	Modulation (gauss)	Klystron Power (dB rel. $10^{-5}W$)	Modulation Frequency	r_0
A	± 0.9	0	160 c/s	10
B	± 0.9	-6	160 c/s	40
C	± 0.9	-12	80 c/s	80

that the dips in the traces are not as sharp as those which might be expected for high values of r_0 is probably due to the non-zero basic line width. This is fairly significant, for in the case of high r_0 and infinitesimal line width, these inverted peaks would be extremely sharp and narrow. Their rounding off indicates the existence of either or both of the following:

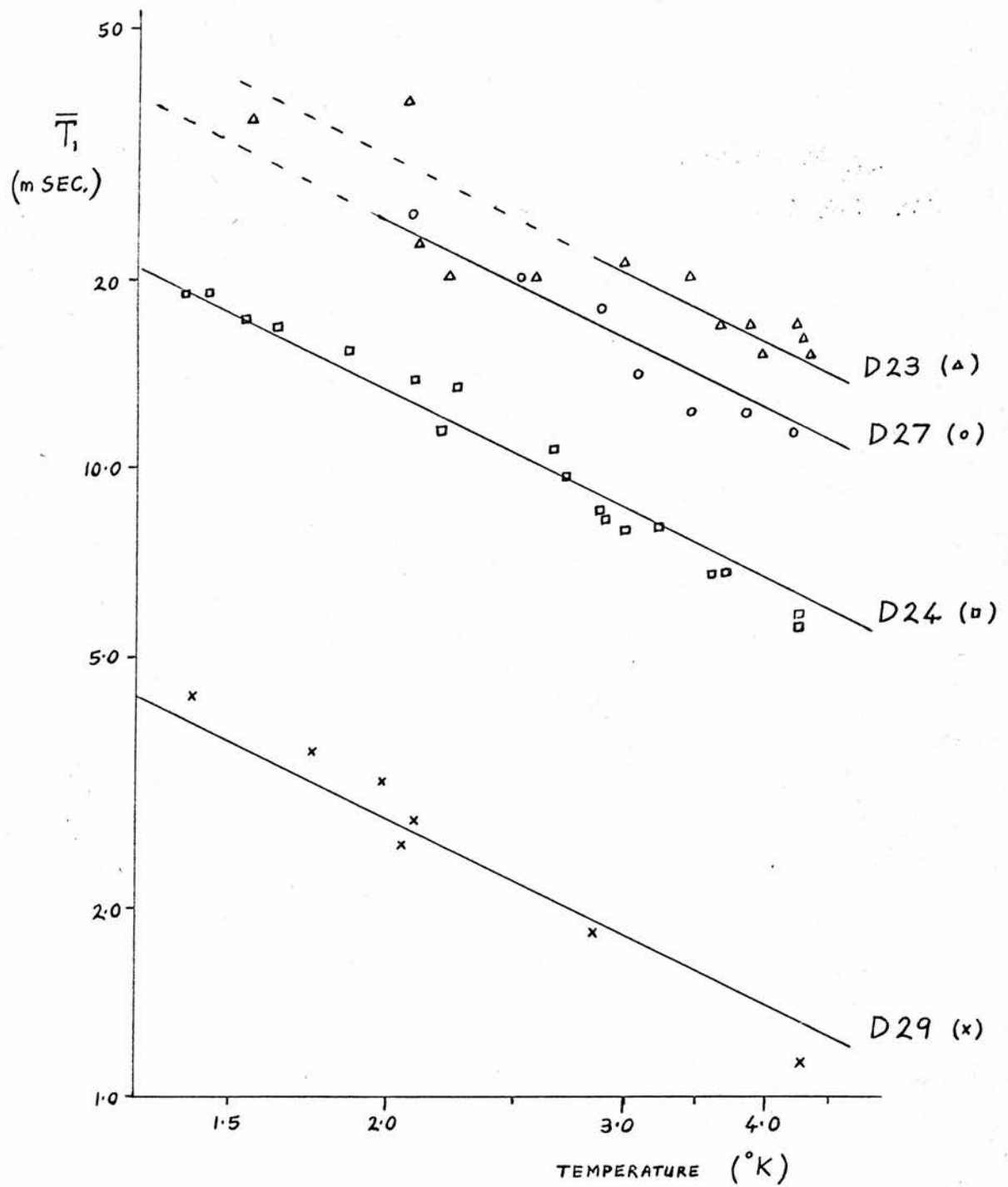
- 1) Finite basic line width.
- 2) Magnet field instability.

The rounding off is in fact very sensitive to either of these factors, because it occurs at the crest of a sine wave (the modulation waveform). For example, a line width or a field instability of only 1% of the modulation amplitude will give rise to a spread of about ± 8 degrees ($\cos^{-1} 0.99$) in the inverted peak. Even with the Newport Post-stabiliser, a field instability of about 0.1 gauss was still present.

7.8 Measurement of the Overall Spin-lattice Relaxation Time, \overline{T}_1 .

In order to obtain a measure of the overall spin-lattice relaxation time, \overline{T}_1 , it is necessary to saturate or at least partially saturate the whole line, and monitor the recovery of the whole line. This can be achieved by the use of method (a) of section 5.3, sweeping through a considerable part of the line. It is not possible to sweep through the whole line, since the wings spread out somewhat indefinitely to over 100 gauss from the centre. It was decided to use 30 gauss peak to peak field modulation, as a compromise between 1) too small field modulation, covering an insufficient amount of the line to give realistic values for an overall relaxation time, and 2) too large field modulation, giving rise to the sampling inaccuracies mentioned in section 5.3 when using the Digital Memory Oscilloscope. Experiments were carried out on the four diamonds D 23, D 24, D 27, and D 29, and the results plotted in Figure 7.7.

It can be seen that there is a considerable spread of points for D 23 at the low temperature end. This is partly due to the limiting low-frequency response of the post-detector amplifying chain (Figure 4.15) which introduces errors when relaxation times longer than about 20 milliseconds are encountered. There is also the fact that the X.13 pulse length is at its upper limit (3.5 milliseconds) so that a modulation frequency of less than 140 c/s cannot be used while still covering half a cycle. This leads to an unduly large number of half cycles being included within the field of the Digital Memory Oscilloscope, and hence



TEMPERATURE DEPENDENCE OF \bar{T}_1 IN DIAMOND

Figure 7.7

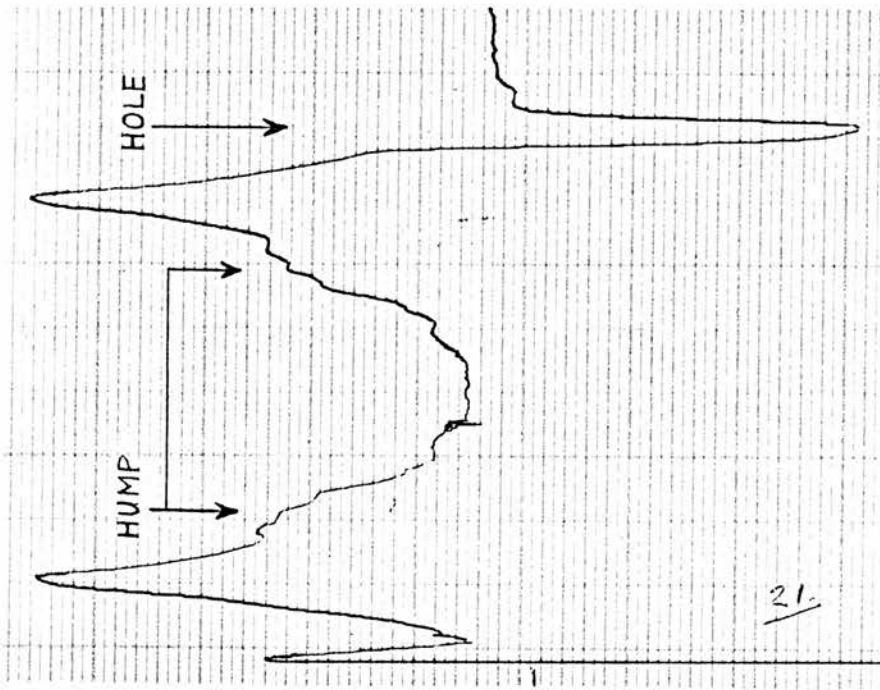
sampling errors. The only way to avoid this is to have better L.F. response in the amplifier and a longer pulse.

The lines drawn on Figure 7.7 represent a temperature dependence $\bar{T}_1^{-1} \propto T$, and are seen to fit reasonably well. This would suggest a direct process of relaxation. The relaxation rate (\bar{T}_1^{-1}) is also seen to be directly proportional to neutron dosage, i.e. density of spins, within a reasonable experimental error. This suggests that the relaxation process involves interactions between pairs of spin centres, and that the relaxation process from individual spin centres to the lattice is considerably slower, and hence not observable at the spin concentrations existing in these samples.

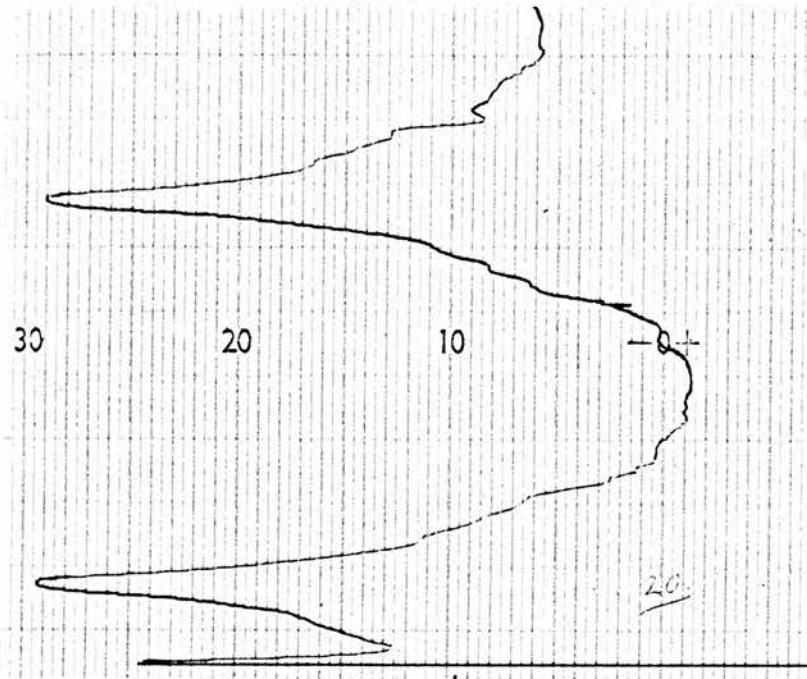
7.9 Confirmation of the S = 1 Nature of the Spectrum.

An observation has been made of a complementary "hole" and "hump" effect in both D 23 and D 27, whereby if a hole is burnt in one side of the line, an inverted hole, or "hump" appears at the mirror image position in the line, on the other side of $g = 2$. This "hump" is not nearly so well defined as the hole, and the best pen-recording of this effect which was obtained is shown in Figure 7.8, which compares the cases (A) with X.13 pulse, and (B) without X.13 pulse (i.e. no hole burnt). The experimental conditions were:

Sample	:	D 23
Temperature	:	1.38° K
Modulating Frequency	:	70 c/s
Modulation Depth	:	± 8 gauss



A WITH PULSE



B WITHOUT PULSE

COMPLEMENTARY HOLE AND HUMP EFFECT

Figure 7.8

Monitor Klystron Power : - 30 dB (10^{-8} watts)
 Pulse Klystron Power : -26 dB (6.3×10^{-4} W) for trace A
 -44 dB (10^{-5} W) for trace B

The "hump" on the other side of the peak can be seen in trace A. It is more easily observed on the oscilloscope where, if the position of the X.13 pulse on the line (i.e. the timing with respect to the modulation) is varied manually, the complementary "hump" can be seen moving on the other side of the line, in the opposite direction.

This observation confirms the $S = 1$ nature of the spectrum. Faulkner et al. (Refs. 59, 62) have suggested that the "d" system in neutron-irradiated diamond (i.e. that part being investigated in this chapter) consists of a large number of triplet systems having a range of zero-field splitting parameter, D . If these triplets all have the same g -value (i.e. $g = 2$) then burning a hole in one side of the line will saturate one of the allowed transitions in each of a selected range of triplets whose other allowed transition lies at an equal distance on the other side of $g = 2$. Since saturation of one transition leads to an increased population difference for the other transition (the same effect as observed in MgO, section 5.6), the signal from the other transition will be increased, resulting in a "hump" in that part of the spectrum corresponding to the other transition.

Ideally, this should lead to a "hump" which is as sharp and well defined as the hole, and the fact that this is not the case suggests that there is a spread of g -values. Triplet systems may also have a non-

zero E-splitting term, due to the disappearance of axial symmetry, and this would have the effect of spreading out the "hump", similar to a spread of g-values. Because of the random nature of neutron irradiation, there is no reason to expect axial symmetry in a vacancy-interstitial pair, the supposed origin of the triplet system. Spin diffusion or cross relaxation sufficient to account for the spread of the "hump" is discounted, since the initial hole retains its shape and position.

In a triplet system, the $\Delta m = 2$ transition is sometimes detectable. It is strictly forbidden only when $D = 0$, but the transition probability decreases rapidly as D tends to zero; in fact it is proportional to D^2 in the limit of D tending to zero (Ref. 64). In the present system D is of the order of $.01 \text{ cm}^{-1}$, making the intensity of any line due to a $\Delta m = 2$ transition very small indeed.

Nevertheless, a group of four lines has been detected in D 29 near half field which could be interpreted in this way. It was also possible to burn holes in these lines, the experimental conditions being:

Modulation Frequency	:	320 c/s
Modulation Depth	:	± 5 gauss
Minimum Pulse Power for Saturation	:	- 14 dB (10^{-2} watts)

This corresponds to $r = 0.1$ (using the half-field value of γ) which represents a certain amount of "forbiddenness" (the value of r required to saturate a line is directly proportional to the transition probability) but nothing like as much as would be expected. It is

therefore very unlikely that this group of lines is directly related to the triplet system.

CHAPTER 8

Points Arising from the Work and Conclusions.8.1 Failure of the Bloch Equations at High Microwave Field.

Consider the interaction of two spins in the rotating coordinate system. Let one (S_1) be at the origin and the other (S_2) be at a distance r , and at an angle θ to the d.c. magnetic field (i.e. the Z-axis). In the rotating frame, S_2 will be averaged out over a circular orbit subtending a conical angle θ to the Z-axis at S_1 , as illustrated in Figure 8.1. The field at S_1 due to S_2 will be the average over the orbit, since the variations due to the rotation will be at a frequency ω_0 , the microwave frequency, which is much too rapid to affect S_1 .

a) The Z-component of S_2 will give rise to a field entirely in the Z-direction:

$$H_Z = (\mu_Z / 4\pi r^3)(3 \cos^2 \theta - 1)$$

b) The X-component of S_2 will give rise to a field entirely in the X-direction. However, at any given instant, it is dependent on ϕ , the angle S_2 makes with the XZ plane at the projection on the Z-axis. Resolving parallel and perpendicular to this ϕ -direction,

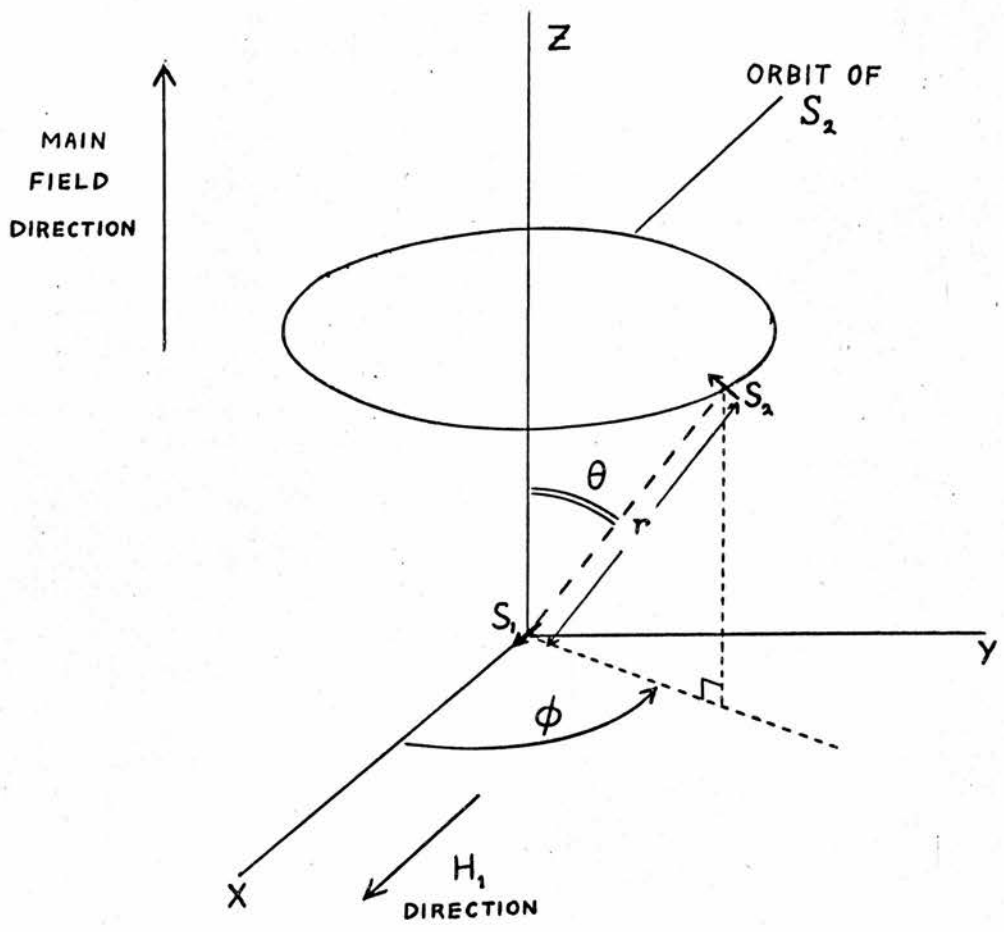
$$H_{\parallel} = (\mu_X \cos \phi / 4\pi r^3)(3 \sin^2 \theta - 1)$$

and

$$H_{\perp} = (\mu_X \sin \phi / 4\pi r^3)$$

whence

$$H_X = H_{\parallel} \cos \phi - H_{\perp} \sin \phi$$



TWO SPINS IN THE ROTATING COORDINATE FRAME

Figure 8.1

$$= (\mu_X / 4\pi r^3)(3 \sin^2 \theta \cos^2 \phi - \cos^2 \phi - \sin^2 \phi)$$

Averaging over ϕ ,

$$\bar{H}_X = - (\mu_X / 8\pi r^3)(3 \cos^2 \theta - 1)$$

and similarly for \bar{H}_Y . Thus the whole interaction between the two spins may be specified by a single constant

$$k = - (\mu / 8\pi r^3)(3 \cos^2 \theta - 1)$$

The field at S_1 is then:

$$\begin{aligned} H_X &= k S_{2X} \\ H_Y &= k S_{2Y} \\ H_Z &= - 2k S_{2Z} \end{aligned} \quad (8.1)$$

If S_2 is precessing in the d.c. magnetic field at some frequency other than that of S_1 , say due to a different g-value or local field difference, then in the rotating coordinate system a component of field at the difference frequency will be present at S_1 . If S_1 is initially lying in the X-direction, along the H_1 field, it can only precess about H_1 at a frequency γH_1 , and unless some component at this frequency is present in the interaction field, no transition will occur. Further, the perturbing field is required to act at right angles to H_1 and be rotating in the appropriate direction.

During passage in the case of free spins, it might be assumed that all start out initially along the Z-direction, and violent precession will only be evident after $t' = 0$ (see the solutions of section 2.6).

This, however, would only be true at 0° K , and in fact spins of all orientations will be encountered, with no more than the expected Boltzmann bias. Thus, in general, precession will be occurring about H , the field in the rotating coordinate system. This field consists of two parts, $H_X = H_1$, and $H_Z = H_0 - \omega/\gamma$. The modulus $\sqrt{H_X^2 + H_Z^2}$ determines the precession frequency, and therefore must match the field seen by S_1 for interaction to take place; i.e. the amplitude of field seen by each spin must be the same in the rotating coordinate frame. Since $H_1 = H_X$ is the same, then either

$$H_{Z1} = H_{Z2}$$

or

$$H_{Z1} = -H_{Z2}$$

In the first case S_1 and S_2 must have identical γ and therefore share the same precession pattern. Any exchange between them will therefore leave the spin system unaffected.

In the second case, S_1 and S_2 only interact for a short time during passage while $H_{Z1} = -H_{Z2}$, or

$$H'' = H'$$

where

$$\underline{H}' = \underline{H}_X + \underline{H}_{Z1}$$

and

$$\underline{H}'' = \underline{H}_X + \underline{H}_{Z2}$$

The precession of S_2 about \underline{H}'' gives rise to fields at various angles at S_1 . Let

$$\tan \theta = H_{Z2} / H_X$$

then

$$S_{2X} = \sin \phi \sin \theta$$

$$S_{2Y} = \cos \phi$$

$$S_{2Z} = \sin \phi \cos \theta$$

giving rise to a perturbation field at S_1 :

$$H_{XP} = k \sin \phi \sin \theta$$

$$H_{YP} = k \cos \phi$$

$$H_{ZP} = - 2k \sin \phi \cos \theta$$

ϕ is the instantaneous angle of rotation of S_2 about $\underline{H''}$, such that $d\phi/dt = \gamma H''$. The component of this perturbation field which is rotating about $\underline{H'}$ in the correct direction is

$$\frac{k \cos^2 \theta}{2}$$

If S_2 is sitting in the midst of a uniform distribution of spins, then for any given H_Z , a portion of the spectrum around S_2 is "reflected" onto S_1 , the strength of the interaction being proportional to $\cos^2 \theta$. But θ is related to rt' (see section 2.5 and Appendix 1b) by

$$\cos^2 \theta = 1 / (r^2 t'^2 + 1)$$

Hence the expectation rate of decay of S_1 is proportional to

$$1 / (r^2 t'^2 + 1) \quad (8.2)$$

This is to be compared with the rate involved in the Bloch equations. In

the adiabatic region treated in Appendix 1(b),

$$S = S_0 \exp(-\beta\theta/r)$$

Hence $(1/S) \cdot dS/dt = -\beta/r$ (8.3)

Therefore $(1/S) \cdot dS/dt' = -\beta \cos^2 \theta = -\beta/(1+r^2 t'^2)$

which is the same law as 8.2.

However, the significant point about the foregoing argument is that it relates the decay rate to a particular part of the spectrum, and the density of spins there.

Now suppose an inhomogeneously broadened line having an overall Gaussian line shape, and consider a spin packet at the centre. For small H_1 , β will be the same during all parts of the passage, and the solution of 8.3 is straightforward. However, if H_1 is comparable with the line width, β will be a function of θ , and from 8.3,

$$\log S = - (1/r) \int \beta \cdot d\theta$$

We can define

$$\beta_{\text{eff}} = (1/\pi) \int_{-\pi/2}^{\pi/2} \beta \cdot d\theta$$

or

$$\begin{aligned} \eta &= \beta_{\text{eff}} / \beta_{\text{max}} = (1/\pi \beta_{\text{max}}) \int \beta \cdot d\theta \\ &= (1/\pi) \int g(\theta) \cdot d\theta \end{aligned}$$

where $g(\theta)$ is the line shape function, such that $g(0) = 1$.

If g is taken as the Gaussian line shape,

$$g(\theta) = \exp(-\alpha \tan^2 \theta)$$

η can be expressed as a function of the normalised line width (i.e. the ratio of the width at the half-signal points to H_1). This has been computed and is shown in Figure 8.2, from which it can be seen that the dependence on width (or on H_1 for a constant width) is considerable. η is down to 0.5 when H_1 is less than one quarter of the line width.

In our original discussion of the Bloch equations, β was inversely proportional to H_1 . In this discussion

$$\beta \propto \eta H_1^{-1}$$

so that for large H_1 , where $\eta \propto H_1^{-1}$,

$$\beta \propto H_1^{-2} \propto \text{Power}^{-1}$$

Hence $r = (dH/dt) / \gamma H_1^2 \propto (dH/dt) \cdot (\text{Power})^{-1} \propto \beta (dH/dt)$

That is, the lines of constant dH/dt are lines of constant r/β , which, of course, in the adiabatic region (Region III) are lines of constant inversion. Hence, at higher powers, the inversion should become relatively independent of power and dependent only on sweep rate. This provides a possible explanation of why the inversion in MgO does not start to fall again at high power for a given sweep rate (Figure 5.3 as compared with Figure 2.6).

Portis (Ref. 65) has also advanced a theory based on spin diffusion

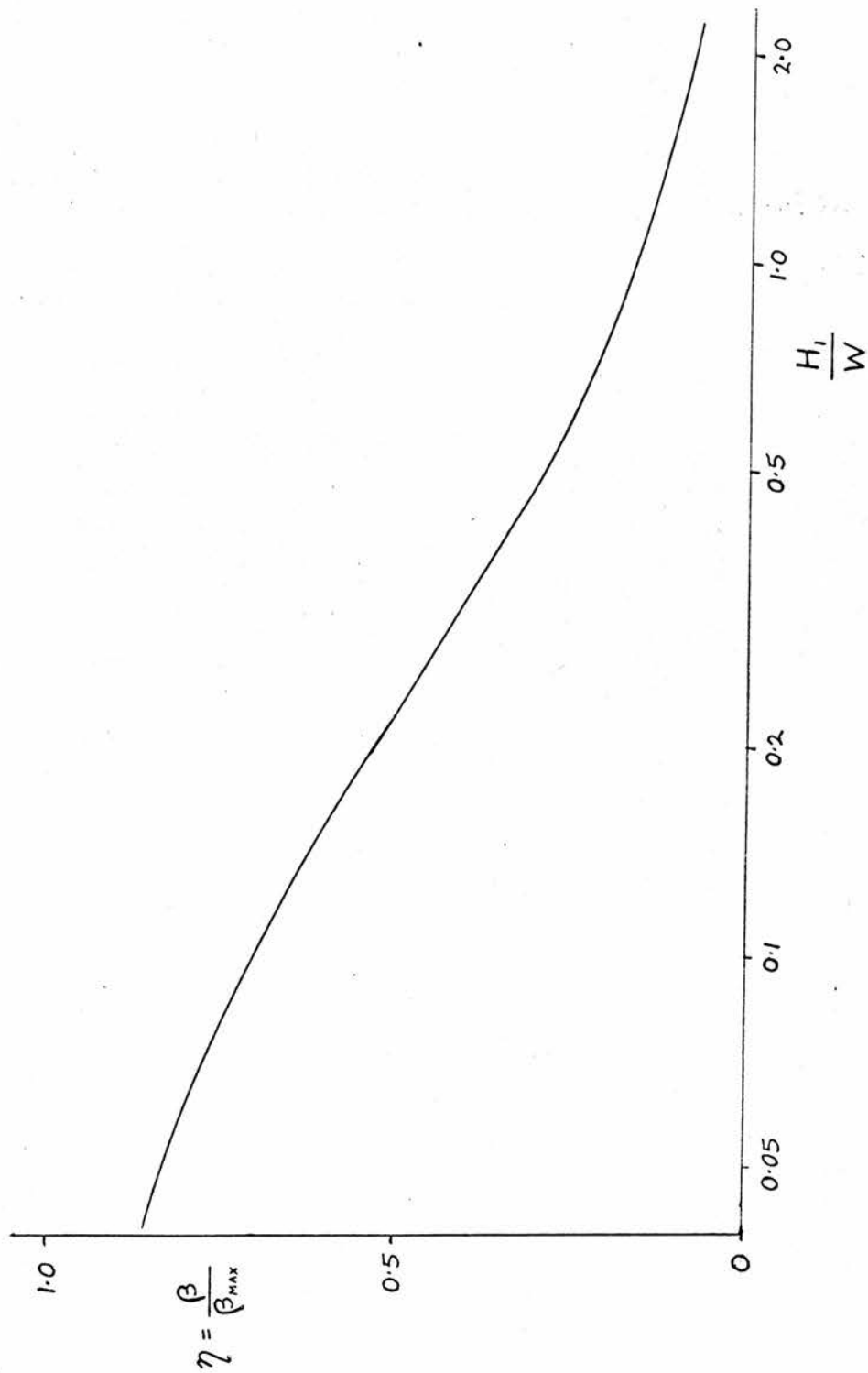


Figure 8.2

REDUCTION OF β FOR A GAUSSIAN LINE SHAPE

which leads to a dependence of T_2 on H_1 . In fact, the whole topic of spin-spin interaction is still under a fair amount of discussion (for example, Refs. 66, 67).

8.2 Anomalous Behaviour of the MgO Satellite Line.

This probably owes much of its anomalous behaviour (section 5.5 and Figure 5.4) to the fact that the system consists of six consecutive levels with five interrelated transitions. It is easily seen that immediately passage is carried out on any one of these transitions, the population differences for the other transitions are changed. Also, if H_1 is comparable with the distances between lines, the passages through the different transitions will not be separated in time, and hence cannot be treated individually. Thus a considerable dependence on the magnitude of H_1 is to be expected, but the problem is extremely complex and no analysis will be attempted here.

8.3 Locus of the $Z_F = 0$ Contour in MgO.

In section 5.7, the locus of the $Z_F = 0$ contour for the main line in magnesium oxide was found to be given by

$$R^* = 6.3 \text{ gauss / microwatt second}$$

in contrast with the expected value of 40 gauss / microwatt second.

This would suggest a lowered transition probability, being 0.16 of the free electron value, or 0.2 if the experimental value of R^* for phosphorus-doped silicon (section 6.5) is taken as being correct. Since the MgO line has a g -value very close to 2, with little or no anisotropy,

this is a very unexpected finding. The most likely explanation is that the line is not "pure"; i.e. it consists of a number of different types of spin system having different relaxation times (both T_1 and T_2). The components having a very short T_1 , for example, would relax before any observation could be carried out, and would also contribute towards reducing the apparent inversion at all points on the map. If, for example, a quarter of the spins were of this nature, the apparent inversion could never exceed 50%, and to give an apparent $Z_f = 0$, r would have to be about 1.3 or less. This would reduce R^* to 20 or less, but cannot account for all the observed discrepancy.

8.4 Conclusions and Recommendations.

As mentioned in the first two chapters, the aim of this thesis has been to study passage effects and to try to correlate theory and experiment. This has been achieved to a moderate extent, both with regard to inversion efficiency measurements and passage effects. The outcome of the study is that the Bloch Equations are of limited use in describing fully the behaviour of a spin system, and although some attempt has been made in this chapter to modify the theory, there remains a considerable gulf between theory and facts, principally in the realm of spin-spin interaction.

The work on neutron-irradiated diamond has shown that by the use of pulse and passage techniques, a certain amount of information can be obtained about a spin system which would otherwise be lost in run-of-the-mill spectroscopy.

Phosphorus-doped silicon has offered the best correlation with the inversion efficiency theory, probably because of the innate simplicity of its spin system.

On the experimental side, several new techniques have been devised and found to yield useful information. In particular, the extended pulse technique (section 5.4), the multiple inversion technique (section 6.3) and hole-burning could benefit from further refinements. Nor has the full range of uses of the Digital Memory Oscilloscope been exploited; it is not without its hazards, as was found in section 5.3, but used with caution it should prove a valuable tool.

APPENDICES

1. Analytical Solution of the Bloch Equations in certain Regions.

Start from the normalised Bloch equations representing passage (equations 2.7):

$$dX/dt' = rt'Y - \beta X \quad (A1.1)$$

$$dY/dt' = Z - rt'X - \beta Y \quad (A1.2)$$

$$dZ/dt' = -Y \quad (A1.3)$$

a) Case when $\beta \gg 1$. This is the region of no "wiggles"; the variation of X, Y and Z with time is smooth. Hence the terms βX and βY are much greater than the derivatives dX/dt' and dY/dt' , and can only be balanced by the remaining terms. The equations then become:

$$\beta X = rt'Y \quad (A1.4)$$

$$\beta Y = Z - rt'X \quad (A1.5)$$

$$dZ/dt' = -Y \quad (A1.6)$$

From A1.4 and A1.5

$$\begin{aligned} Z &= \beta Y - rt'X \\ &= (\beta + r^2 t'^2 / \beta) Y \\ &= (\beta + r^2 t'^2 / \beta) dZ/dt' \end{aligned}$$

Therefore $(dZ/dt') / Z = -1 / (\beta + r^2 t'^2 / \beta)$

Integrating, $\log_e Z = (-1/r) [\tan^{-1}(\beta t'/r)] + \text{constant}$

The limits of t' are $\pm \infty$, and the initial value of Z is +1. Therefore

the constant is $-\pi/2r$

and the final magnetisation is given by

$$\log_e Z_f = -\pi/r$$

or
$$Z_f = \exp(-\pi/r)$$

b) Case when $r \ll 1$. This is another region of no "wiggles", this time the adiabatic region where the magnetisation closely follows the field in direction. All the derivatives are small, at least to a first order. Hence, from A1.3, Y is small to a first order, and therefore dY/dt' is small to a second order. So also is the term βY , since β is small. The other terms in A1.2 are not small, so that the relation

$$Z = rt'X$$

must hold, to a second order. It is convenient to define an angle θ such that

$$\tan \theta = rt'$$

which also gives
$$d\theta/dt' = r \cos \theta \quad (\text{A1.7})$$

and a quantity S such that

$$Z = S \sin \theta$$

and
$$X = S \cos \theta \quad (\text{A1.8})$$

From A1.1 and A1.3,
$$dX/dt' + rt' (dZ/dt') = -\beta X$$

Substituting from A1.7 and A1.8,

$$\begin{aligned} (\frac{dS}{dt'}) \cos \theta - rS \sin \theta \cos^2 \theta + (\frac{dS}{dt'}) \tan \theta \sin \theta \\ + rS \tan \theta \cos^3 \theta = - \beta S \cos \theta \end{aligned}$$

This expression can be simplified by putting

$$\frac{dS}{dt'} = r \cos^2 \theta \left(\frac{dS}{d\theta} \right)$$

whence

$$\frac{dS}{d\theta} = - \beta S / r$$

that is,

$$S = S_0 \exp (- \beta \theta / r) \quad (A1.9)$$

Taking $Z = 1$ at $\theta = - \pi/2$, then at $\theta = + \pi/2$ (the completion of passage)

$$Z_f = - \exp (- \pi \beta / r) \quad \text{Q.E.D.}$$

The value of Z at any intermediate point can also be found from A1.8 and A1.9:

$$Z = - \sin \theta \exp ([\theta + \pi/2] \beta / r) \quad \text{where } \theta = \tan^{-1} r t'$$

The values of Z given by this expression agree closely with the computed ones for $r < 0.25$

2. Relation between H_1 and Power for an H_{012} Cavity.

Let the cavity be represented on a coordinate system by the boundaries $X = 0$, $Y = 0$, $X = 2L$, $Y = B$, and the field configuration be such that there is an electric field node along $X = L$. Let the thickness of the cavity be t ; this dimension is not important, since it does not affect the field configuration. The amplitudes of the electric and magnetic fields at any point X , Y in the cavity are then

$$\begin{aligned}
 E_Z &= E_0 \sin(\pi X/L) \sin(\pi Y/B) \\
 H_X &= H_{X0} \sin(\pi X/L) \cos(\pi Y/B) \\
 H_Y &= H_{Y0} \cos(\pi X/L) \sin(\pi Y/B)
 \end{aligned}$$

By continuity of the magnetic flux ($\nabla \cdot \underline{H} = 0$),

$$BH_{X0} = LH_{Y0}$$

The peak energy contained in the magnetic field is

$$\begin{aligned}
 E &= \int \frac{1}{2} \underline{B} \cdot \underline{H} \, dV \\
 &= (\mu_0 t/2) \int_0^{2L} \int_0^B (H_X^2 + H_Y^2) \, dX \, dY \\
 &= (\mu_0 tLB/4)(H_{X0}^2 + H_{Y0}^2) \\
 &= (\mu_0 H_{Y0}^2 V/8)(1 + L^2/B^2)
 \end{aligned}$$

where V is the cavity volume.

The sample is situated at $X = L$, $Y = B/2$, and hence experiences a magnetic field $H_m = H_{Y0}$ in the Y -direction. The total energy in a resonant circuit (which is equal to the peak magnetic energy) is

$$E = QP / \omega$$

where Q is the unloaded cavity Q factor, P is the mean power dissipated in the cavity and ω is the angular frequency. When the cavity is critically coupled to the waveguide, all the incident power is absorbed, and the loaded Q_L is half the unloaded Q . Hence

$$P = (\mu_0 H_m^2 V \omega / 16 Q_L) (1 + L^2/B^2)$$

The microwave field H_m can be resolved into two counter-rotating components of magnitude $H_1 = H_m/2$, only one of which affects the spin system, as discussed in section 2.3. It is also more convenient to express H_1 in weber metre⁻² than in ampere metre⁻¹. Hence

$$P = (H_1^2 V \omega / 4 \mu_0 Q_L) (1 + L^2/B^2) \quad \text{in M.K.S.U.}$$

For the cavity in question, at liquid helium temperatures, $Q_L = 2000$, $L = 0.8$ ", $B = 0.9$ ", $t = 0.4$ " and $\omega = 2 \pi \times 9300$ Mc/s, giving

$$P \text{ (watts)} = 0.97 H_1 \text{ (gauss)}$$

3. Best Fit Exponential for the Case of Non-uniform Time Interval Progression.

A relation between the signal Y and time T of the form

$$Y = A \exp(-T/T_1) + B$$

is expected, where T_1 is the relaxation time. Let

$$X = \exp(-T/T_1)$$

Then Y against X is a straight line. If, however,

$$X = \exp(-T/T_S)$$

where $T_S \neq T_1$, then the best straight line of Y against X , as computed by

the method of least squares, will not be as good as when $T_S = T_1$; i.e. the fitting error will be larger. It is convenient to compute a dimensionless quantity directly related to the fitting error, namely

$$E = 1 - \sigma^2$$

where σ is the correlation coefficient between X and Y. E is then minimised with respect to T_S , the sharpness of the minimum of E giving a measure of the probable error in T_1 .

The computer program to carry out this process is shown in Figure A3.1. N pairs of values of Y and T are read in, the values of T being normalised to a convenient TN. It is also necessary to read in a rough estimate of the range in which T_1 may be expected to lie. This is done by reading in TS such that T_1 is estimated to fall within the range TS to TS x 10. TS is then incremented in steps of $^{20}\sqrt{10}$, each time calculating E. If, at the Jth step, E(J) is found to be greater than E(J-1), the incrementation stops, and the three values E(J), E(J-1), and E(J-2) used to interpolate the location of the minimum of E, as in statement 7. This simply fits these three points to a parabola and finds the minimum. The subroutine JHLSQ computes the best straight line by the method of least squares. REGY is the gradient, CEPT the intercept on the Y-axis and COR the correlation coefficient (σ). The percentage error D calculated in statement 13 is the change in TS required to double the value of E.

This computation takes considerably longer than the equal-interval method discussed in section 5.3, but nevertheless takes only a second or two per data set. Each data set is labelled according to the number

*
C
C

RELAXATION TIMES 3. J. HUTCHISON.
CALLS JHLSQ

```
DIMENSION Y(50),X(50),T(50),E(21)
R=10.0**0.05
PRINT 21
9 READ 1,LA,LB,N,TS,TN
  READ 2,(Y(I),I=1,N)
  READ 2,(T(I),I=1,N)
  DO 3 J=1,25
    DO 4 I=1,N
      4 X(I)=EXP(-T(I)/TS)
      CALL JHLSQ(N,X,Y,XM,YM,REGY,CEPT,COR)
      E(J)=200.*(1.-COR)
      IF(J-2)3,40,50
40 IF(E(J)-E(J-1))3,3,11
50 IF(E(J)-E(J-1))3,3,7
      3 TS=TS*R
11 PRINT 22,LA,LB
    GO TO 9
      7 D=0.5*(E(J-2)-E(J))/(E(J-2)+E(J)-2.*E(J-1))
      P=D-1.0
      TS=TS*R**P
      DO 6 I=1,N
        6 X(I)=EXP(-T(I)/TS)
        CALL JHLSQ(N,X,Y,XM,YM,REGY,CEPT,COR)
        Y1=CEPT+REGY
        ER=200.*(1.-COR)
        D=2.*ER/(E(J)+E(J-2)-2.*E(J-1))
13 D=SQRTF(D)*11.5
      T1=TS*TN
      PRINT 5,LA,LB,T1,D,CEPT
      GO TO 9
19 CALL EXIT
      5 FORMAT(11H DATA SET I2,2X,I2,3H T=E10.3,3H +-F5.1,
        120H PERCENT. Y(FINAL)= F9.4 )
22 FORMAT(22H NO SOLUTION FOR SET I2,2X,I2)
21 FORMAT(30H RELAXATION TIMES 3. /)
      1 FORMAT(I2,2X,2I2,F5.2,E10.3)
      2 FORMAT(5X,10F5.2)
      END
```

Figure A3.1

```

C      RELAXATION 4.      J. HUTCHISON      JUNE 1966.
C
DIMENSION X(50),Y(50),W(50),T(50),E(21)
R=10.0**0.05
9 READ 1,N,C
  READ 52,(Y(I),I=1,N)
  READ 2,(T(I),I=1,N)
C
C      FIND APPROXIMATE BEST C OVER A RANGE OF 10/1
C=C*.32
DO 13 I=1,N
Y(I)=1.0/(Y(I)*T(I))
13 W(I)=1.0/(Y(I)*Y(I))
DO 3 J=1,21
DO 4 I=1,N
4 X(I)=F(C,T(I))
CALL JHLSQW(N,X,Y,W,XM,YM,REGY,CEPT,COR)
E(J)=200.*(1.-COR)
PRINT 40,C,E(J),REGY,CEPT
3 C=C*R
C
C      INTERPOLATION OF BEST C.
IF(E(2)-E(1))10,10,11
10 DO 8 J=3,21
  IF(E(J)-E(J-1))8,8,7
8 CONTINUE
11 PRINT 22
  GO TO 9
7 D=0.5*(E(J-2)-E(J))/(E(J-2)+E(J)-2.*E(J-1))
  P=J-23
  P=P+D
  C=C*R**P
DO 6 I=1,N
6 X(I)=F(C,T(I))

```

Figure A4.1

```

CALL JHLSQW(N,X,Y,W,XM,YM,REGY,CEPT,COR)
ER=200.*(1.-COR)
D=2.0*ER/(E(J)+E(J-2)-2.0*E(J-1))
D=SQRTF(D)*11.5
PRINT 30,CEPT,REGY,C,D,ER

```

C
C

```

          TABULATION OF Y OVER RANGE T=0.5 TO 5.5
X(1)=0.5
DO 12 J=1,51
X(2)=CEPT*X(1)+REGY*X(1)*F(C,X(1))
X(2)=1.0/X(2)
PRINT 5,X(1),X(2)
12 X(1)=X(1)+0.1
GO TO 9
5 FORMAT(F6.1,7X,E10.3)
30 FORMAT(45H FOR THE RELATION 1/T1= AT+BT*(C,T),
1/4H A=E10.3/4H B=E10.3/4H C=F9.5,8H DEGREES /
2 /16H PROBABLE ERROR= F9.4,9H PERCENT. /4H ER=F9.5//
327H T(DEGREES) T1(SECONDS) )
22 FORMAT(20H NO SOLUTION. ///)
52 FORMAT(8E10.3)
2 FORMAT(10F5.2)
40 FORMAT(4(5X,E10.3))
1 FORMAT(I2,3X,F5.1)
19 CALL EXIT
END

```

C FOR DIRECT + RAMAN PROCESSES,
F(C,T)=T**(A-1.0)

C FOR DIRECT + ORBACH PROCESSES,
F(C,T)=EXPF(-C/T)/T

Figure A4.1

(continued)

function $F(C,T)$ as specified in a separate function statement. The expression derived by the program is also tabulated at intervals of 0.1 degrees in the range 0.5 to 5.5° K.

5. Transition Probability in an $S = 1$ System.

On the assumption of a small zero-field splitting (D) in a triplet system, the two allowed transitions separate spectrally. The problem is whether any one of these transitions can be considered as being equivalent to an $S = \frac{1}{2}$ system.

We shall assume the triplet Hamiltonian used by Stevens (Ref. 68), considering only a D -splitting along the Z -axis.

$$\mathcal{H} = g\beta \begin{pmatrix} D/g\beta + H_Z & (H_X + iH_Y)/\sqrt{2} & 0 \\ (H_X - iH_Y)/\sqrt{2} & 0 & (H_X + iH_Y)/\sqrt{2} \\ 0 & (H_X - iH_Y)/\sqrt{2} & D/g\beta - H_Z \end{pmatrix}$$

If the main magnetic field is along the Z -direction, the eigenfunctions are

$$(1 \ 0 \ 0), \quad (0 \ 1 \ 0) \quad \text{and} \quad (0 \ 0 \ 1)$$

with eigenvalues $g\beta H + D$, 0 and $D - g\beta H$

Suppose now that transitions are restricted to those between the first two states; then the Hamiltonian may be reduced to a 2×2 matrix

$$\mathcal{H} = g\beta \begin{pmatrix} D/g\beta + H_Z & (H_X + iH_Y)/\sqrt{2} \\ (H_X - iH_Y)/\sqrt{2} & 0 \end{pmatrix}$$

When transferred to a rotating coordinate system, with H_Z now the difference between the actual field and the resonance field, it becomes

$$\mathcal{H}' = \frac{1}{2} g \beta \begin{pmatrix} H_Z & \sqrt{2}(H_X + iH_Y) \\ \sqrt{2}(H_X - iH_Y) & -H_Z \end{pmatrix} \quad (\text{A5.1})$$

This is to be compared with the standard matrix Hamiltonian for a spin of $\frac{1}{2}$,

$$\mathcal{H} = \frac{1}{2} g \beta \begin{pmatrix} H_Z & H_X + iH_Y \\ H_X - iH_Y & -H_Z \end{pmatrix}$$

It can be seen that expression A5.1 only differs from this by a factor of $\sqrt{2}$ in the transverse components. This would lead to double the transition probability (i.e. half the microwave power level to produce a given effect) and appears to be the only real difference between the two cases.

Note that there is no reason why the (0 0 1) state should be empty. On average it will be approximately 1/3 occupied, but this will not change during a transition involving the other two states. Another point is that the D-splitting need not be parallel to the Z-axis to arrive at expression A5.1. All that is required is that there be a splitting sufficient to separate the two transitions. Provided that $D \ll g \beta H$, expression A5.1 holds ^dgood.

REFERENCES

- 1 F. Bloch, Phys. Rev. 70, 460 (1946)
- 2 E. Zavoisky, J. Phys. USSR, 9, 211 & 245 (1945)
- 3 E. Zavoisky, J. Phys. USSR, 10, 197 (1946)
- 4 J. Weber, Proc. I.R.E. Transactions on Electron Devices (June 1953)
- 5 J. P. Gordon, H. J. Zeiger & C. H. Townes, Phys. Rev. 95, 282 (1954)
- 6 J. Combrisson, A. Honig & C. H. Townes, Comptes Rendus 242, 2451 (1956)
- 7 N. Bloembergen, Phys. Rev. 104, 324 (1956)
- 8 R. R. Ernst & W. A. Anderson, Rev. Sci. Instr. 36, 1696 (1965)
- 9 E. E. Salpeter, Proc. Phys. Soc. 63A, 337 (1950)
- 10 C. K. Campbell, Ph.D. Thesis, St. Andrews (1960)
- 11 I. M. Firth, Ph.D. Thesis, St. Andrews (1962)
- 12 G. E. Pake, "Paramagnetic Resonance", (Benjamin, 1962)
- 13 C. P. Slichter, "Principles of Magnetic Resonance" (Harper & Row)
- 14 A. Abragam, "Principles of Nuclear Magnetism" (O.U.P.)
- 15 F. Bloch & L. A. Siegert, Phys. Rev. 57, 522 (1940)
- 16 J. Winter, Comptes Rendus Acad. Sci., 241, 375 (1955)
- 17 J. Margerie & J. Brossel, Comptes Rendus 241, 373 (1955)
- 18 E. R. Andrew, "Nuclear Magnetic Resonance" (C.U.P.)
- 19 A. M. Portis, Phys. Rev. 91, 1071 (1953)
- 20 N. Bloembergen, S. Shapiro, P. S. Persham & J. O. Artman, Phys. Rev. 114, 445 (1959)
- 21 J. S. Hyde, Phys Rev. 119.2, 1483 (1960)
- 22 J. S. Hyde, Phys. Rev. 119.2, 1492 (1960)

- 23 A. Gourlay, Dept. of Applied Mathematics, Private communication (1966)
- 24 A. G. Redfield, Phys. Rev. 98, 1787 (1955)
- 25 M. Weger, Bell System Tech. Journal 39, 1013 (1960)
- 26 J. Hervé & J. Pescia, Comptes Rendus 256, 4621 (1963)
- 27 N. Bloembergen, E. M. Purcell & R. V. Pound, Phys. Rev. 73, 679 (1948)
- 28 G. Feher, J. P. Gordon, E. Buehler, E. A. Gere & C. D. Thurmond, Phys. Rev. 109, 221 (1958)
- 29 E. L. Hahn, Phys. Rev. 80, 580 (1950)
- 30 G. Feher, Bell System Tech. Journal 36, 449 (1957)
- 31 I. M. Firth, Jour. Sci. Instr. 39, 131 (1962)
- 32 P. F. Chester, P. E. Wagner, J. G. Castle & G. Conn, Rev. Sci. Instr. 30, 1127 (1959)
- 33 Lecture Notes from Marconi College Radio Engineering Course (1962)
- 34 J. C. M. Henning, Rev. Sci. Instr. 32, 35 (1961)
- 35 P. Jung, Jour. Sci. Instr. 37, 372 (1960)
- 36 J. M. S. Hutchison, Jour. Sci. Instr. 43, 491 (1966)
- 37 N. A. Schuster, Rev. Sci. Instr. 22, 254 (1951)
- 38 D. T. N. Williamson, Wireless World 53, 118, 161 & 282 (1947)
- 39 Y. Crosnier & R. Gabillard, Colloque Ampère, Sept. 1963, 157
- 40 J. N. Aubrun, P. Veillet & Tran Van Hiep, Colloque Ampere, Sept. 1963, 534
- 41 M. P. Klein, G. W. Barton, Low's Paramagnetic Resonance, Vol. II 698, (1963)
- 42 J. P. Gordon, Rev. Sci. Instr. 32, 658 (1961)
- 43 J. E. Wertz, J. W. Orton & P. Auzins, Faraday Soc. Discussions 31, 140 (1961)

- 44 J. E. Wertz, P. Auzins, R. A. Weeks & R. H. Silabee, Phys. Rev. 107, 1535 (1957)
- 45 W. Low, Phys. Rev. 105, 793 (1957)
- 46 P. Auzins, J. W. Orton & J. E. Wertz, Low's Paramagnetic Resonance, Vol. I, 90 (1963)
- 47 H. Van Dijk & M. Durieux, Physica 24, 920 (1958)
- 48 L. M. Roth, Phys. Rev. 118, 1534 (1960)
- 49 H. Honig & E. Stupp, Phys. Rev. Letters 1, 275 (1958)
- 50 H. Hasegawa, Phys. Rev. 118, 1523 (1960)
- 51 D. Pines, J. Bardeen & C. P. Slichter, Phys. Rev. 106, 489 (1957)
- 52 G. Feher & E. A. Gere, Phys. Rev. 114, 1245 (1959)
- 53 G. Feher, Low's Paramagnetic Resonance II, 715 (1963)
- 54 A. Honig & E. Stupp, Phys. Rev. 117, 69 (1960)
- 55 M. B. Prince, Phys. Rev. 93, 1204 (1954)
- 56 P. L. Scott & C. D. Jeffries, Phys. Rev. 127, 32 (1962)
- 57 W. Kohn, Solid State Physics 5, 257 (1957)
- 58 G. Feher, Phys. Rev. 114, 1219 (1959)
- 59 E. A. Faulkner, E. W. J. Mitchell & P. W. Whippey, Nature 198, 981 (1963)
- 60 J. H. E. Griffiths, J. Owen & I. M. Ward, Conference on Defects in Crystalline Solids, Univ. of Bristol, 1954, p 81.
- 61 M. C. M. O'Brien & M. H. L. Price, Conference on Defects in Crystalline Solids, Univ. of Bristol, 1954, p 88.
- 62 E. A. Faulkner & J. N. Lomer, Phil. Mag. 7, 1995 (1962)
- 63 J. A. Baldwin, Phys. Rev. Letters 10, 220 (1963)
- 64 E. Wasserman, L. C. Snyder & W. A. Yager, Jour. Chem. Phys. 41, 1763 (1964)

- 65 A. M. Portis, Phys. Rev. 104, 584 (1956)
- 66 G. Sauermann, Physica 32, 2017 (1966)
- 67 R. H. Terweil & P. Mazur, Physica 32, 1813 (1966)
- 68 K. W. H. Stevens, Proc. Roy. Soc. (London) A214, 237 (1952)